SYNTHESIS OF NOVEL PHOTOACTIVE NANOPARTICLES TOWARDS PHOTOTHERAPY

A THESIS SUBMITTED TO

THE GRADUATE SCHOOL OF ENGINEERING AND SCIENCE

OF BILKENT UNIVERSITY

IN PARTIAL FULFILLMENT OF THE REQUIREMENTS FOR

THE DEGREE OF

MASTER OF SCIENCE

IN

CHEMISTRY

By

Ishmeal Kwaku DUAH

September 2021

SYNTHESIS OF NOVEL PHOTOACTIVE NANOPARTICLES TOWARDS PHOTOTHERAPY

By Ishmeal Kwaku Duah

September 2021

We certify that we have read this thesis and that in our opinion it is fully adequate, in scope and in quality, as a thesis for the degree of Master of Science.

Dönuş Tuncel (Advisor)

Halil Okur

Ferdi Karadaş

Ulrike Salzner

Irem Erel Göktepe

Approved for the Graduate School of Engineering and Science:

Ezhan Karaşan

Director of the Graduate School

ABSTRACT

SYNTHESIS OF NOVEL PHOTOACTIVE NANOPARTICLES TOWARDS PHOTOTHERAPY

Ishmeal Kwaku DUAH

M.S. in Chemistry

Advisor: Dönüş TUNCEL

September 2021

Nanomaterial-based compounds are attracting a lot of interest because many functionalities such as photoactive units, drugs and targeting groups can be combined on one platform to fight against infectious diseases and cancer. Recently, conjugated polymer-based nanomaterials have proven to be effective photosensitizers for antibacterial and photodynamic cancer therapies owing to their unique electronic and optical properties, including high singlet oxygen generation capacity, strong light-harvesting ability and its tunable optical spectrum. In this study, novel cross-linked conjugated polymer nanoparticles-based photosensitizers namely conjugated polymer-porphyrin nanoparticles (CPPN) and cross-linked conjugated polymer nanoparticles (PCP) were synthesized. The nanoparticles were prepared via nanoprecipitation using cucurbit[6]uril-(CB6)-catalyzed azide-alkyne cycloaddition (CB6-AAC) reaction. Conjugated polymer-porphyrin nanoparticles (CPPN) are advantageous than micelles incorporating porphyrin systems. For micelles containing porphyrin systems, the phototherapy effect of the porphyrin can only be seen after the porphyrin is released by conditions such as a change in pH, which is not the case for conjugated polymer-porphyrin nanoparticles (CPPN). The nanoparticles demonstrated high reactive oxygen species (ROS) generation efficiency which is evident in the antibacterial and anticancer photodynamic therapy (PDT) experiments. From the antibacterial photodynamic therapy experiment, when Gram-negative (*Escherichia*

coli, *E. coli*) and Gram-positive (*Bacillus subtilis*, *B. Subtilis* and *Staphylococcus aureus*, *S. aureus*) bacteria were incubated with CPPN (20 µg/mL) and irradiated with white light (22 mW/cm^2) for 10 min, more than 3.5-log reduction in colony-forming units (CFUs) was recorded for CPPN**.** Furthermore, when *E. coli* and *B. subtilis* were treated with PCP (24 µg/mL) and illuminated with light, about 3-log killing efficiency was recorded. However, in the dark, the nanoparticles demonstrated minimal dark cytotoxicity against the model bacteria. In addition, the anticancer photodynamic effect of CPPN and PCP on MCF-7 breast cancer cells was investigated. When MCF-7 breast cancer cells were treated with PCP in the dark and under light irradiation, almost all cells were alive for both cases. It may be that PCP could not generate enough reactive oxygen species to kill the cells. When MCF-7 breast cancer cells were treated with CPPN in the dark, the cell viability was 96% and upon irradiation with light for 20 minutes, the cell viability decreased to about 4%. Moreover, conjugated polymer-porphyrin-gold nanoparticles (CPPN-Au) and cross-linked conjugated polymer-gold nanoparticles (PCP-Au) nanoparticles were prepared, but due to the instability of the nanoparticles, they could not be used in phototherapy.

Keywords: Cucurbituril, conjugated polymer, porphyrin, click reaction, photodynamic therapy, singlet oxygen, nanoparticle.

ÖZET

FOTOTERAPIYE YÖNELIK ÖZEL FOTOAKTIF NANOPARTIKLER SENTEZI.

Ishmeal Kwaku DUAH

Kimya, Yüksek Lisans

Tez Danışmanı: Dönüş TUNCEL

Eylül 2021

Fotoaktif birimler, ilaçlar ve hedefleme grupları gibi birçok işlevsellik, bulaşıcı hastalıklar ve kansere karşı savaşmak için tek bir platformda birleştirilebildiğinden, nanomateryal bazlı bileşikler çok ilgi görüyor. Son zamanlarda, konjuge polimer bazlı nanomalzemelerin, yüksek singlet oksijen üretme kapasitesi, güçlü ışık toplama kabiliyeti ve ayarlanabilir optik spektrumu dahil olmak üzere benzersiz elektronik ve optik özellikleri sayesinde antibakteriyel ve fotodinamik kanser tedavileri için etkili ışığa duyarlılaştırıcılar oldukları kanıtlanmıştır. Bu çalışmada, iki yeni çapraz bağlı konjuge polimer bazlı nanopartikül, yani konjuge polimer-porfirin nanopartiküller (CPPN) ve çapraz bağlı konjuge polimer nanopartiküller (PCP), cucurbit[6]uril-(CB6)-katalizli azid-alkin siklo ilavesi (CB6-AAC) reaksiyon kullanılarak nanoçökeltme yoluyla rapor edilmiştir. Konjuge polimer-porfirin nanoparçacıkları (CPPN), porfirin sistemleri içeren misellerden daha avantajlıdır. Porfirin sistemleri içeren miseller için, porfirinin fototerapi etkisi, ancak konjuge polimer-porfirin nanoparçacıkları (CPPN) için geçerli olmayan pH değişikliği gibi koşullar tarafından porfirinin salınmasından sonra görülebilir. Nanopartiküller, antibakteriyel ve antikanser fotodinamik terapi (PDT) deneylerinde açıkça görülen yüksek reaktif oksijen türleri (ROS) üretme verimliliği göstermiştir. Antibakteriyel fotodinamik terapi deneyinden, Gram negatif (Escherichia coli, E. coli) ve Gram pozitif (Bacillus subtilis, B. Subtilis ve Staphylococcus aureus, S. aureus)

bakteriler CPPN (20 µg/mL) ile inkübe edildiğinde ve 10 dakika boyunca beyaz ışıkla (22 mW/cm2) ışınlanmış, CPPN için koloni oluşturan birimlerde (CFU'lar) 3.5 log'dan fazla azalma elde edilmiştir. Ayrıca, E. coli ve B. subtilis, PCP (24 µg/mL) ile muamele edildiğinde ve ışıkla aydınlatıldığında, yaklaşık 3-log öldürme verimliliği kaydedildi. Bununla birlikte, karanlıkta, nanopartiküller, model bakterilere karşı minimum karanlık sitotoksisite gösterdi. Ayrıca CPPN ve PCP'nin MCF-7 meme kanseri hücreleri üzerindeki antikanser fotodinamik etkisi araştırıldı. MCF-7 meme kanseri hücreleri, karanlıkta ve ışık ışınlaması altında PCP ile tedavi edildiğinde, her iki durumda da hemen hemen tüm hücreler canlıydı. PCP, hücreleri öldürmek için yeterli reaktif oksijen türü üretememiş olabilir. MCF-7 meme kanseri hücreleri, karanlıkta CPPN ile tedavi edildiğinde, hücre canlılığı %96 idi ve 20 dakika boyunca ışıkla ışınlamanın ardından hücre canlılığı yaklaşık %4'e düştü. Ayrıca konjuge polimer-porfirin-altın nanoparçacıkları (CPPN-Au) ve çapraz bağlı konjuge polimer-altın nanoparçacıkları (PCP-Au) nanoparçacıkları hazırlanmış ancak nanoparçacıkların kararsızlığı nedeniyle fototerapide kullanılamamıştır.

Anahtar sözcükler: kükürbitüril, porfirin, fotodinamik terapi, konjuge polimer, çıt-çıt tepkimesi, singlet oksijen, nanoparçacık.

Acknowledgement

Firstly, I would like to express my deepest appreciation to my supervisor Assoc. Prof. Dr. Dönüş Tuncel for her support, supervision and guidance throughout my master studies. I am privileged to be part of the DT research group.

Secondly, I am thankful to the examining committee members, Asst. Prof Halil Okur, Assoc. Prof. Irem Erel Göktepe, Asst. Prof. Ferdi Karadaş, and Prof. Dr. Ulrike Salzner for their time to review my thesis.

Also, I am thankful to Dr. Aisan Khaligh and Duygu Deniz Akolpoğlu for their help throughout my thesis work.

Lastly, special thanks to my parents Mr. Yusif Kofi Asamoah and Nafisa Baah for their immense support, love, encouragement and prayers thought my life.

Contents

List of Figures

List of Tables

List of Abbreviations

B. subtilis	Bacillus subtilis
BBr_3	Boron tribromide
CB	Cucurbituril
CD	Cyclodextrin
CFU	Colony forming units
CPNs	Conjugated polymer nanoparticles
CPD	Critical point drying
DCM	Dichloromethane
DCFH	2,7-dichlorofluorescein
DDQ	2,3- dicholoro-5,6-dicyano-l,4-benzoquinone
DLS	Dynamic light scattering
DMEM	Dulbecco's modified eagle medium
DMSO	Dimethyl sulfoxide
E. coli	Escherichia coli
ESI-MS	Electrospray ionization mass spectrometry
EtOH	Ethanol
FT-IR	Fourier transfer infrared spectroscopy
HOMO	Highest occupied molecular orbital
LB	Luria-Bertani medium
LUMO	Lowest unoccupied molecular orbital

MIC Minimum inhibitory concentration

MTT Methyl thiazolyl tetrazolium

NIR Near infrared

NMR Nuclear magnetic resonance

NPs Nanoparticles

OD_{600} Optical density at 600 nm

PBS Phosphate-buffered saline

PDT Photodynamic therapy

PL Photoluminescence

PS Photosensitizer

ROS Reactive oxygen species

RT Room temperature

SEM Scanning electron microscopy

TEM Transmission electron microscopy

XPS X-ray photoelectron spectroscopy

TCBQ Tetrachloro-p-benzoquinone

THF Tetrahydrofuran

TPP Tetraphenylporphyrin

UV-vis Ultraviolet-visible

$^1O_2$ Singlet oxygen

$^3O_2$ Triplet oxygen

λ Wavelength

CPPN Conjugated polymer-porphyrin nanoparticles

PCP Cross-linked conjugated polymer nanoparticles

CPPN-Au Conjugated polymer porphyrin-gold nanoparticles

PCP-Au Cross-linked conjugated polymer-gold nanoparticles

List of Compound Names and Codes

CPPN	Conjugated polymer-porphyrin nanoparticles
M l	2- (2,5-dibromothiophen-3-yl) ethan- l-ol
M2	2,5-dibromo-3-(2-bromoethyl)thiophene
M3	3- (2-azidoethyl)-2,5-dibromothiophene
TPP-Br	5,10,15,20-tetrakis(α-bromo-p-tolyl)porphyrin
CP-AZ	Azide-functionalized conjugated polymer
KD2	N1, N3-di(prop-2-yn-1-yl)propane-1,3-diamine dihydrochloride
TPP-4AL	Prop-2-ynyl-4-[10,15,20-tris-(4-prop-2-ynylaminomethylphenyl)- porphyrin-5-yl]-benzyl-amine
PCP	Cross-linked conjugated polymer nanoparticles

Chapter 1

1 Introduction

During the last decades, antibiotics have played a vital role in the fight against pathogens and in the prolongation of human life. However, the overuse of antibiotics leads to the emergence of microbial strains that show resistance to antibiotics, making antimicrobial therapy difficult. Avoiding the risk of antibiotic resistance is important, and alternative antimicrobial therapies have been urgently sought to alleviate the crisis. [1-4] Each year, an estimated 700,000 people die from antibiotic-resistant microbials. Also, World Health Organization (WHO) predicts that by 2050 it will reach 10 million deaths a year if drastic measures are not taken. Phototherapy (photodynamic and photothermal therapy) is an alternative method that can be used to combat antibiotic-resistant microbials.

According to The International Agency for Research on Cancer, by 2040, the number of new cancer cases and cancer-related deaths is expected to reach 29.5 million and 16.4 million, respectively, each year. In 2020, 1.81 million new cancer cases were reported in the United States, and 606,520 people died from the disease, according to National Cancer Institute (NCI). Cancer is mostly treated with chemotherapy and radiotherapy, but these treatment methods can cause severe effects such as hair loss, anaemia, and sex and fertility issues in patients. Phototherapy (photodynamic and photothermal therapy) serves as an alternative method because it is less costly and has negligible side effects. Phototherapy can be used to treat cancer such as skin, eye, actinic keratosis, and non-small cell lung cancer. [5-7]

1.1 Phototherapy

Phototherapy is mainly classified into two groups, namely photodynamic therapy and photothermal therapy. Photodynamic therapy involves the use of reactive oxygen species

(ROS) for treatment, while for photothermal therapy, thermal energy (heat) is used. In this section, we will discuss photodynamic and photothermal therapy in detail.

1.1.1 Photodynamic therapy

Photodynamic therapy (PDT) is a non-invasive therapeutic method that is efficient against cancer, bacteria, viruses and other microbes. [8,9] For PDT, three key elements are essential; photosensitizer (PS), light and molecular oxygen. [10,11] When the PS is illuminated with light at a specific wavelength, PS moves from the ground state (S_0) to the excited state (S_1) and then undergoes intersystem crossing to the excited triplet state (T_1), as depicted in Figure 1.12. From there, the photosensitizer can undergo two types of reactions at the excited triplet state. Type I reaction; the photosensitizer directly interacts with substrates to generate reactive oxygen species (ROS), mainly active radicals, while for Type II reaction, the photosensitizer in the triplet state transfers its energy to the surrounding molecular oxygen ($^3O_2$) and convert it to highly reactive singlet oxygen ($^1O_2$). Type I and Type II reactions occur instantaneously, and their likelihood of occurrence depends on the type of photosensitizer used, the availability of substrate and oxygen, and the binding affinity of the sensitizer for the substrate.

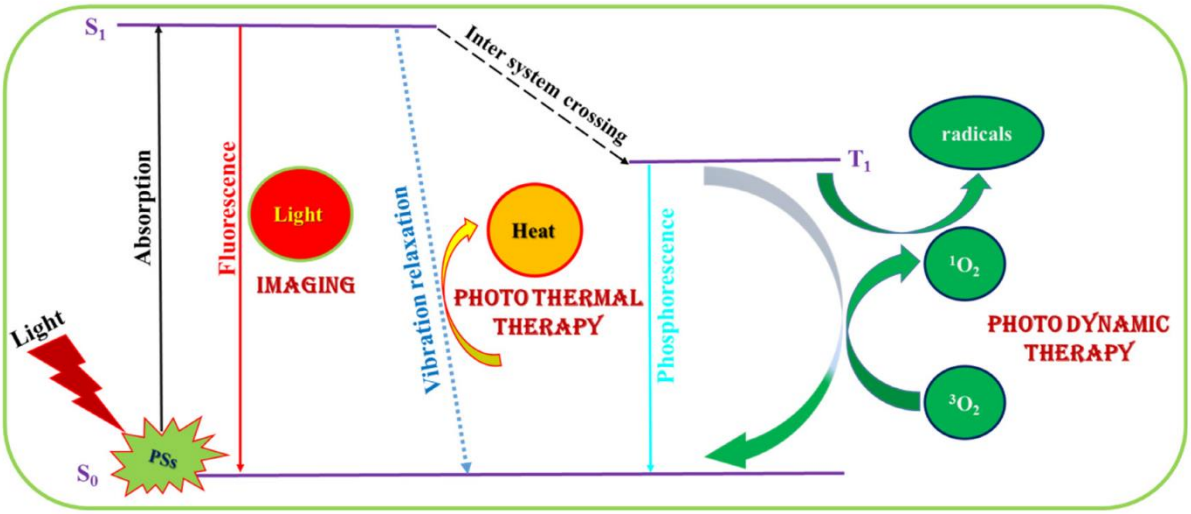

Figure 1.1: Modified Jablonski energy diagram for the generation of ROS. [12]

Ideal photosensitizers have a well-defined chemical structure, good aqueous solubility and stability, minimal dark cytotoxicity, and high singlet oxygen (1O2) generation ability when irradiated with light.

Furthermore, photosensitizers absorbing at higher wavelengths (600-800 nm) can increase the therapeutic efficacy because more light can penetrate into tissues. ROS (peroxides, superoxide, hydroxyl radical and singlet oxygen) generated by photosensitizers can interact with biological components such as plasma membrane, peptides, proteins, and nucleic acids through oxidative reactions, and as a result, the activity is disrupted, leading to cell death. Also, ROS kill bacteria by destroying the cell membrane. [10,11]

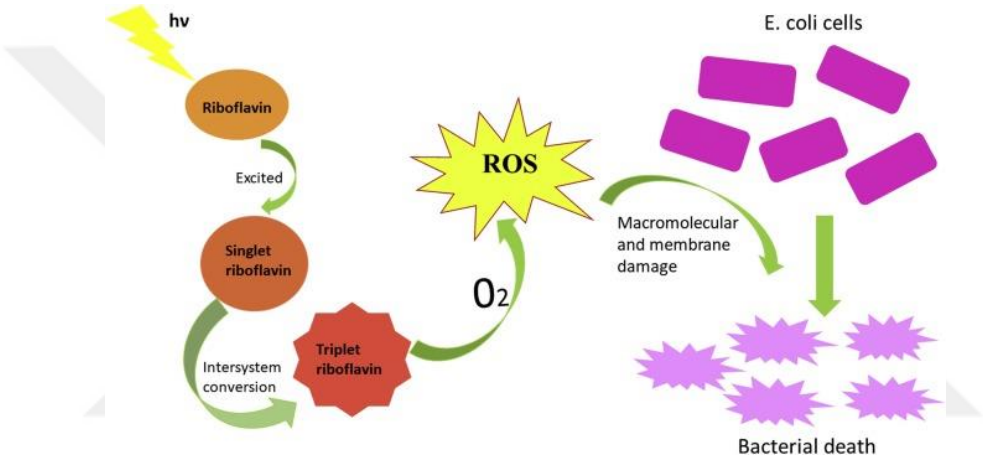

Figure 1.2: In activation of a bacteria using photodynamic therapy. Reprinted with permission from [84].

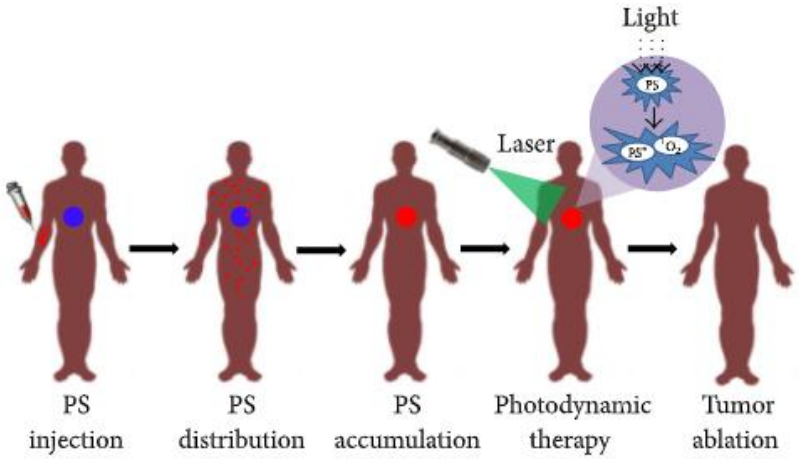

Figure 1.3: Clinical application of photodynamic therapy. Reprinted with permission from [13].

1.1.2 Photothermal therapy

The photothermal effect is caused by the photo-excitation of a photosensitizer which causes the production of thermal energy (heat). Photothermal therapy (PTT) is a promising cancer therapy technique based on the photothermal effect caused by irradiating photosensitizer by a NIR laser, thereby converting light energy into thermal energy. The main benefit of PTT is its capability of wavelength-dependent selectivity. In PTT, the heat released causes a rapid surge in temperature, which generates local hyperthermia (41-48 ^{0}C) or irreversible injury (48-60 ^{0}C), leading to bacteria and tumour cell death. The rise in temperature only kills cancer cells without causing damage to normal cells because normal cells are more tolerant to higher heat than cancer cells. [85-86] Gold nanostructures such as gold nanoparticles, nanorods, nanocages and nanostars have been superior photothermal agents due to their localized surface plasmon resonance (LSPR) effect in the near-infrared region (NIR), allowing NIR light energy to be converted to thermal energy at high yield.

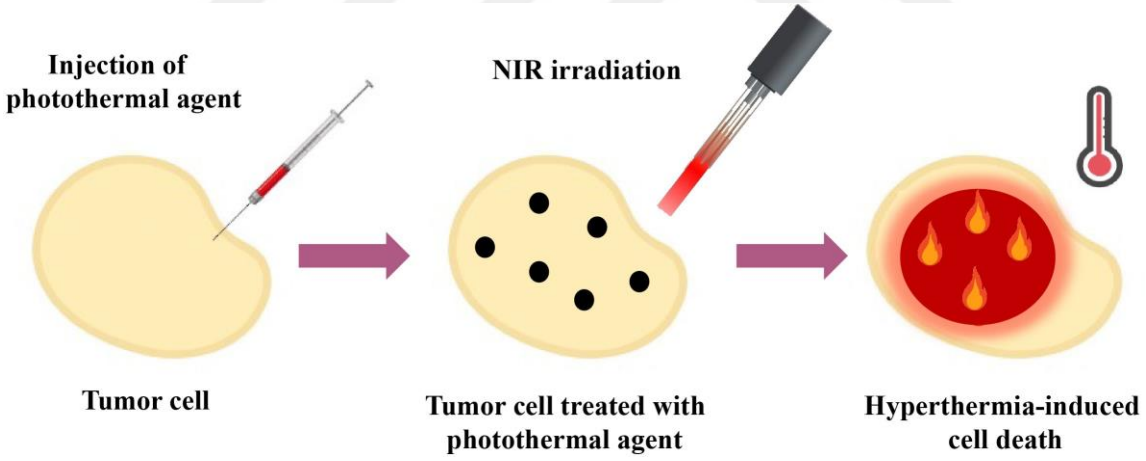

Figure 1.4: Photothermal cancer therapy.

1.1.3 Photosensitizers used in Phototherapy

Nanomaterial-based systems are also gaining increasing attention because they can hold many functionalities, including the photoactive units, drugs and targeting groups in one platform to

fight infectious diseases and cancer more effectively. [24-26] Nanoparticles of conjugated, photoactive compounds such as porphyrins, conjugated polymers and oligomers, bodipys and phthalocyanines have been used in phototherapy due to their ability to generate reactive oxygen species (ROS) when irradiated with light at the appropriated wavelength. In this section, we will focus on conjugated polymer and porphyrin-based nanoparticles.

1.1.3.1 Porphyrin Nanoparticles

Porphyrin and its derivatives have attracted a lot of attention as a photosensitizer in photodynamic therapy (PDT) due to their excellent photophysical properties such as efficient absorption in the near-infrared region, high molar extinction coefficient and high singlet oxygen (1O2) quantum yield when irradiated with light. [14-16] To date, derivates of porphyrin such as Photofrin® and Fotolon® are used clinically for PDT. [17,18] In 1993, Photofrin® became the first approved PS for the treatment of bladder cancer in Canada. [19] However, they still face many problems, such as poor biocompatibility, and they are less selective towards cancer cells. To increase the therapeutic effects of PDT, the synthesis of novel porphyrin-based photosensitizers with high $^1O_2$ quantum yield and biocompatibility is needed.

Zhang *et al.* reported a photosensitizer assembled from CB7 and methylpyridinium-attached porphyrin (TPOR). Singlet oxygen ($^1O_2$) quantum yield of TPOR-CB7 assembly is higher than that of TPOR due to the strong host-guest complexation between CB7 and methylpyridinium in the aqueous medium. Due to increased singlet oxygen quantum yield, the antibacterial efficacy of TPOR-CB7 is enhanced (Figure1.5). [20-21]

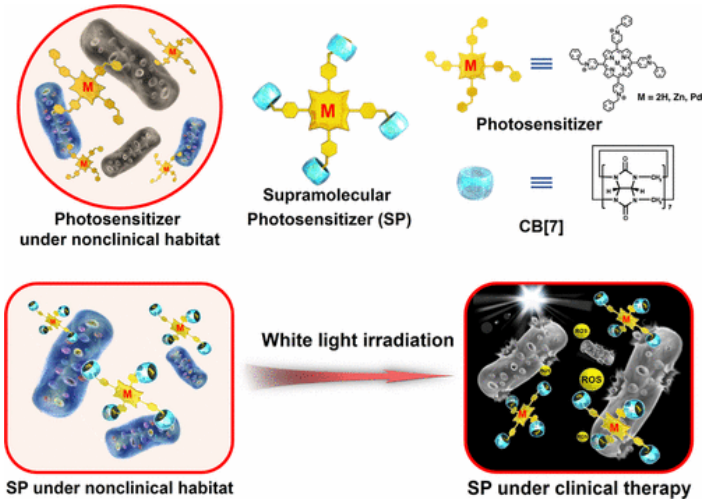

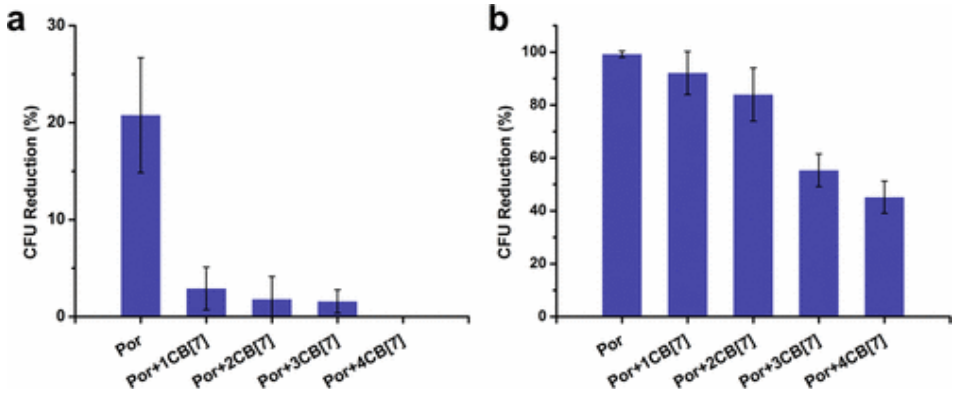

Figure 1.5: Colony-forming unit (CFU) reduction of Por (2.5×10^{-6} M) and Por with different ratios of CB[7] (a) in the dark and (b) under white-light illumination. (Reprinted with permission from [20]. Copyright 2017, American Chemical Society)

Özkan *et al*. reported a porphyrin-based 5-rotaxane. This assembly was synthesized through CB6 catalyzed click reaction between an alkyne functionalized porphyrin and an azide functionalized stopper group. From the antibacterial experiment, when Gram-negative bacteria (*Escherichia coli, E. coli*) were treated with this photosensitizer (3.5 μm) and irradiated with white light (22 mW/cm^2) for a minute, 96 % of E. *coli* were killed, but in the dark, only 9% were killed. The presence of cucurbit[6]uril (CB6) reduced the dark toxicity of the photosensitizer by ion-dipole interaction between the cationic groups of the porphyrin and carbonyl groups of CB6. [23]

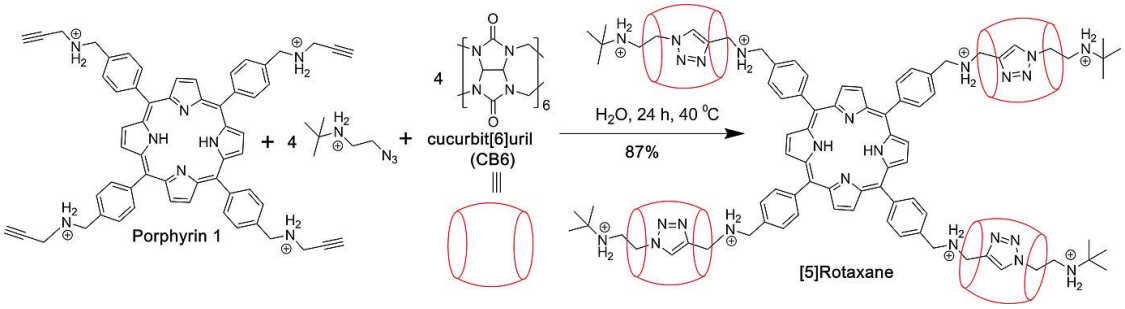

Figure 1.6: Synthetic scheme for [5]rotaxane.

Gao *et al*. reported a hyaluronan conjugated zinc protoporphyrin using an ester bond (HA-es-ZnPP) and studied its anticancer PDT effect on the C26 colon cancer cell line. [22] HA-es-ZnPP demonstrated high solubility in water and formed micelles with a size of ~ 40 nm in an

aqueous solution. Cytotoxicity increased by 10-fold when mouse C26 colon cancer cells were treated with HA-es-ZnPP and illuminated with light (Figure 1.8)

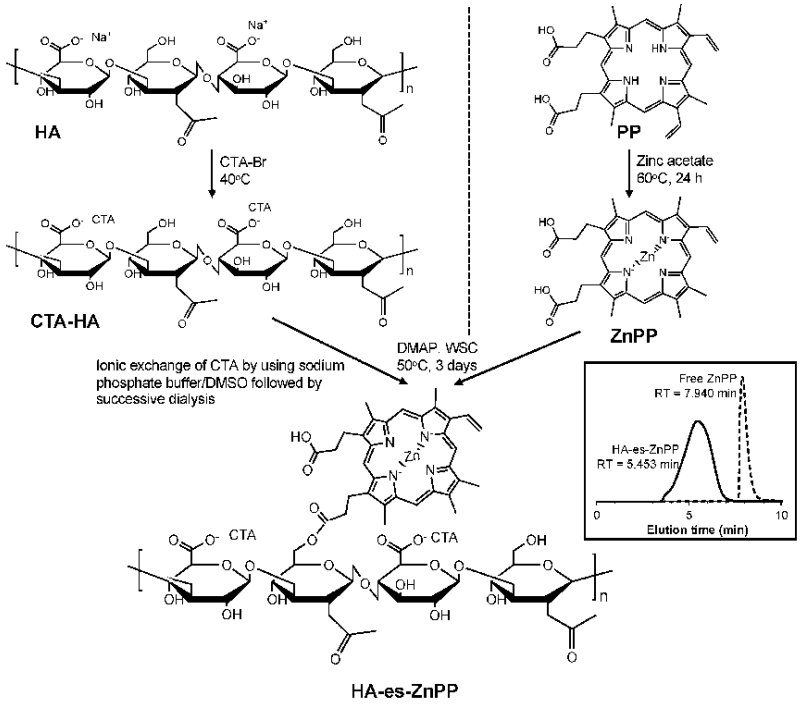

Figure 1.7: Synthesizing protocol of hyaluronan (HA) conjugated ZnPP through ester bond (HA-es-ZnPP). Reprinted with permission from [22].

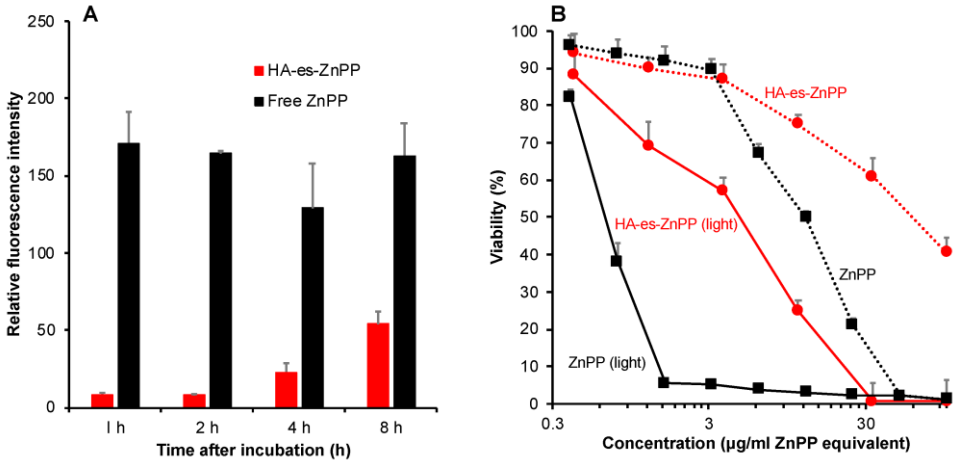

Figure 1.8: Intracellular uptake (**A**) and in vitro cytotoxicity (**B**) of HA-es-ZnPP in C26 colon cancer cells. (**A**), free ZnPP or HA-es-ZnPP (20 μg/mL ZnPP equivalent) was added to C26 cells for the indicated time. Reprinted with permission from [22].

Zeng *et al*. prepared chitosan-coated Au NPs connected to meso-tetrakis(4-sulphonato phenyl) porphyrin (TPPS) via electrostatic interaction to form a hybrid nanoparticle (TPPS/QCS-SH/Au NPs) (Figure 1.9). [88] The nanoparticles were utilized in both photothermal and photodynamic therapy against HepG2 cancer cells. When nanoparticles were illuminated with a laser, the temperature increased to about 56 °C, and a large number of reactive oxygen species were generated from the porphyrin. From their results, when HepG2 cancer cells were treated with TPPS/QCS-SH/Au NPs and irradiated with laser (10 min), the cell viability reduced to about 14.3% (Figure 1.10).

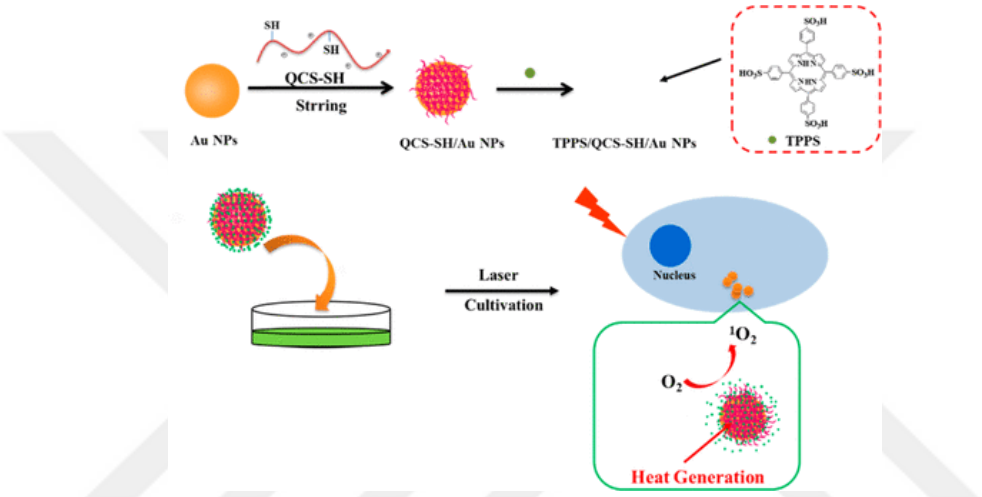

Figure 1.9: Illustration for the Preparation of TPPS/QCS-SH/Au NPs and Its Anticancer Property by PDT/PTT. (Reprinted with permission from [88]. Copyright 2018, American Chemical Society)

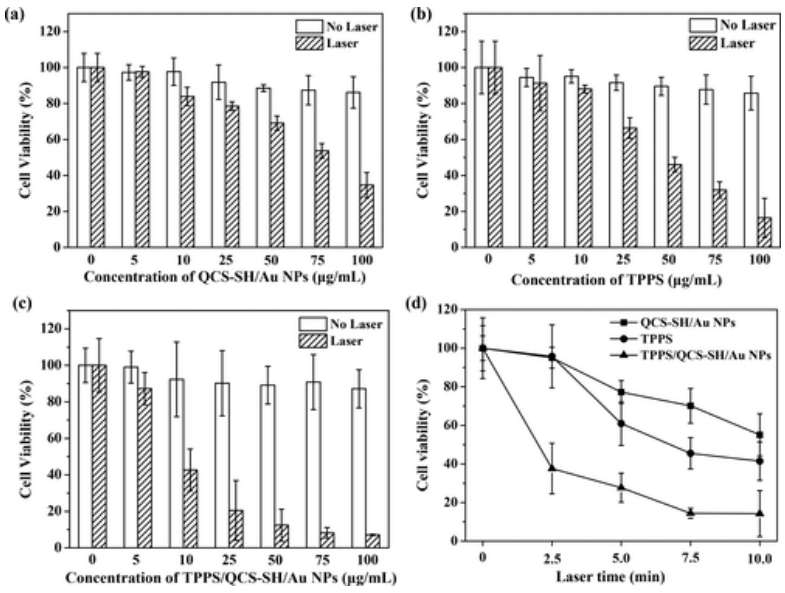

Figure 1.10: Cell viability of HepG2 treated with (a) QCS-SH/Au NPs, (b) TPPS, and (c) TPPS/QCS-SH/Au NPs at different concentrations before and after laser irradiation for 10 min at 635 nm (0.85 W/cm^2). (d) Cell viability incubated with different nanoparticles at the same concentrations (50 μg/mL) of various nanoparticles by laser irradiation at 635 nm (0.85 W/cm2) multiple times. (Reprinted with permission from [88]. Copyright 2018, American Chemical Society)

Karunakaran *et al*. reported a novel water-soluble porphyrin (THPP) and its Zn metalated derivative (Zn-THPP). [89] They investigated the light-induced photodynamic effect of the photosensitizers on MDA MB 231, IMR 32 and MCF 7 cancer cells. From their results, the photodynamic therapy activity of THPP was about 2-3-fold higher than that of Photofrin in all the model cancer cells used. Also, THPP was used in cellular imaging.

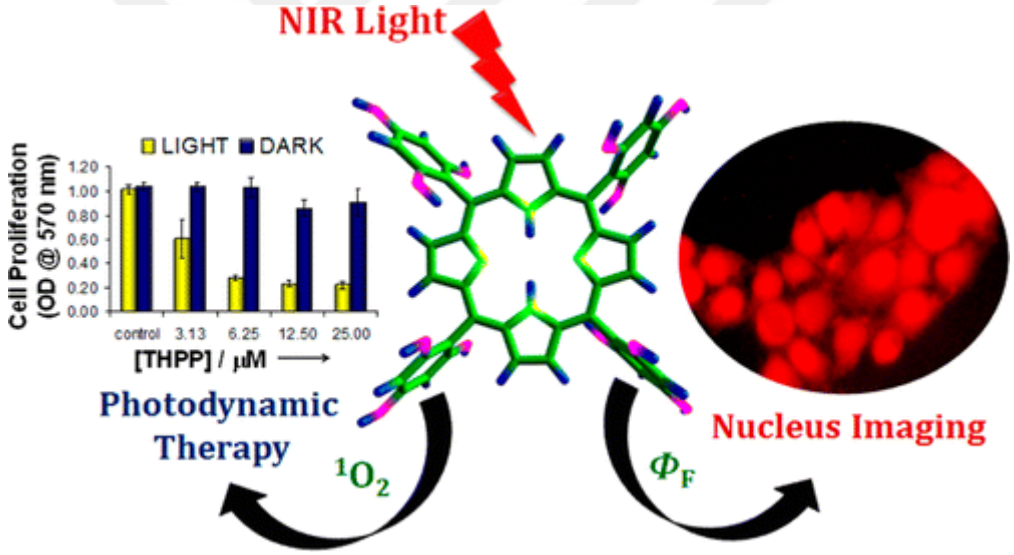

Figure 1.11: Photodynamic effect and cellular image of cancer cells treated with THPP. (Reprinted with permission from [89]. Copyright 2013, American Chemical Society)

1.2.3.2 Conjugated Polymer Nanoparticles

Recently, nanostructures based on conjugated polymers have started to emerge as effective photosensitizers for antimicrobial and anticancer photodynamic therapy due to their unique electronic and optical properties showing strong light-harvesting capability, high singlet oxygen quantum yield, tunable optical spectrum and less-cytotoxicity compared to

conventional dyes and quantum dots. [27-36] Conjugated polymer nanoparticles can be prepared mainly by nanoprecipitation [39-44] and mini-emulsion [37,38] methods. Mini-emulsion involves the use of surfactants, but in nanoprecipitation, no surfactants are needed. In nanoprecipitation, the polymer is dissolved in water-miscible solvents like THF. This organic phase is injected into an aqueous solution while stirring with sonication. After removing the organic solvent, nanoparticles of the conjugated polymer are obtained (Figure 2).

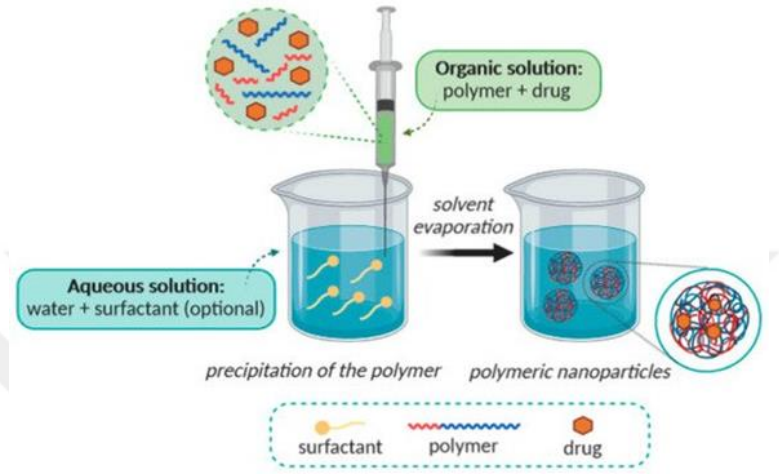

Figure 1.12: Schematic illustration of the nanoprecipitation method. Reprinted with permission from [87]

Applications of conjugated polymer nanoparticles include sensors, actuators, flexible displays, discrete electronics, and smart fabric. The use of conjugated polymer-based nanoparticles as a chemical or biological sensor is possible due to their sensitivity to the physical conditions of the surrounding environment, such as chemical composition, pH, permittivity, humidity, and temperature. [45-47]

Elgiddawy *et al*. have investigated antimicrobial activity of cationic poly(3-hexylthiophene) nanoparticles (Figure 1.13). In this work, poly(3-hexylthiophene) P3HT-based nanoparticles (NPs) were prepared by mini-emulsion method using cetyltrimethylammonium bromide (CTAB) as a stabilizer. [48] The antimicrobial activity of the nanoparticles on bacteria and fungi was investigated. The minimum inhibitory concentration (MIC) of *E. coli* and *S. aureus* was determined to be 2.5 µg/mL, while for *C. albicans* it was 0.312 µg/mL.

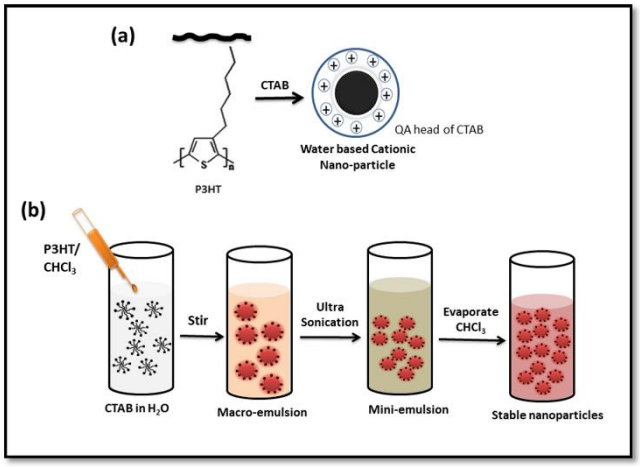

Figure 1.13: Schematic illustration of nanoparticle formation for CTAB-P3HT (a), Scheme for the synthesis of nanoparticles by mini-emulsion process (b).

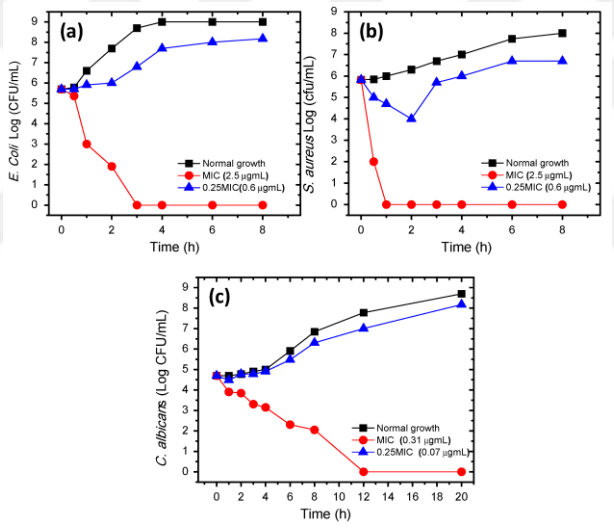

Figure 1.14: Time-killing curves for CTAB-P3HT NPs against (**a**) *E. coli*, (**b**) *S. aureus* and (**c**) *C. albicans* isolates. Blackline = Growth control, red line = MIC and blue line = 1/4 MIC. Reprinted from [48].

Yuan *et al*. reported a conjugated polymer-quantum dot hybrid material (PFP/QD) constructed using fluorescence resonance energy transfer (FRET) process (Figure 1.15). [49] The hybrid nanomaterial consists of water-soluble anionic CdSe/ZnS QDs (QDs) and cationic poly (fluorene-alt-phenylene) derivatives by electrostatic interaction, promoting FRET between PFP and QD. From light-induced antimicrobial results, a killing efficiency of 100, 77 and 33% was achieved for *E. coli*, *S. aureus* and *C. albicans* when treated with PFP/QD and irradiated with light for 15 min.

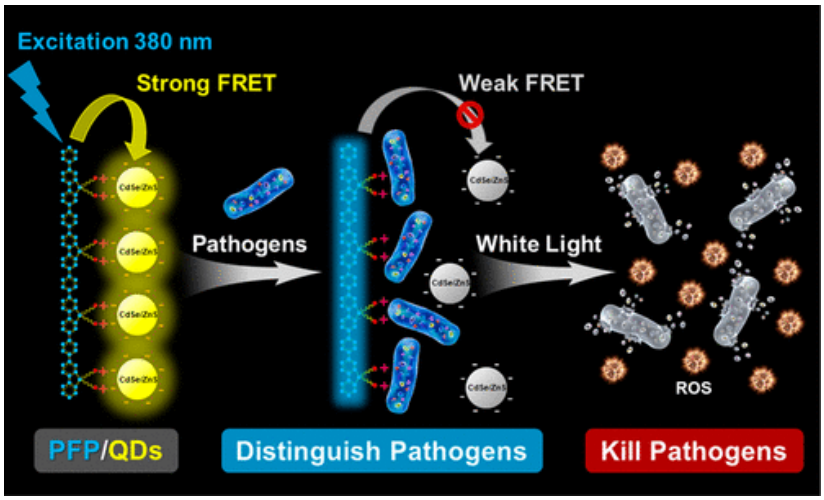

Figure 1.15: Schematic representation of PFP/QD Complex to Achieve Pathogen Identification and Antimicrobial Capabilities. (Reprinted with permission from [49]. Copyright 2020, American Chemical Society)

Parthasarathy *et al*. reported an imidazolium functionalized poly(phenylene ethynylene) (PPE)-based conjugated polyelectrolytes, namely PIM-2 and PIM-4 (Figure 1.16). [50] The polymers are very fluorescent, and they exhibit an amplified quenching effect when low concentrations of the anionic electron acceptor anthraquinone disulfonate are added. The photodynamic antimicrobial activity of the nanoparticles was investigated on Gram-negative *E. coli* and Gram-positive *S. aureus* bacteria both in the dark and under blue-light irradiation. From their results, about 3 log-killing efficiency was recorded when the bacteria were treated with nanoparticles (10 μg mL–1) and illuminated with light (30–60 min).

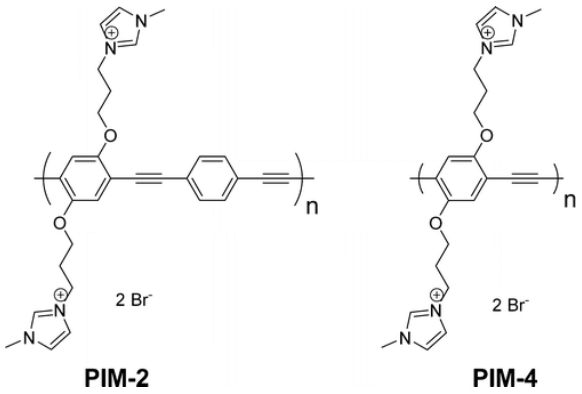

Figure 1.16: Structures of the imidazolium functionalized polyelectrolytes.

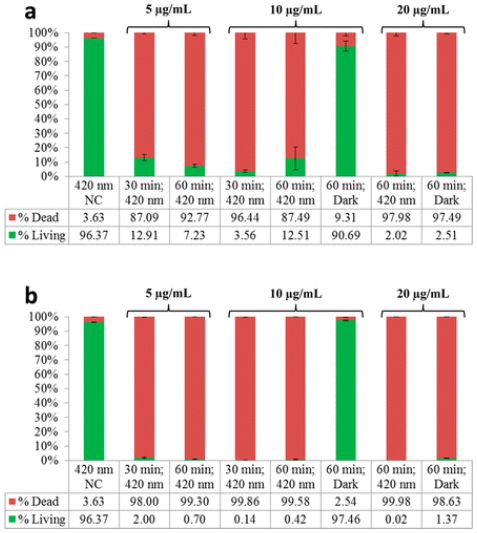

Figure 1.17: Viability E. coli against (a) PIM-2 and (b) PIM-4 upon exposure to blue-violet light for various times. (Reprinted with permission from [50]. Copyright 2015, American Chemical Society)

Peng *et al.* investigated the photothermal effect of fluorene-based conjugated oligomer (OF-Green-N) on *E. coli* (Figure 1.18). [82] The photothermal conversion efficiency of OF-Green-N (10 μg/mL) was measured to be 37.7% when irradiated with an 808 nm laser. When the suspension of *E. coli* was treated with OF-Green-N (0.06 mg/mL) and illuminated with a laser, almost all the bacteria were killed. Also, OF-Green-N showed high dark cytotoxicity due to the presence of quaternary ammonium groups.

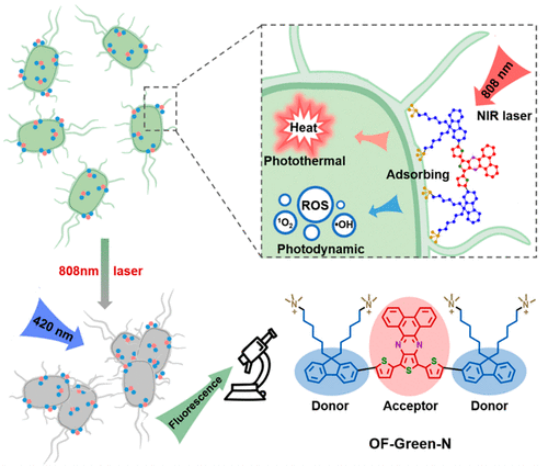

Figure 1.18: Schematic representation of OF-Green-N for killing bacterial. (Reprinted with permission from [82]. Copyright 2020, American Chemical Society)

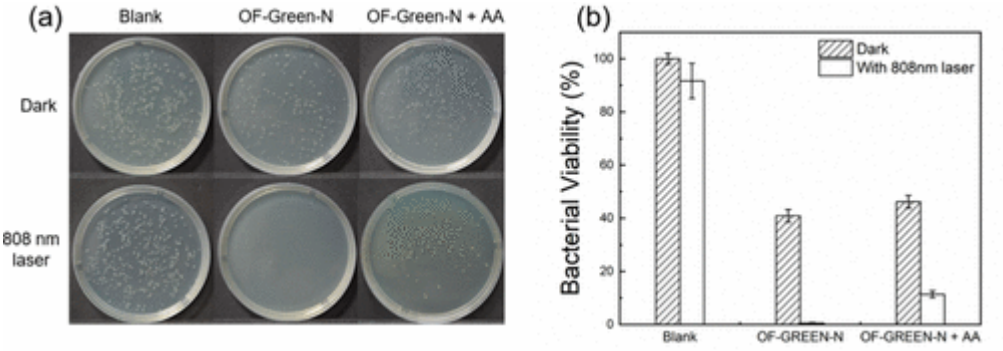

Figure 1.19: (a) Photographs and (b) viability of *E. coli* c incubated with OF-Green-N, and OF-Green-NAA in the dark and under laser exposure. (Reprinted with permission from [82]. Copyright 2020, American Chemical Society)

Guo *et al*. reported conjugated polymer-based organic nanoparticles (PDCP-NPS) as a bactericidal agent. [83] The nanoparticles were prepared using the nanoprecipitation method. PDCP-NPS was utilized in both *in vitro* and *in vivo* as a photosensitizer. Almost all the bacteria were killed when they were incubated with PDCP-NPS (50 mg/mL) and illuminated with light. PDCP-NPS showed almost no cytotoxicity against 293T, EA.hy926, HeLa, A549 mammalian cells.

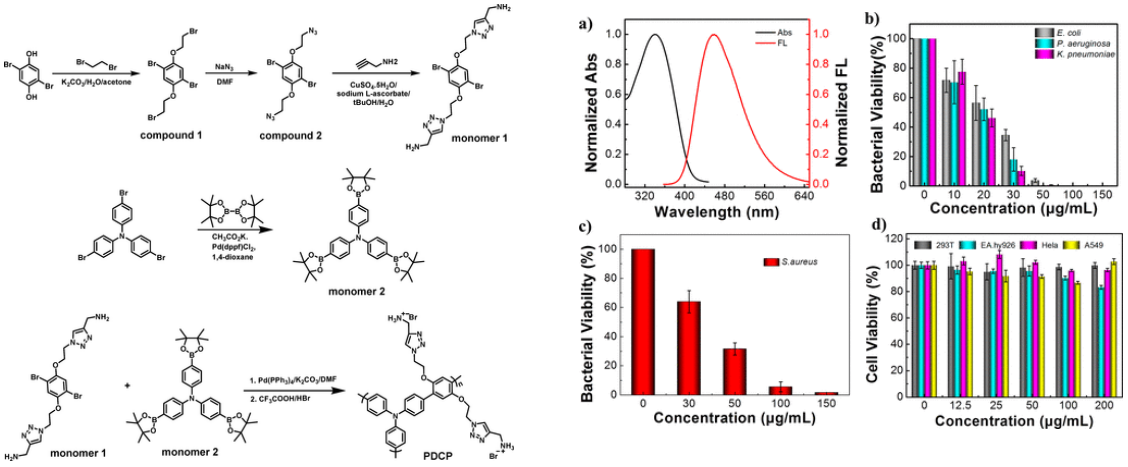

Figure 1.20: (a) Normalized UV–vis absorption and fluorescence spectrum of PDCP-NPs in aqueous solution. (b) Antibacterial activity of PDCP-NPs against *P. aeruginosa*, *K. pneumoniae*, and Amp^r*E. coli*. (c) Antibacterial activity of PDCP-NPs against *S. aureus*. (d) Cytotoxicity of PDCP-NPs on mammalian cells: 293T, EA.hy926, HeLa, A549. (Reprinted with permission from [83]. Copyright 2020, American Chemical Society)

Cai *et al*. synthesized a hyaluronic acid-functionalized diketopyrrolopyrrole based photosensitizer (DTDPPBr2–HA) with a remarkable targeting and photodynamic therapy efficacy for both in vitro and in vivo studies (Figure 21). [90] From their cell culture experiment results, cell viability of HCT-116 decreased to about 10% when treated with DTDPPBr2–HA (1 mg/mL) followed by illumination with light (40 mW/cm^2). In the dark, DTDPPBr2–HA showed minimal dark cytotoxicity.

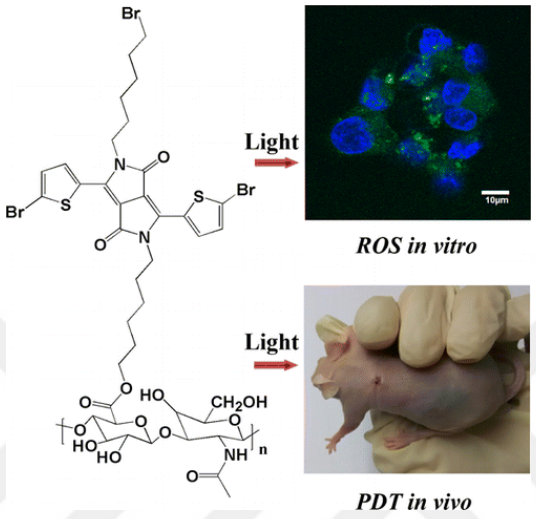

Figure 1.21: DTDPPBr2–HA in both *in vivo* and *in vitro* studies. (Reprinted with permission from [90]. Copyright 2016, American Chemical Society).

Özkan *et al.* prepared a hybrid conjugated oligomer-gold nanoparticles (COL-Au-NPs) using the nanoprecipitation method. COL-Au-NPs was utilized in a combined photodynamic-photothermal therapy as well as in cellular imaging. [91] The nanoparticles were toxic in the dark against bacteria and MCF-7 cancer cells due to the presence of amine pendant groups. When the nanoparticles were capped with cucurbit[7]uril (CB7@COL-Au-NPs) the dark cytotoxicity of the nanoparticles were reduced significantly.

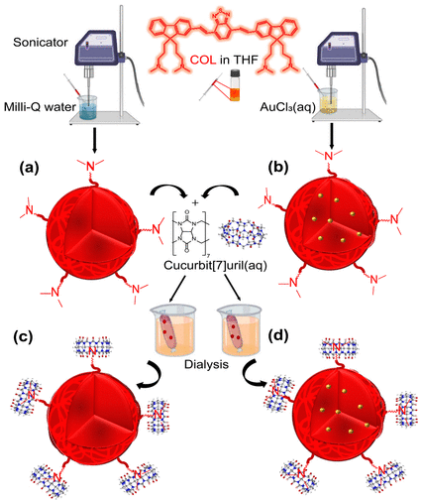

Figure 1.22: Schematic Overview of the Preparation of (a) COL-NPs and (b) COL-Au-NPs and Complexation of Amine Residues of NPs with CB7, (c) CB7@COL-NP and (d) CB7@COL-Au-NPs. (Reprinted with permission from [91]. Copyright 2020, American Chemical Society).

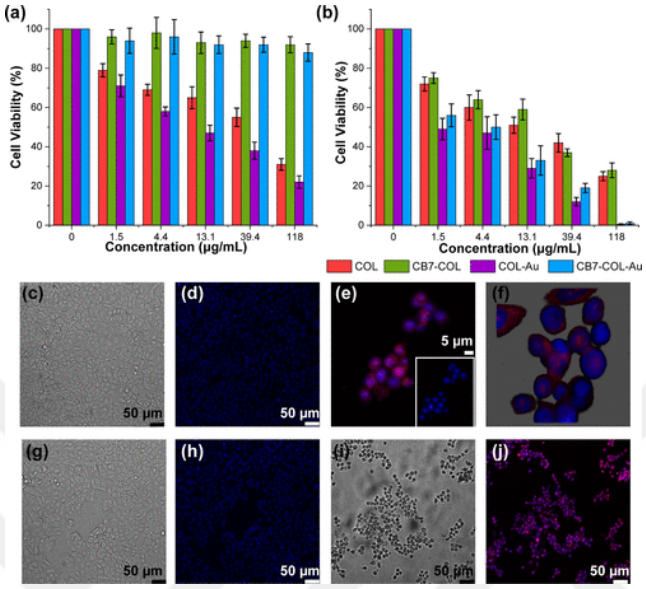

Figure 1.23: Relative cell viability (%) of MCF-7 cells treated with various concentrations of COL-NPs, CB7@COL-NPs, COL-Au-NPs, and CB7@COL-Au-NPs: (a) in the dark and (b) under continuous white light irradiation (20 min, 20 mW/cm^2). MCF-7 cells of the nontreated DMEM control group in the dark. (c) DIC image and (d) CLSM image, and nuclei were stained with DAPI. (e) MCF-7 cells were treated with 1 μM COL-Au-NPs and exposed to light. (f) Three-dimensional image of COL-Au-NP-treated MCF-7 cells. (g) DIC image of the nontreated light control group. (h) CLSM image of the nontreated light control group. (i) DIC image of the COL-Au-NP-treated dark group. (j) CLSM image of the COL-Au-NP-treated dark group. (Reprinted with permission from [91]. Copyright 2020, American Chemical Society).

1.2 Aim of Study

In this study, we report the synthesis and characterization of novel water dispersible and mechanically stable conjugated polymer-based nanoparticles which can generate singlet oxygen more efficiently, show minimal dark cytotoxicity, and high light induced biocidal activity. All these features make the nanoparticles an ideal photosensitizer. Two photosensitizers namely conjugated polymer-porphyrin nanoparticles (**CPPN**) (Figure 1.25) and cross-linked conjugated polymer nanoparticles (**PCP**) (Figure 1.24) will be synthesized.

Porphyrin is selected as a cross-linker to investigate the effect it has on the overall reactive oxygen species (ROS) generation of the nanoparticles.

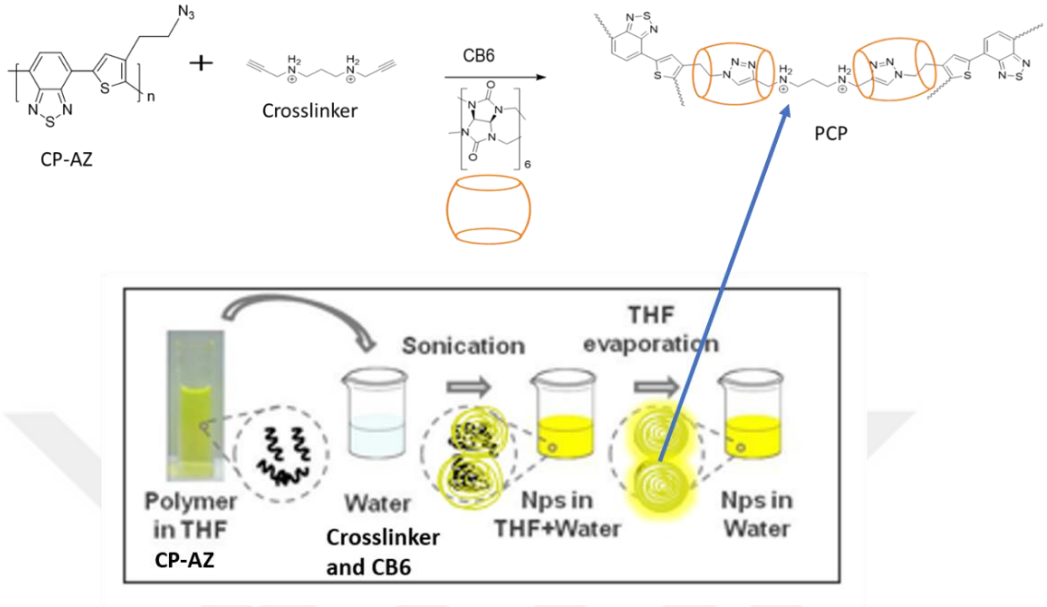

Figure 1.24: Preparation of cross-linked conjugated polymer nanoparticles (**PCP**)

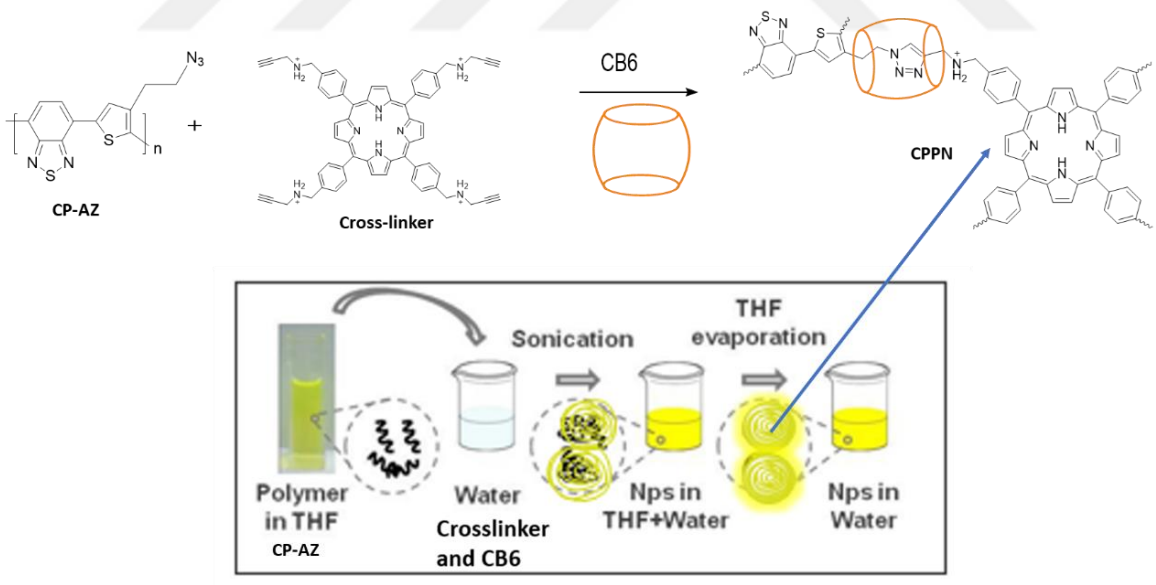

Figure 1.25: Preparation of conjugated polymer-porphyrin nanoparticles (**CPPN**).

The conjugated polymer-based nanoparticles will be prepared in one pot using the nanoprecipitation method by cross-linking a hydrophobic azide-functionalized conjugated

polymer (**CP-AZ**) with a water-soluble propargylamine-functionalized porphyrin (**TPP-4AL**) and, N, N′-di-prop-2-ynyl-propane-1,3-diamine hydrochloride through cucurbit[6]uril-(**CB6**)-catalyzed azide-alkyne cycloaddition (**CB6-AAC**) reaction (Figures 1.24 and 1.25). [51-53] **CB6** is a macrocycle and is a homologue of the CBn family with six glycoluril (n=6) units. [54] **CB6** have a hydrophobic cavity and two hydrophilic portals, each with six carbonyl groups. It can encapsulate hydrophobic guests of suitable sizes in its cavity and complex with cationic guests through ion-dipole interaction.

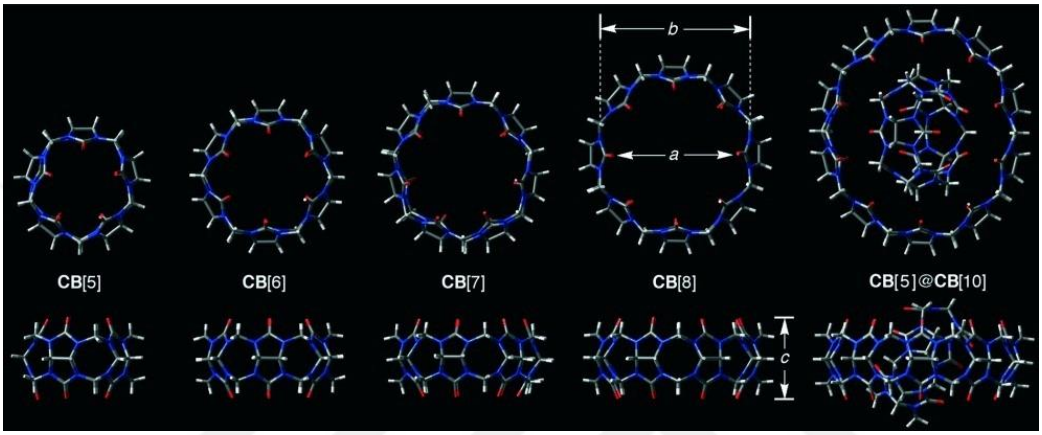

Figure 1.26: X-ray crystal structures of CBs (Reprinted with permission from [92] Copyright, 2005 John Wiley & Sons, Ltd.).

CB	M_w (g/mol)	a (Å)	b (Å)	c (Å)	d (Å)	V (Å^3)
CB5	830	2.4	4.4	9.1	13.1	82
CB6	996	3.9	5.8	9.1	14.4	164
CB7	1163	5.4	7.3	9.1	16.0	279
CB8	1329	6.9	8.8	9.1	17.5	479
CB10	1161	9.5-10.6	11.3-12.4	9.1	20.0	870
iCB6	996	4.3-3.9	3.8-5.8	9.1	10.7-14.4	-
iCB7	1163	6.7-5.4	5.4-7.3	9.1	11.2-16.0	-

Table 1.1: Structural parameters of common CB homologues and inverted CBs (Mw= molecular weight, a=portal diameter, b=cavity diameter, c=height, d=outer diameter, V=cavity volume).

CB6 can also catalyze 1,3-dipolar cycloaddition between alkyne and azide, forming a triazole. In the preparation of conjugated polymer-based nanoparticles, CB6 will act as a catalyst for alkyne-azide cycloaddition reaction, and the use of Cu(I) as a catalyst will be avoided because even a small amount of Cu is known to cause toxicity for biological applications. [55] Secondly, the introduction of positive charges into the nanoparticles through

the cross-linking causes repulsion between the nanoparticles and prevents aggregation of the nanoparticles without the need for any surfactant. In addition, the positive charges allow the negatively charged bacteria membrane to interact with nanoparticles more effectively, thereby increasing the photodynamic effect of the nanoparticles. [56-59] Although the cationic head groups are known to cause dark cytotoxicity, CB6 forms ion-dipole interaction with them, and this will reduce their dark cytotoxic effect. [60] The nanoparticles will be utilized as a photosensitizer in PDT to study the biocidal activity against Gram-negative (E. *coli*) and Gram-positive (*B. Subtilis* and *S. aureus*) bacteria. Furthermore, the cytotoxicity of the conjugated polymer-based nanoparticles against MCF-7 breast cancer cells will be studied in the dark and under light irradiation.

In addition, we will encapsulate gold into the conjugated polymer-based nanoparticles to enhance the ROS generation ability through the improved intersystem crossing. Since gold nanoparticles have localized surface plasmon resonance (LSPR) in the near-infrared region of the electromagnetic spectrum, the nanoparticles can be used in photothermal therapy.

Chapter 2

Experimental

2.1 Materials

All chemicals used in the chemical syntheses were of analytical grade and used as received. Milli-Q water (18.2 MΩ cm at 25 ^{0}C) was used when needed. Column chromatography was done using silica gel purchased from Sigma-Aldrich (high-purity grade, with a pore size of 60 ˚A, 70-230 mesh, 63-200 pm) or Sephadex G-15 medium. Reaction steps were followed by thin-layer chromatography (TLC) using silica-coated (Merck TLC Silica Gel F254) TLC plates, visualizing by shortwave (254 nm) or longwave (365 nm) LTV light. Deuterated solvents ($CDCl_3$ and D_2O) used in NMR spectroscopy were obtained from Merck.

For the bacterial assays, Escherichia coli DH5-α strain (Gram-negative), Bacillus subtilis MTCC 441 strain (Gram-positive) and Staphylococcus aureus ATCC 6538 strains were used for bacteria assays. To prepare liquid lysogeny broth (LB) as a nutrient medium for bacteria and semi-solid LB agar, sodium chloride, tryptone, yeast extract, and agar powder were obtained from Sigma-Aldrich. Whatman qualitative filter paper Grade 3 was used for the agar disk diffusion assay, and ampicillin was purchased from Sigma-Aldrich. For SEM imaging of bacteria, a glutaraldehyde solution was purchased from Merck.

For the cell culture experiment, Gibco Dulbecco's Modified Eagle Medium (DMEM), L-glutamine, and sodium pyruvate were obtained from Sigma-Aldrich. Moreover, Fetal Bovine Serum (FBS) and penicillin/streptomycin (Pen-strep) were from Thermo Fischer Scientific, and MEM non-essential amino acids solution was obtained from Merck. PBS (10X) was purchased from Sigma-Aldrich and 1X PBS was obtained by 10-fold dilution of 10X PBS with deionized water and then it was autoclaved.

2.2 Characterization Techniques

2.2.1 ^{1}H and ^{13}C Nuclear Magnetic Resonance (NMR) Spectroscopy

Bruker AVANCE DPX-400 NMR spectrometer operating at 400 MHz and 100 MHz for ^{1}H-NMR and ^{13}C-NMR respectively were used to obtain ^{1}H NMR and ^{13}C NMR spectra of the samples. All spectra measurements were recorded at 25 ^{0}C and dissolving samples in deuterated solvents. The chemical shifts are in ppm relative to the internal standard tetramethylsilane (TMS). Also, spin multiplicities are represented with the following notations: s (singlet), d (doublet), t (triplet), q (quartet), m (multiplet).

2.2.2 Electrospray Ionization-Mass Spectrometry

Agilent 6224 Accurate-Mass Time-of-Flight (TOF) LC/MS and Agilent 6530 Accurate Mass Q-TOF LC/MS systems were used to analyze the exact molecular weight of the product.

2.2.3 F T -IR Spectroscopy

The functional groups of the samples are analyzed using Bruker Alpha-II Platinum ATR FT-IR spectrometer. The spectra were recorded in the range of 400-4000 cm^{-1}, and the resolution was 2 cm^{-1}.

2.2.4 UV-Vis Absorbance Spectroscopy

Absorption spectra of the samples were recorded using Cary 300 UV-vis spectrophotometer equipped with a Xenon flash lamp.

2.2.5 Fluorescence Spectroscopy

All fluorescence spectra were recorded in the solution phase on the Varian Cary Eclipse fluorescence spectrophotometer with a quartz cuvette with a 10 mm path length.

2.2.6 Dynamic Light Scattering (DLS) and Zeta Potential

The size and zeta potential of nanoparticles was measured using Malvern Zetasizer Nano ZS equipped with 663 nm laser at 25 ^{0}C. DLS measurements were recorded using standard fluorescence cuvette, while zeta potential measurements were obtained using folded capillary zeta cells.

2.2.7 Scanning Electron Microscopy (SEM)

The morphology of nanoparticles and bacteria were visualized on Quanta 200 FEG Thermo Fisher Scientific operating at environmental scanning electron microscopy mode.

2.2.8 Transmission Electron Microscopy (TEM)

The morphology of nanoparticles was visualized on FEI Tecnai G2 F30 transmission electron microscope.

2.2.10 Microplate Reader

The optical density of bacteria at 600 nm (OD_{600}) and the absorbance of the MTT assay (570 nm) was obtained using SpectraMax M5 multi-detection microplate reader system.

2.2.11 Critical Point Dryer (CPD)

Bacteria for SEM imaging were dried by Autosamdri-934 Tousimis CPD in a cleanroom using CO_2 at 7.4 MPa, 30 ^{0}C using ethanol as an intermediate fluid.

2.3 Synthesis

2.3.1 Synthesis of 5,10,15,20-tetrakis(4-(bromomethyl) phenyl) porphyrin (TPP-Br)

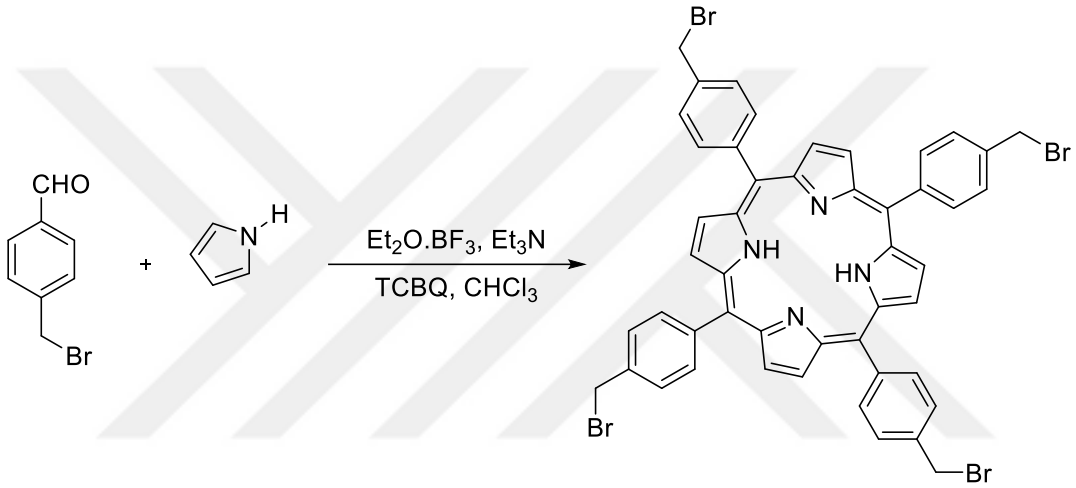

To degassed chloroform (1 L) in a 2L flask, 1.5 g of 4-(bromomethyl) benzaldehyde, pyrrole (0.543 mL) and BF_3OEt_2 (0.31 mL) was added. The flask was covered with aluminum foil and stirred for 1h. Then triethylamine (0.421 mL) and TCBQ (1.39 g) were added and stirred overnight. After that, the mixture was refluxed for 1 hr at 50 ^oC and allowed to cool down to room temperature. The solvent was evaporated using a rotary evaporator. The remaining solid was dissolved in toluene. The product was purified by passing it through silica gel. After removing the solvent, the product was washed with methanol. The purple solid was dried at 60 ^oC under a vacuum.

Yield: 794 mg, 43%.

^{1}H-NMR (400 MHz, $CDCl_3$, RT) δ (ppm): 8.867 (s, 8 H), 8.205 (d, 8 H), 7.811 (d, 8 H), 4.884 (s, 8 H), -2.783 (s, 2 H).

2.3.2 Synthesis of Prop-2-ynyl-4-[10,15,20-tris-(4-prop-2-ynyl aminom-ethylphenyl)- porphyrin-5-yl]-benzyl-amine (TPP-4AL)

KD1 (152.90 mg, 0.155 mmol) was dissolved in DCM and added to propargylamine (2 mL, 29 mmol) dropwise in a round-bottomed flask while stirring. The mixture was stirred for 72 h, and then 0.1 N NaOH (10 mL) was added to the reaction mixture while stirring for an hour. Extraction was done using DCM (50 mL) three times. The solvent was removed with rotavap, and the remaining purple solid was dried at 65 ^{o}C under vacuum.

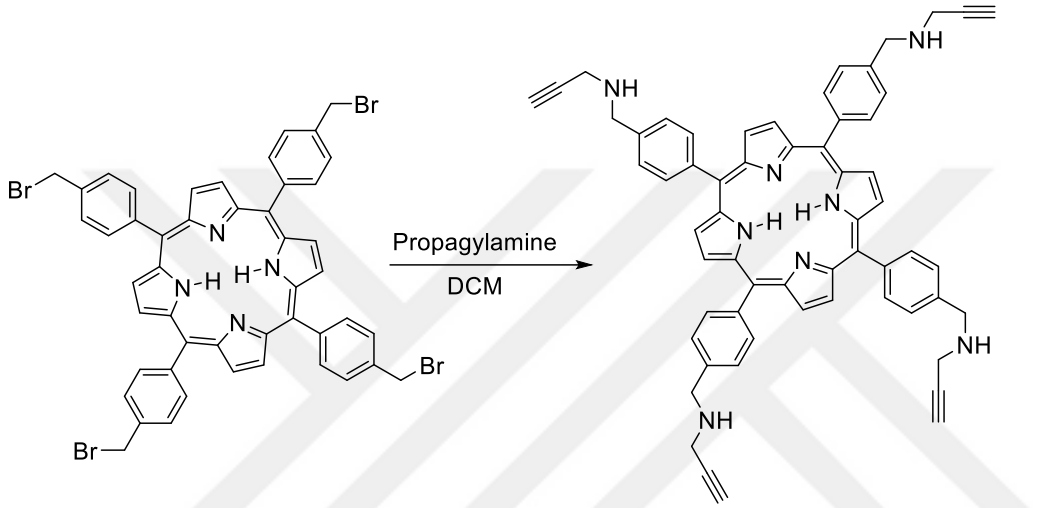

Yield: 120 mg, ~80%.

^{1}H-NMR (400 MHz, CDCl3, RT) δ (ppm): 8.9 (s, 8 H), 8.7 (d, 8 H), 7.7 (d, 8 H), 4.3 (s, 8 H), 3.7 (d, 8 H), 2.4 (t, 8H) -2.7 (s, 2 H).

2.3.3 Synthesis of Azide-functionalized Red-Emitting Conjugated Polymer (CP-AZ)

The red-emitting conjugated polymer has been synthesized and reported in our group`s previous work. [61] The synthesis pathway is depicted below.

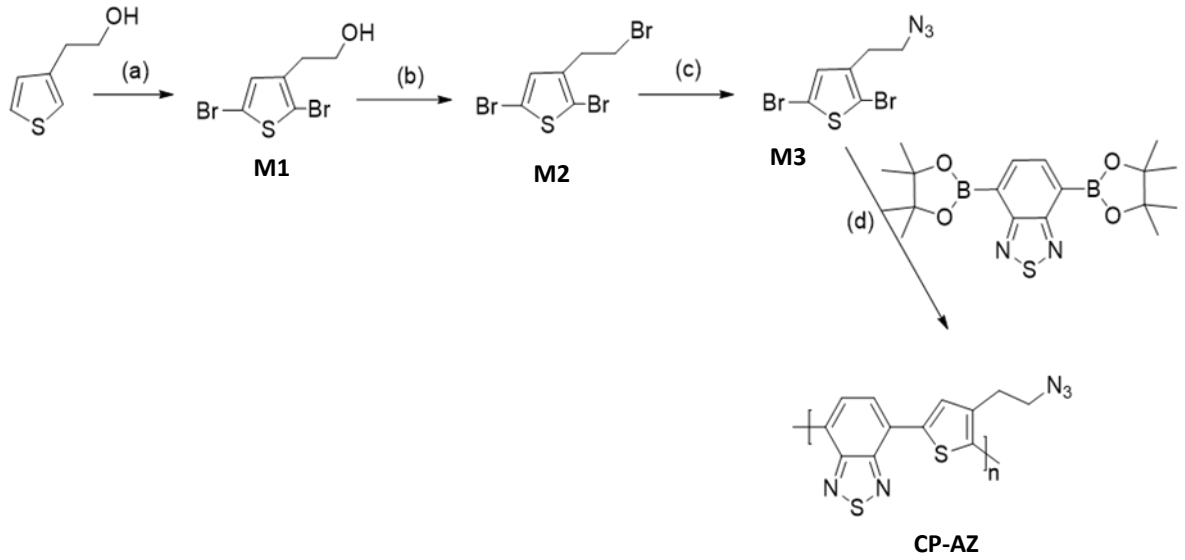

(a) **M1:** NBS, EtOAc, RT, overnight; (ii) **M2:** PPh_3, CBr_4, THF, RT, 24 h; (iii) **M3:** NaN_3, DMSO, RT, 72 h; (iv) **CP-AZ**: $Pd(PPh_3)_4$, TBAB, K_2CO_3, THF, Toluene, H_2O, 55°C, 72 h, N_2.

2.3.4 Synthesis of N^1, N^3-di(prop-2-yn-1-yl)propane-1,3-diamine dihydrochloride (KD2)

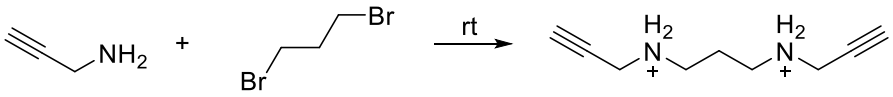

0.7 g (3.6 mmol) of 1,3-dibromopropane was added dropwise to an excess amount of propargylamine (2 g, 36.3 mmol) at room temperature, and it was stirred for 48 h. Then 0.1 N NaOH (5 mL) was added to the reaction mixture and stirred for 1 h. The solvent was removed using rotavap, and the remaining yellow solid was dissolved in diethyl ether. The mixture was placed in an ice bath, and 0.1 N HCl in diethyl ether (5 mL) was added dropwise. The mixture was subjected to stirring for 4 h, and the precipitate was collected. Recrystallization was done in ethanol to yield the product.

^{1}H-NMR (400 MHz, D_2O, 25^{O}C) ppm: 2.05 (m, 2H, d), 2.90 (d, 2H, a), 3.25 (t, 4H, c), 3.75 (s, 4H, b).

2.3.5 Crosslinked Conjugated polymer Nanoparticles

The cross-linked nanoparticles were synthesized according to our previously reported procedure. [55] Cross-linked nanoparticles were prepared by CB6 catalyzed click reaction between the azide functionalized polymer (CP-AZ) and alkyne functionalized crosslinkers (TPP-4AL and KD2). The nanoparticles were synthesized by varying the ratio of polymer to crosslinker concentration.

2.3.5.1 Crosslinked Nanoparticles between CP-AZ and TPP-4AL (CPPN)

(a) TPP-4AL:CP-AZ (1:2): 1 mg of the conjugated polymer was dissolved in 3 mL of THF. CB6 (7 mg, 4 equivalents) was dissolved in 0.1 N HCl and stirred for some time to get a homogeneous solution. Porphyrin (0.5 mg) was added to the above solution and stirred for about 15 min, and the volume was made up to 100 mL with deionized water. The polymer solution was injected rapidly into the above solution under vigorous stirring. The mixture was stirred with sonication for 1 h at room temperature and, then the dispersion was left overnight at room temperature. The remaining solution was concentrated to the required volume and was dialyzed using a 14 kDa MWCO regenerated cellulose membrane for 24 h to remove excess CB6 and any unreacted species.

(b) TPP-4AL:CP-AZ (1:4): 2 mg of polymer (P1) was dissolved in 3 mL of THF. CB6 (7 mg, 4 equivalents) was dissolved in 0.1 N HCl and stirred for some time to get a homogeneous solution. Porphyrin (0.5 mg) was added to the above solution and stirred for about 15 min, and the volume was made up to 100 mL with deionized water. The polymer solution was injected rapidly into the above solution under vigorous stirring. The mixture was stirred with sonication for 1hr at room temperature and, then the dispersion was left overnight at room temperature. The remaining solution was concentrated to the required volume and was dialyzed using a 14 kDa MWCO regenerated cellulose membrane for 24 h to remove excess CB6 and any unreacted species.

(c) TPP-4AL:CP-AZ (1:6): 3 mg of polymer (P1) was dissolved in 3 mL of THF. CB6 (7 mg, 4 equivalents) was dissolved in 0.1 N HCl and stirred for some time to get a homogeneous solution. Porphyrin (0.5 mg) was added to the above solution and stirred for about 15 min, and the volume was made up to 100 mL with deionized water. The polymer solution was injected rapidly into the above solution under vigorous stirring. The mixture was stirred with sonication for 1hr at room temperature and, then the dispersion was left overnight at room temperature. The remaining solution was concentrated to the required volume and was dialyzed using a 14 kDa MWCO regenerated cellulose membrane for 24 h to remove excess CB6 and any unreacted species.

2.3.5.2 Crosslinked Nanoparticles between CP-AZ and KD2 (PCP)

(a) KD2:CP-AZ (1:2): 1 mg Polymer was dissolved in THF (2 ml). CB6 (5.4 mg, 2 equivalents) was dissolved in 0.1 N HCl and stirred for some time to get a homogeneous solution. From stock solution of N,N′-di-prop-2-ynyl-propane-1,3-diamine hydrochloride (KD5) (5 mg in 5 mL water) 0.5 mL was added to the CB6 solution and stirred for 15 min. Its volume was made up to 100 mL by adding deionized water. The polymer solution in THF was injected rapidly into the above solution while stirring with sonication for 1 h at room temperature. The mixture was left overnight. The remaining solution was concentrated to the required volume, and dialysis was done using a 14 kDa MWCO regenerated cellulose membrane for 24 h to remove the excess CB6 and any unreacted species.

(b) KD2:CP-AZ (1:4): 2 mg Polymer was dissolved in THF (2 ml). CB6 (5.4 mg, 2 equivalents) was dissolved in 0.1 N HCl and stirred for some time to get a homogeneous solution. From stock solution of N,N′-di-prop-2-ynyl-propane-1,3-diamine hydrochloride (KD5) (5 mg in 5 mL water) 0.5 mL was added to the CB6 solution and stirred for 15 min. Its volume was made up to 100 mL by adding deionized water. The polymer solution in THF was injected rapidly into the above solution while stirring with sonication for 1 h at room temperature. The mixture was left overnight. The remaining solution was concentrated to the required volume, and dialysis was done using a 14 kDa MWCO regenerated cellulose membrane for 24 h to remove the excess CB6 and any unreacted species.

(c) KD2-CP-AZ (1:6): 3 mg Polymer was dissolved in THF (2 ml). CB6 (5.4 mg, 2 equivalents) was dissolved in 0.1 N HCl and stirred for some time to get a homogeneous solution. From stock solution of N,N′-di-prop-2-ynyl-propane-1,3-diamine hydrochloride (KD5) (5 mg in 5 mL water) 0.5 mL was added to the CB6 solution and stirred for 15 min. Its volume was made up to 100 mL by adding deionized water. The polymer solution in THF was injected rapidly into the above solution while stirring with sonication for 1 h at room temperature. The mixture was left overnight. The remaining solution was concentrated to the required volume, and dialysis was done using a 14 kDa MWCO regenerated cellulose membrane for 24 h to remove the excess CB6 and any unreacted species.

Although the click reaction was done by varying the ratio of the polymer, the ideal ratio that led to nanoparticles that are stable and effective was obtained in 1:4 (KD2:CP-AZ and TPP-4AL:CP-AZ) ratio. The crosslinked nanoparticles in the ratio 1:4 were used for further studies.

2.3.5.3 Synthesis of CPPN-Au and PCP-Au Nanoparticles

An aqueous solution of 0.1 μM $AuCl_3$ was placed in a beaker, and the volume was made up to 100 mL with deionized water. After that, the procedure used for CPPN and PCP synthesis was repeated.

2.3.6 Reactive oxygen species (ROS) measurement

We measured the ROS generation ability of nanoparticles following the previously reported procedure. [128,129] 2.5 mg of dichlorofluorescein diacetate (DCFH-DA) was dissolved in 5 mL ethanol. From the resulting solution, 500 μL was added to 2 mL of 0.01 N NaOH and kept in the dark at room temperature for 30 min. After that, 10 mL of 25 mm of sodium phosphate buffer (PBS) was added to the mixture and kept in the fridge. The concentration of DCFH was 40 μM. For blank measurements, 1 mL of water was added to 500 μL of DCFH in a standard fluorescence cuvette, and the sample was excited at 488 nm. The emission data were collected from 500 nm to 700 nm with a slit width of 5 nm. PL intensity of DCFH was measured (blank 0 min). After this, the solution was irradiated with white light (1mW/cm^2) for 4 min, and the emission spectrum was taken every minute. For CPPN measurements, 5 μg/mL of each nanoparticle was added to 500 μL of DCFH and was diluted with 1 ml of deionized water. The same procedure used for the blank measurements were used to detect ROS generation of CPPN.

2.3.7 Bacterial Experiments

2.3.7.1 Bacteria Solution Preparation and Minimum Inhibitory Concentration (MIC) Assay

The broth microdilution method was used to predict the MIC values of the nanoparticles. To prepare a bacterial suspension, an E. coli colony on an agar plate was transferred to a 5 ml Luria-Bertani (LB) culture medium and incubated (37 ^{0}C, 200 rpm) for 14 h. Next, the suspension was centrifuged and further washed with 10 mM PBS to remove the LB medium. The optical density (OD) was adjusted to 1.0 using PBS. The same procedure was used to prepare B. subtilis and S. aureus suspensions

For MIC assay, 100 µL of bacterial suspension was placed in 1.5 ml Eppendorf tubes, and the 5 µL different concentrations of nanoparticles were added to the tubes. For the control groups, an equal volume of PBS was added. Blank and nanoparticles containing tubes were irradiated with white light (22 mW/cm^2) for 10min. The same procedure was repeated for the dark groups. After that, the Eppendorf tubes were placed in the incubator for 16 h. Finally, the mixture was transferred to 96-Well microplates, and the OD was measured using a microplate reader. [130]

2.3.7.2 Antibacterial activities of the nanoparticles (CPPN)

After the MIC was determined, which was 20 µg/mL for CPPN, to a 1 mL E. coli suspension in 1.5 ml Eppendorf tube, 50 µL of CPPN was added and incubated for 15 min at 200 rpm. Then the dark groups were kept in the dark while the light groups were irradiated for 10 min using white light (22 mW/cm^2). After that, bacterial suspension was diluted 10^4-fold in PBS, and 100 mL of it was spread on an LB agar plate and incubated for 14 h at 37 ^{0}C. Next, the number of colonies formed were counted. The same procedure was followed for Gram-positive bacteria (B. subtills and S. aureus).

2.3.7.3 Preparation of Bacteria for SEM Imaging

E. coli, B. subtilis and S. aureus suspensions (OD_{600} = 1.0) were incubated with CPPN for 15 minutes in an incubator (37 ^{0}C, 200 rpm). The mixture was irradiated with white light (22 mW/cm^2) for 10 min while the dark groups were not exposed to light. Organic contamination on silicon wafers (1 cm * 1 cm) was removed by incubating at 37 ^{0}C with isopropanol and pure ethanol (30 min each). Then the clean wafers were placed in six well-plate and dried in an incubator for 30 min. After this, four bacterial samples were prepared; dark-control, light-control, dark-sample and light-sample. 60 µL of each bacterial sample were placed on the silicon wafers in the six well-plate, and the bacterial were fixed onto the wafers using 2.5% glutaraldehyde in PBS. The wafers were kept at 4oC for 14 h. Next, the wafers were washed with PBS and water (two times each), followed by 25% (v/v) ethanol, 50% (v/v) ethanol, 75% (v/v) ethanol, and lastly, with pure ethanol. The wafers were dried using a critical point dryer (CPD), and the wafers were examined under SEM at 15 kV, 3.0 spot size.

2.3.7.4 Zeta Potential Measurement

E. coli, B. subtilis and S. aureus suspensions (OD = 1.0) in 600 µl of PBS were incubated with 20 µg/ml of CPPN and 24 µg/ml of PCP for 15 min. After light treatment for 5 min, the bacteria mixture was centrifuged at 4,000 rpm for 5 min to harvest the bacteria. Next, the bacteria were washed with water and redispersed in water (1 mL). The bacteria suspension was kept in ice for the zeta potential measurement.

2.3.7.5 Disk diffusion assay

In an LB medium, colonies of E. coli, B. subtilis and S. aureus were grown in an incubator (37 ^{0}C, 200 rpm, 16 h). The optical density (OD_{600}) of the bacterial solutions were adjusted to 0.5. From each bacteria suspension, 150 µL were spread evenly on an agar plate. 10 µL of nanoparticles (CPPN) and antibiotic (ampicillin) was placed on a 5 mm circular filter disk. The disk was placed on the agar plates, and the light group were irradiated with white light (22 mW/cm^2) for 10 min. After that, agar plates were incubated at 37 ^{0}C for 14 h. The antibacterial activity of the nanoparticle was observed by measuring the inhibition zone radius.

2.3.8 *In vitro* Experiment

The photodynamic effect of nanoparticles was determined using methyl thiazolyl tetrazolium (MTT) assay.

2.3.8.1 Cell Culture Experiments

MTT was used to determine in vitro dark- and photo-cytotoxicity activities of **CPPN** on the MCF7 breast cancer cell line. The cells were seeded onto 96-well plates at a density of 4×10^3 cells/well and incubated overnight in a carbon dioxide incubator (37 °C, 5% CO_2). Then, the cells were treated with different concentrations of **CPPN** for 24 h. To determine the photo-cytotoxicity, **CPPN** treated cells were irradiated with white light (20 mW/cm) for 20 min. Light treated cells were then placed in the dark for another 24 h at 37 °C. To determine the dark-cytotoxicity, **CPPN** treated cells were incubated in the dark for 48 h at 37 °C. All dilution series of treatment groups and untreated control samples included an equal volume of PBS and DMEM were prepared for each treatment study.

For cell viability assay, thiazolyl blue tetrazolium bromide (MTT) was used. After the medium was removed, the cells were incubated with 110 µL of Gibco Dulbecco's Modified Eagle Medium (DMEM) containing MTT (1.2 mM) for 4 h at 37 °C. Then, 110 µL of SDS-HCl solution (10% SDS in 10 mM HCl) was added to wells to dissolve formazan crystals. After that, the plates were incubated overnight at 37 °C. The cell viability of each well was measured using a microplate reader.

CPPN Light/Dark	Final concentration of CPPN (µg mL^{-1})	CPPN Stock (3 mg mL^{-1}) (µL)	PBS (µL)	DMEM (µL)
Cell control	0	0	60	1540
Conc. 1	3.75	2	58	1540
Conc. 2	9.375	5	55	1540
Conc. 3	18.75	10	50	1540
Conc. 4	37.5	20	40	1540
Conc. 5	75	40	20	1540
Conc. 6	112.5	60	0	1540

Table 2.1: Concentrations of **CPPN** used in MTT cell viability assays.

2.3.8.2 Statistical Analysis

The difference in cell viability was measured by comparing it to the Gibco Dulbecco's Modified Eagle Medium (DMEM) control group. Analysis for dark and light conditions were performed using a 2-way Analysis of variance (ANOVA). (* and ** indicate a significant difference between groups with $p < 0.05$ and $p < 0.0001$, respectively).

Chapter 3

Results and Discussions

In this chapter, there are four sections. In Section 3.1, the synthesis and characterization of the conjugated polymer-porphyrin nanoparticles (CPPN) are covered. Section 3.2 shows the application of CPPN in anticancer and antimicrobial photodynamic therapy. Section 3.3 talks about the synthesis and application of PCP in antimicrobial photodynamic therapy. Section 3.4 talks about the preparation of cross-linked conjugated polymer-gold nanoparticles.

3.1 Synthesis and Characterization of CPPN

3.1.1 Synthesis of 5,10,15,20-tetrakis(α-bromo-p-tolyl)porphyrin (TPP-Br)

We obtained TPP-Br by condensation reaction between α-bromo-p-tolualdehyde (electrophile) and pyrrole (nucleophile) using $Et_2O.BF_3$ (Lewis's acid) as a catalyst. $Et_2O.BF_3$ acts as a catalyst by making α-bromo-p-tolualdehyde more electrophilic, making it more suitable for nucleophilic attack by the pyrrole. A stable intermediate porphyrinogen is formed as a result of the condensation reaction. After the formation of porphyrinogen, triethylamine (Et_3N) is added to the reaction mixture to deprotonate the pyrrolic -NH groups. Then tetrachloro-1,4-benzoquinone (TCBQ) was added to the mixture to obtain TPP-Br.

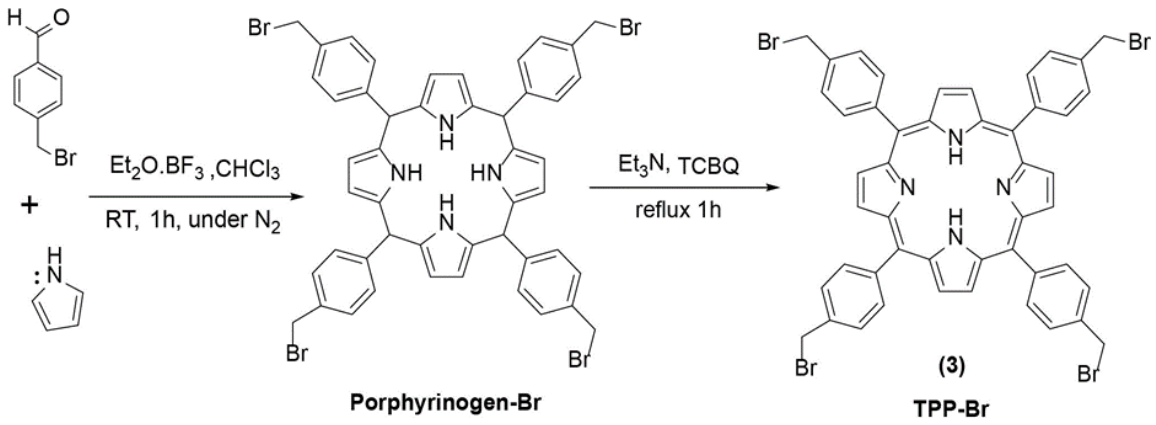

Figure 3.1: Synthesis of TPP-Br

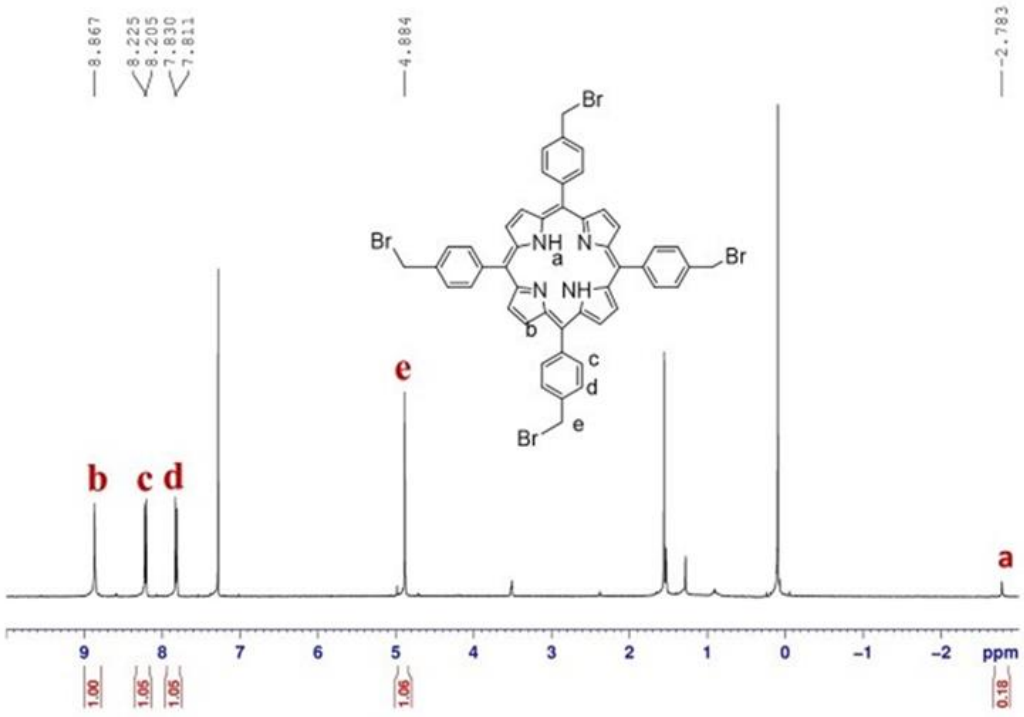

Figure 3.2: ^{1}NMR spectrum of **TPP-Br** (400 MHz, $CDCl_3$, 25 ^{o}C).

To confirm the successful synthesis of TPP-Br ^{1}H-NMR spectroscopy was used and is shown in Figure 3.2. From the ^{1}H-NMR spectrum, a singlet peak at -2.7 ppm was assigned to Pyrrolic N-hydrogens (a) because they are shielded in the aromatic macrocycle. Also, all pyrrolic hydrogens (b) are chemically equivalent and are highly deshielded, and they resonate as a singlet at 8.84 ppm. The benzene hydrogens (c and d) are chemically inequivalent, so they couple to each other to give a doublet at 8.19 and 7.80 ppm, respectively. Singlet peak at 4.80 ppm was attributed to the benzylic hydrogen (e).

3.1.2 Synthesis of Alkyne-substituted Porphyrin (TPP-4AL)

TPP-4AL was synthesized through a nucleophilic substitution reaction. The unbonded nitrogen electrons of propargylamine attack the benzylic carbon of TPP-Br. 0.1 N of NaOH solution was added to the mixture to convert it to a free base. Then, extraction was done with chloroform. The solvent was evaporated using rotavap. After that, the remaining solid was purified using column chromatography at a yield of 80%.

The structure of TPP-4AL was characterized by 1H-NMR (Figure 3.3). The ^{1}H-NMR shows nine different hydrogens, as expected. Singlet peak at -2.7 ppm represents the amine hydrogens inside the porphyrin ring. At 2.4 ppm, triplet was observed (a). The broad singlet at 1.6 ppm (d) is from the protons of the secondary amine. The methylene protons of propargylamine (b) resonate at 3.7 ppm as a doublet. At 4.20 ppm, the singlet peak is assigned to the benzylic (c). Observing higher magnetic field strength for (b) (3.7 ppm) than (c) (4.20 ppm) was expected since the protons are de-shielded. The aromatic protons appear at the downfield region at 7.7 (e) and 8.2 ppm (f) as doublets. The most downfield part of the spectrum contains a peak at 8.8 ppm due to the non-equivalent -pyrrolic protons of porphyrin ring (g) and (h). 7.7 (e) and 8.2 ppm (f) as doublets.

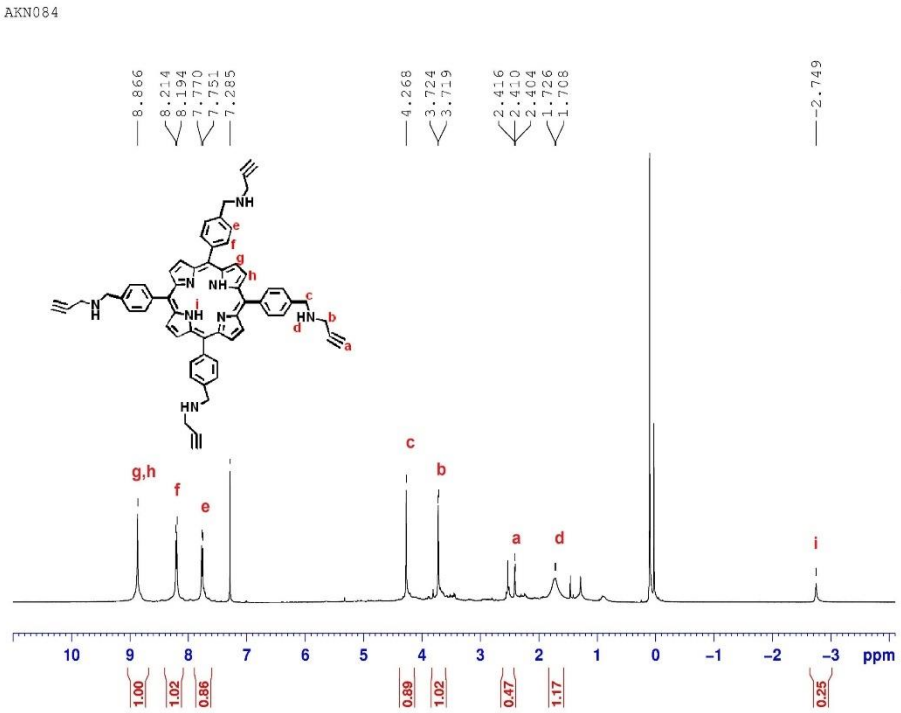

Figure 3.3: ^{1}H-NMR of **TPP-4AL** (400 MHz, $CDCl_3$, 25 ^{o}C).

3.1.3 Synthesis of Azide-functionalized Conjugated Polymer (CP-AZ)

The conjugated polymer has been synthesized, characterized and reported in the previous thesis. [61] Figure 3.5 shows the synthesis of CP-AZ. Bromination reaction between N-Bromo succinimide (NBS) and 3-thiopheneethanol in ethyl acetate afforded M1 in 92% yield. M2 was obtained through Appel reaction of M1 in the presence of CBr4 and PPh3. Azidation of M2 with NaN3 yielded M3. CP-AZ was synthesized by a Pd-catalyzed Suzuki coupling reaction between M3 and 2,1,3-benzothiadiazole-4,7- bis (boronic acid pinacol ester).

CP-AZ were characterized using ^{1}H-NMR, FT-IR and GPC. The weight-average molecular weight (Mw) and number-average molecular weight (Mn) of CP-AZ measured by GPC were found to be 24100 and 22300 g/mol, respectively, with a PDI of 1.082.

Figure 3.4 shows the ^{1}H-NMR spectrum of CP-AZ. Triplet peaks at 3.11 ppm (a) and 3.68 ppm (b) are attributed to the methylene protons. The aromatic proton resonates from 7.6-8.5 ppm, and integration of the peak confirm there are three aromatic protons as expected.

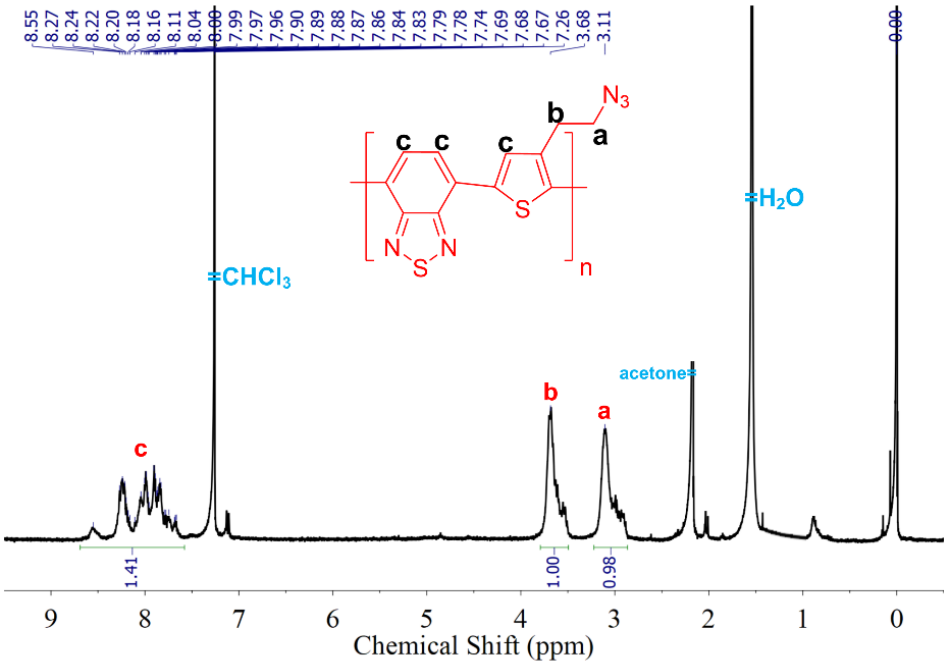

Figure 3.4: ^{1}H NMR ($CDCl_3$, 400 MHz, 25 °C) spectrum of CP-AZ.

From the FT-IR spectrum, the azide stretch peak can be seen at 2094 cm^{-1}. This confirms the successful azidation of the polymer.

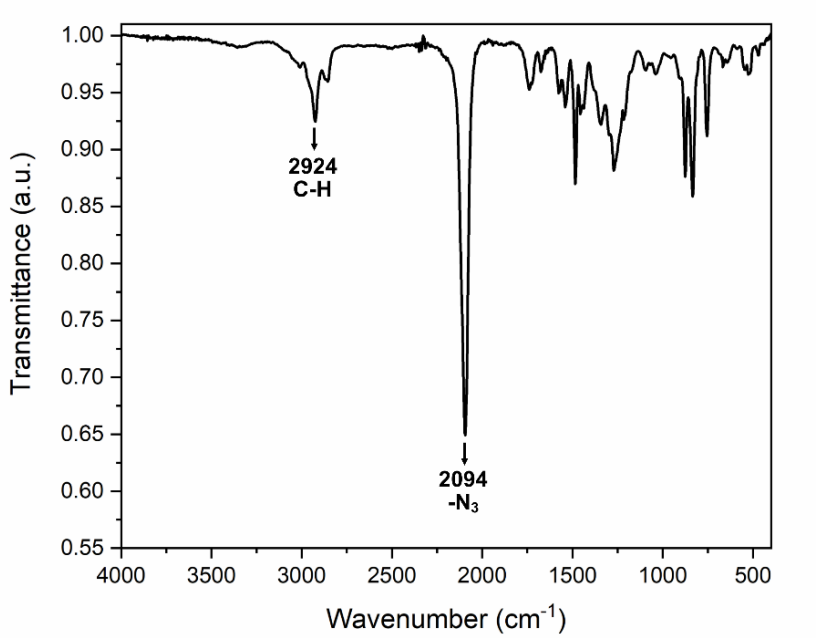

Figure 3.5: FT-IR spectrum of CP-AZ

The photophysical properties of CP-AZ were evaluated using UV-vis absorbance and fluorescence spectroscopy. CP-AZ has two maxima absorption bands at 319 and 494 nm with an emission band at 620 nm.

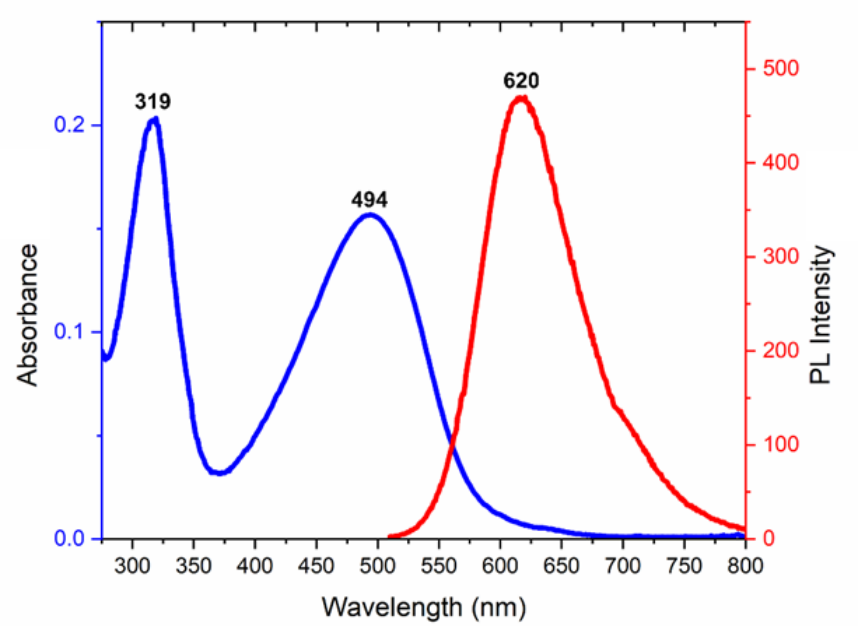

Figure 3.6: UV-vis absorbance and fluorescence spectra of CP-AZ in THF**.**

3.1.4 Preparation and Characterization CPPN

After fully characterizing CP-AZ, conjugated polymer-porphyrin nanoparticles (CPPN) were prepared using CB6-catalyzed azide-alkyne cycloaddition reaction (CB6-AAC) between CP-AZ and TPP-4AL as shown in Figure 3.7. Firstly, CB6 was dissolved in 1 N HCl, and then TPP-4AL was added to it and stirred for 15 min. CP-AZ in THF was injected into the aqueous solution will stirring with sonication for 1 h. After that, the mixture was left at room temperature overnight. The next day, the mixture was dialyzed using 14 kDa cut-off regenerated cellulose membrane 16 h to remove excess CB6 and unreacted monomers. The main driving force behind nanoparticles formation is the hydrophobic effect. When a polymer is dissolved in an organic solvent and added to water, the polymer chains fold into spherical shapes to avoid contact with water.

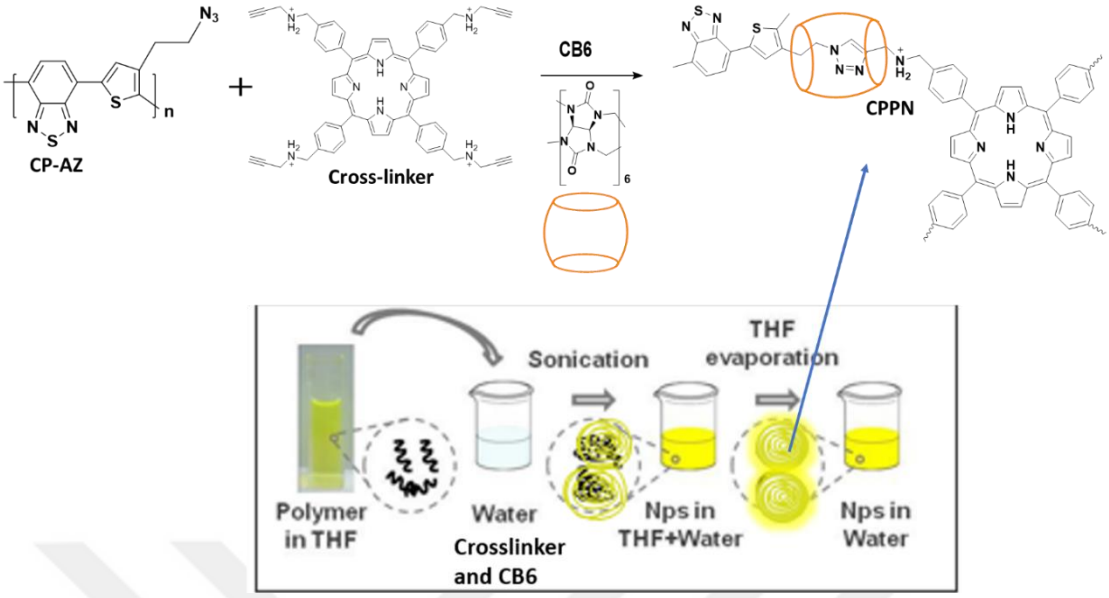

Figure 3.7: Preparation of CPPN by click reaction.

The success of the click reaction was confirmed using FT-IR. FT-IR spectrum of CP-AZ, TPP-4AL and CPPN is shown in Figure 3.8. The decrease in the azide stretch intensity at 2095 cm^{-1}, the appearance of carbonyl peak at 1730 cm^{-1} and also the disappearance of the alkyne peak at 2130 cm^{-1} confirms the success of the click reaction.

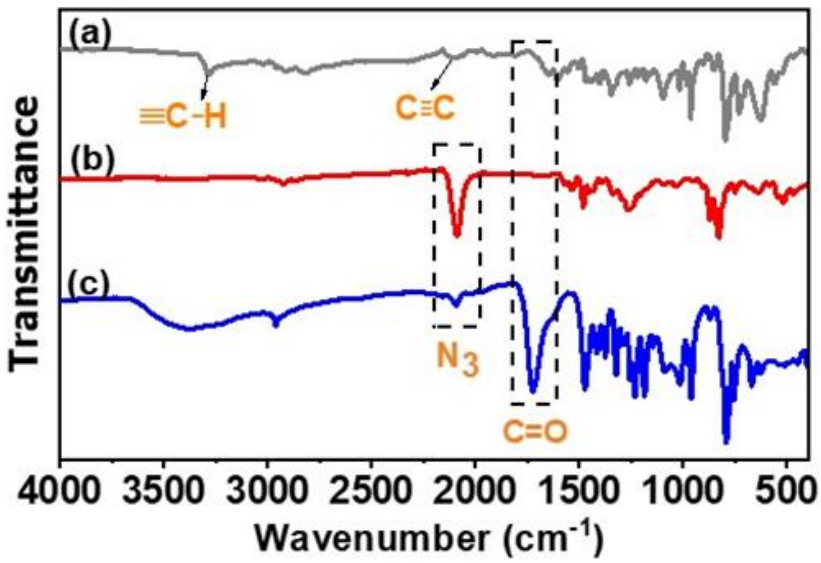

Figure 3.8: Comparison of FT-IR spectra of (c) **CPPN** with (a) **TPP-4AL** and (b) **CP-AZ**.

Furthermore, the morphology of CPPN was examined using TEM and SEM. TEM and SEM images of CPPN shows that CPPN is spherical in shape (Figure 3.9). SEM/EDX analysis shows that CPPN contains 51.46% C, 25.00% O, 23.32% N and 0.22% S. In addition, XPS was used to analyzed the elemental and chemical composition of CPPN. The seven C1s XPS peaks were assigned to C=C (284.25 eV), C-C (284.70 eV), C-S (285.10 eV), C-N (285.41 eV), C-O (286.35 eV), C=O (287.62 eV) and N-C=O (289.10 eV). For N1s, the three peaks were attributed to C=N-C of pyrrolic-N and C=N-S of CP-AZ at 399.26 eV, amine-N and N-N=C of triazole-N and at 400.15 eV and N(C)3 at 401.52 eV. The O 1s XPS spectrum displayed one major peak at 532.25 eV, and this represents the C=O bond. Finally, the S2p core level XPS spectrum was fitted to four components with binding energies of 165.5 eV (S2p3/2), and 166.7 eV (S2p1/2) attributed to the N-S-N bond, and those at 163.9 eV (S2p3/2) and 165.1 eV (S2p1/2) were attributed to C-S-C bond (Figure 3.10).

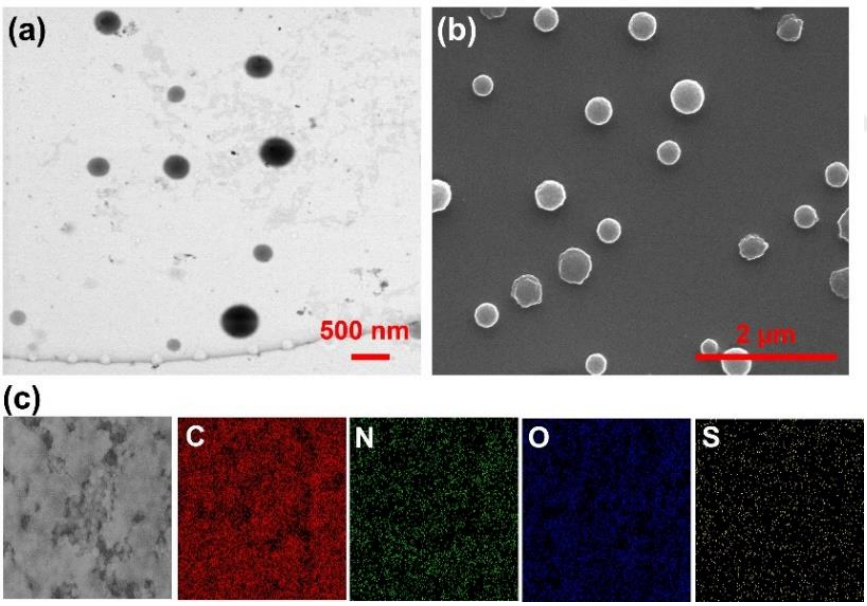

Figure 3.9: (a) TEM, (b) SEM and (c) SEM/EDX elemental mapping images of **CPPN**.

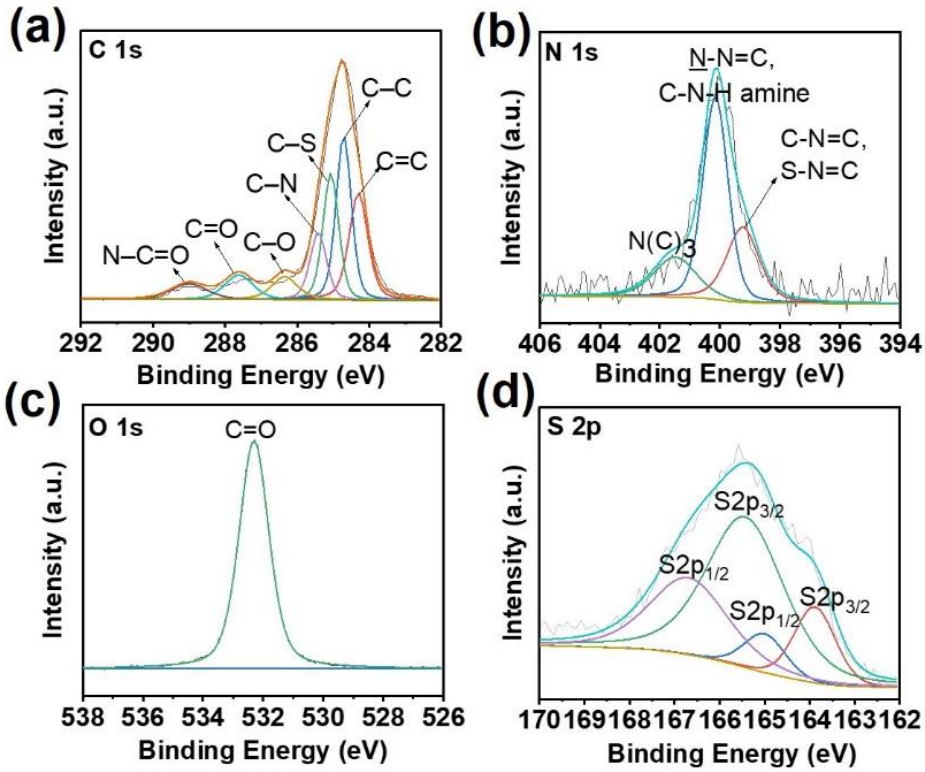

Figure 3.10: High resolution XPS data of CPPN: (a) C1S, (b) N1s, (c) O1s and (d) S2p.

Absorption at 330 nm and 415 nm were assigned to CP-AZ and TPP-4AL (Soret-band), respectively. Q-bands of TPP-4AL overlapped with the broad absorption peak of CP-AZ at 494 nm, as depicted in Figure 3.11. Two emission peaks were seen at 650 nm and 705 nm for CPPN.

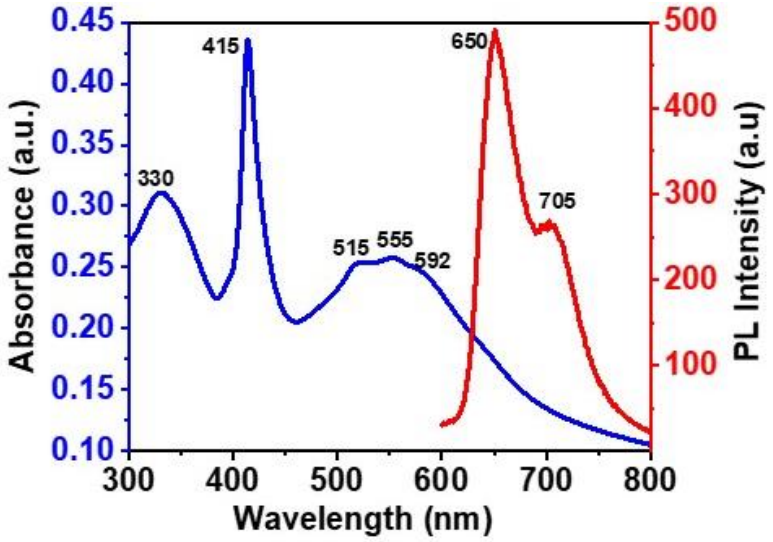

Figure 3.11: UV-vis and fluorescence spectra of CPPN.

According to DLS, the conjugated polymer-porphyrin nanoparticles **(**CPPN) displayed a number average hydrodynamic size of about 185 nm. The zeta potential of the nanoparticles in water was +39.5 mV at 25 ^{0}C (Figure 3.12). The positive ζ-potential is due to the positive charges on the nanoparticles. ζ-potential of +39.5 mV shows that CPPN are stable in water. In addition, the stability of CPPN in water was further monitored by measuring the size of the nanoparticles for 36 days (200 µg/mL, RT). From Figure 3.13, it can be seen that the size of CPPN remained almost unchanged for more than a month. The introduction of positive charges into the nanoparticles causes repulsion between them and prevents aggregation.

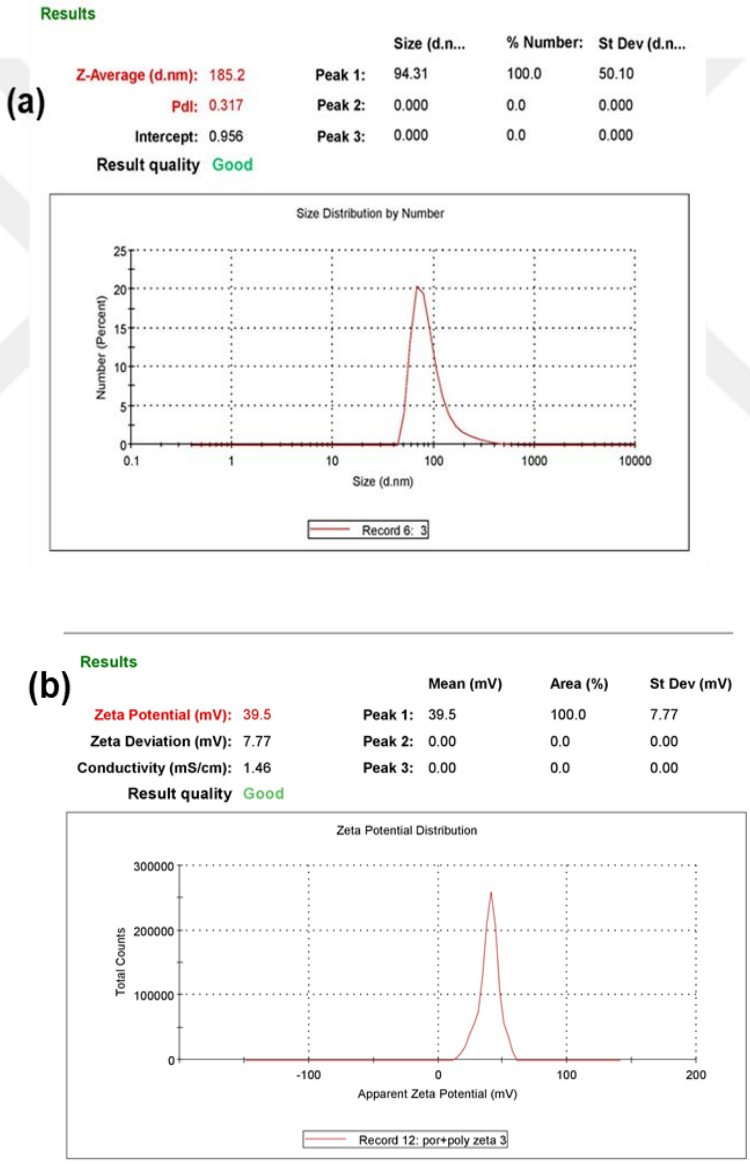

Figure 3.12: DLS histograms of CPPN: (a) number average hydrodynamic size and (b) zeta potential.

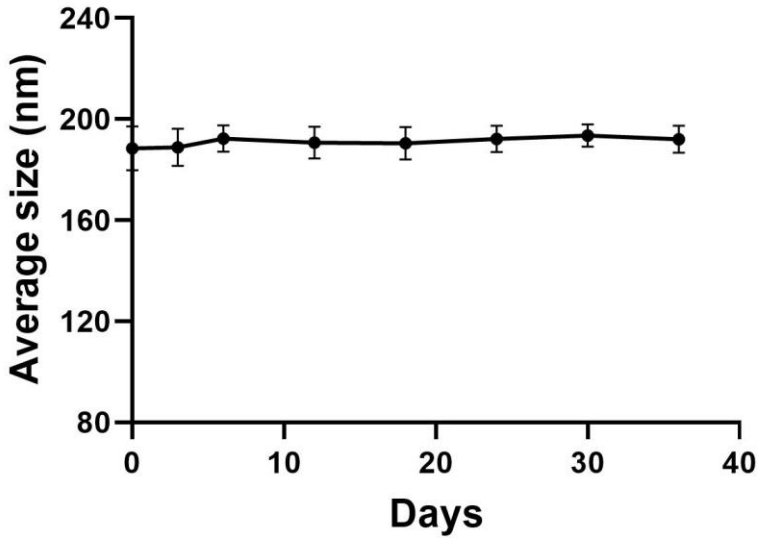

Figure 3.13: Stability test of CPPN in deionized (DI) water for 36 days. Results represent the mean ± SD of four separate measurements.

Section 3.2 Application of CPPN in Photodynamic Antibacterial and Anticancer Therapies.

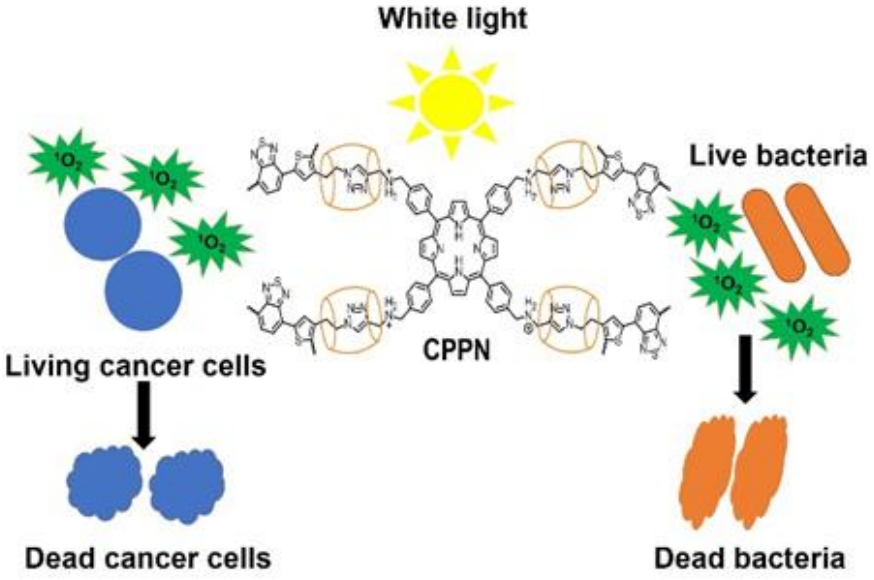

Figure 3.14: Mechanism of antibacterial and anticancer activity of CPPN.

3.2.1 ROS Generation Ability of CPPN

Light-induced reactive oxygen species (ROS) generation ability of CPPN was examined using well known 2,7-dichlorofluorescein diacetate (DCFH-DA) assay. Figure 3.15a provides information about the ROS detection mechanism of the DCFH-DA assay. Firstly, DCFH-DA is hydrolysed to a non-fluorescent 2,7-dichlorofluorescein (DCFH) using an aqueous solution of NaOH. In the presence of ROS, non-fluorescent DCFH can be rapidly oxidised to highly fluorescent 2,7-dichlorofluorescein (DCF), resulting in a clear rise in fluorescence intensity at 524 nm.

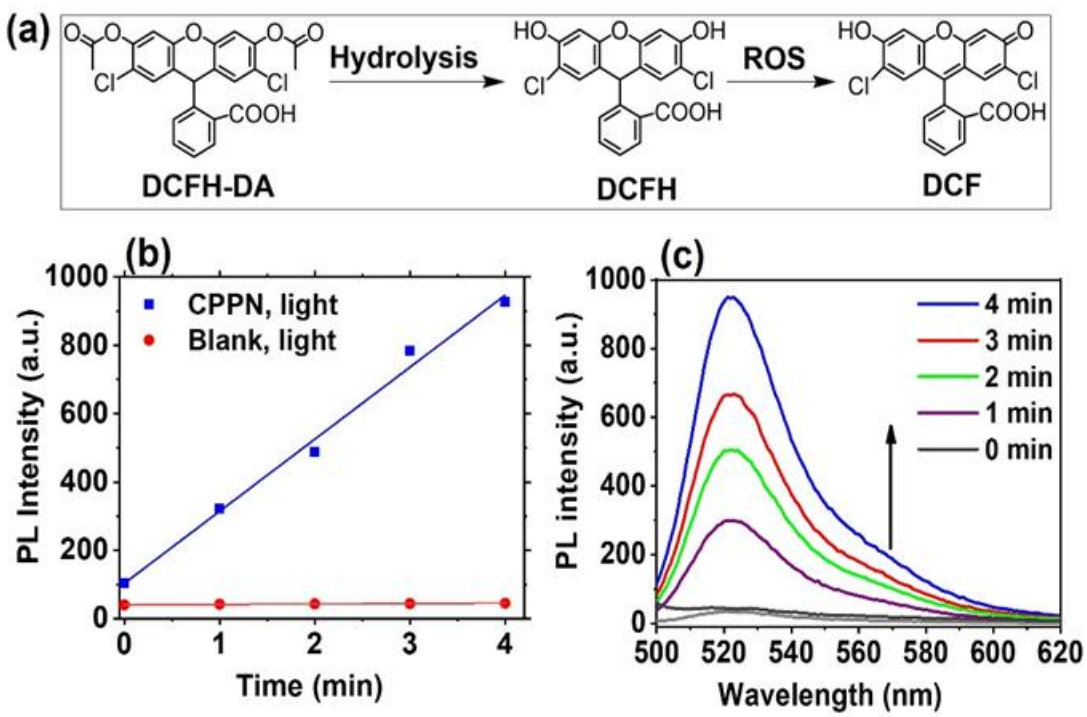

Figure 3.15: (a) Mechanism of ROS detection through DCFH-DA assay. (b) Time response curves of DCFH oxidation with and without CPPN under white light irradiation (1 mW cm^{-2}), (c) The corresponding fluorescence spectra of DCF at 524 nm in the presence of CPPN, under white light.

Figure 3.15b shows the time response curve of DCFH oxidation with and without CPPN light illumination (1 mW/cm^2) for four minutes. From Figure 3.15c, DCFH displayed weak emission peaks at 524 nm when exposed to light without CPPN, and this is due to autooxidation of DCFH to DCF. When CPPN was added to the solution of DCFH, no significant rise in fluorescent was seen compared to the blank group. However, when CPPN

was added to DCFH and exposed to white light (1 mW/cm^2), a massive increase in fluorescence emission intensity was seen at 524 nm and continued to rise throughout the four minutes. The fluorescence emission intensity rose to about 300 nm within a minute and continued to rise, reaching approximately 1000 nm when illuminated for four minutes. These results show that **CPPN** can generate ROS significantly even at a low dose of white light (1 mW/cm^2).

3.2.2 Broad Spectrum Photodynamic Antibacterial Activity of CPPN

After confirming that the conjugated polymer-porphyrin nanoparticles **(**CPPN) can generate ROS, its light-triggered biocidal activity against *E. coli* (Gram-negative), *B. Subtilis* (Gram-positive) and *S. aureus* (Gram-positive), the optimum concentration (MIC) of CPPN to inactivate the bacteria was determined using the broth dilution method. The minimum inhibitory concentration (MIC) was measured in the dark and under light irradiation. To a 100 µL of *E. coli* suspension, 10 µL of CPPN of different concentrations (5-30 µg mL^{-1}) was added both in the dark and under white light irradiation for 10 minutes with a flux of 22 mW cm^{-2}. After keeping the CPPN-treated *E. coli* and non-treated control group in the dark and under light illumination, the optical density at 600 nm (OD_{600}) was measured using a microplate reader. Figures 3.16a and 3.16b show the MIC graph of CPPN in the dark and under light irradiation, respectively. From the graph, when *E. coli* was treated with CPPN in the dark, no significant change in absorbance was seen as expected because CPPN is a photosensitizer that is activated with light. However, when treated with CPPN and exposed to light, a significant decrease in absorbance was seen as the concentration of CPPN increase compared to the control groups. For the light groups, the absorbance reached a plateau after 20 µg mL^{-1} and hence the MIC value of CPPN was estimated to be 20 µg mL^{-1}.

After estimating the MIC to be 20 µg mL^{-1}, the photodynamic antibacterial activity of CPPN against the three model bacteria were investigated in the dark and under light irradiation (10 min, 22 mW cm^{-2}) using the surface plating method and the data obtained at shown in Figure 17a-f. From colony counting results, about 3.8, 3.6 and 3.5-log reduction colony-forming units (CFUs) was achieved when *E. coli*, *B. subtilis* and *S. aureus* were treated with CPPN (20 µg mL^{-1}) under light exposure for 10 min. But in the dark, CPPN displayed negligible dark toxicity towards the three model bacteria.

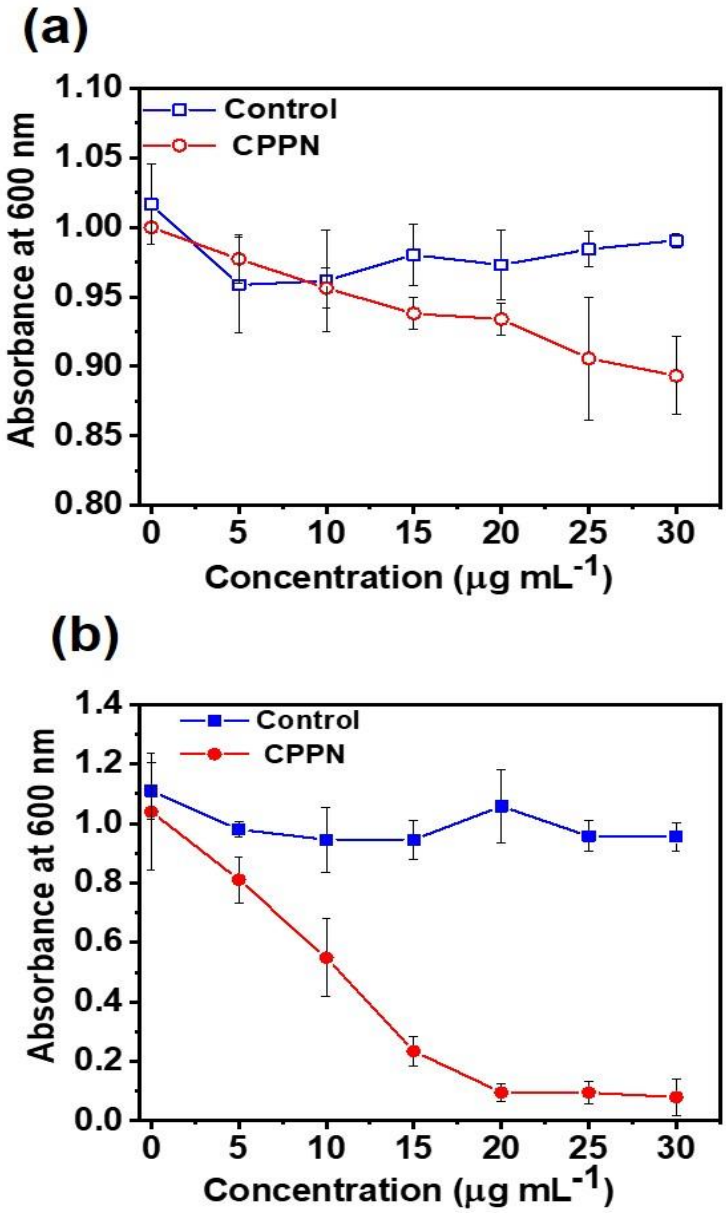

Figure 3.16: Minimum Inhibitory Concentration (MIC) assay for varying concentration of CPPN (a) in the dark and (b) under light in comparison with control group without CPPN. Results are expressed as mean ± SD of three separate experiment.

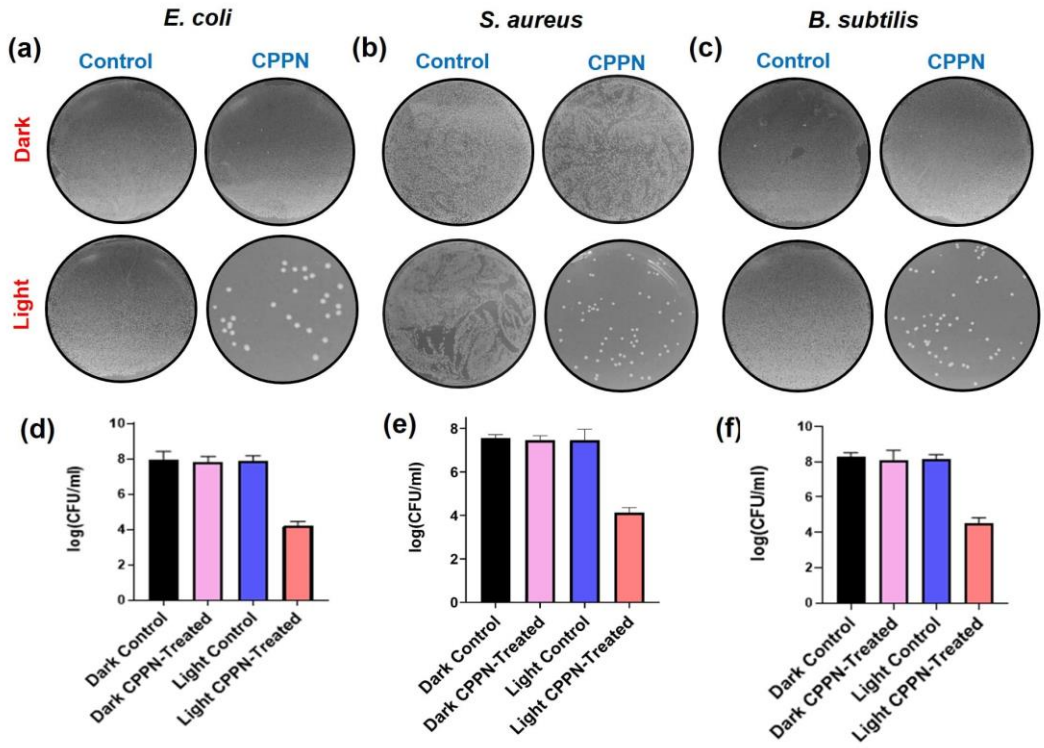

Figure 3.17: Plate photographs of bacteria: (a) *E. coli*, (b) *S. aureus*, and (c) *B. subtilis* for control and CPPN treated groups in the dark and under white light irradiation (22 mW cm^{-2}) for 10 min. The corresponding antibacterial activity of CPPN toward (d) *E. coli*, (e) *S. aureus*, and (f) *B. subtilis*. Results represent the mean ± SD of three separate experiments.

In addition, the agar disk diffusion method was used to investigate further the photodynamic antibacterial activity of CPPN in the dark and under light illumination for 10 min. Figure 3.18a-f shows the comparison of the plate photographs of agar disk diffusion assay and the corresponding inhibition zone radius graphs of CPPN and ampicillin towards E. coli, B. subtilis and S. aureus bacteria, in the dark and under light illumination. From the agar disk diffusion method results, as expected, both in the dark and under light conditions, the inhibition zone radius for ampicillin towards the three studied bacteria was more the 6.5 mm. For CPPN, in the dark, the inhibition zone radius was negligible; however, when exposed to white light (10 min, 22 mW cm^{-2}), the inhibition zone radius increases significantly (more than 6 mm) for the model bacteria. This result supports our previous findings that CPPN is an ideal photosensitizer with negligible dark cytotoxicity.

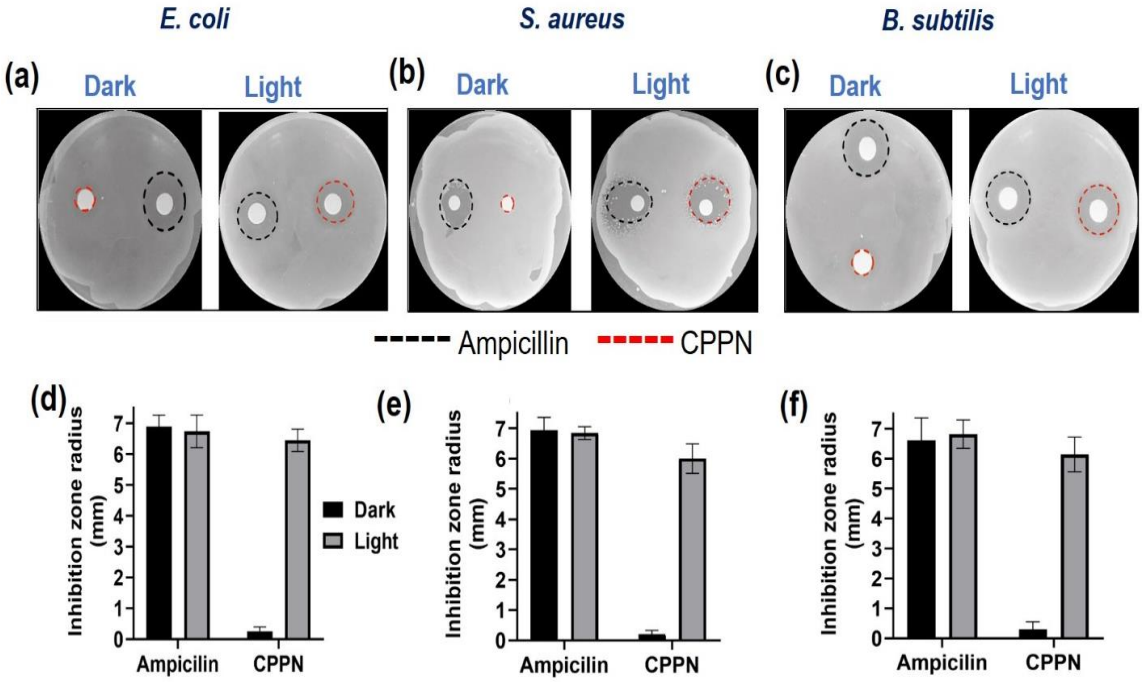

Figure 3.18: Plate photographs of agar disk diffusion assay of (a) *E. coli*, (b) *S. aureus* and (c) *B. subtilis*, treated with 20 μg mL^{-1} of CPPN and ampicillin in the dark and under white light irradiation (22 mW cm^{-2}) for 10 min. The corresponding inhibition zone radius graphs of (d) *E. coli*, (e) *S. aureus* and (f) *B. subtilis*. The zone of inhibition is the average of the radii measured from at least 6 different spots on the circle. Results represent the mean ± SD of three separate experiments.

3.2.3 Investigating CPPN-Bacteria Interaction Using SEM and ζ-potential

To investigate the interaction mechanism between CPPN and the bacteria, a scanning electron microscope (SEM) was used to observe the changes in the morphology of bacteria. As shown in Figure 3.19, when E. coli, B. subtilis and S. aureus were treated with CPPN in the dark without light, the bacteria retained their structure and smooth surfaces without any significant damage. However, after treatment with 20 μg mL^{-1} of CPPN and irradiation with white light for 10 min (22 mW cm^{-2}), the morphology of the three studied bacteria completely changed with a raptured cell membrane. Also, the cytoplasmic contents of the bacteria leaked out, and this is due to the reactive oxygen species (ROS) generated when CPPN is illuminated with light. ROS attacks the cell membrane of the bacteria, which leads to the disruption of the cell's activities. For light control groups, the morphology of the three bacteria remained unchanged. This means the change in morphology is not caused by light but by ROS, which is generated when CPPN is irradiated with white light.

To further study the mechanism of photodynamic antibacterial activity of CPPN, ζ-potential measurements were used to investigate the interaction between CPPN and the negatively charged bacteria (Figure 3.19d). The three model bacteria were treated with 20 μg/mL of CPPN in the dark and under white light illumination (22 mW cm^{-2}) for 10 min, then their ζ-potential values were measured. Control groups of E. coli, B. subtilis and S. aureus only had ζ-potentials of -47.6, -36 and -30.6 mV, respectively, and when treated with CPPN in the dark, positive shifted values were seen for all the model bacteria. When bacteria were treated with CPPN and exposed to white light (22 mW cm^{-2}) for 10 min, much more positive shifts were experienced for the three model bacteria.

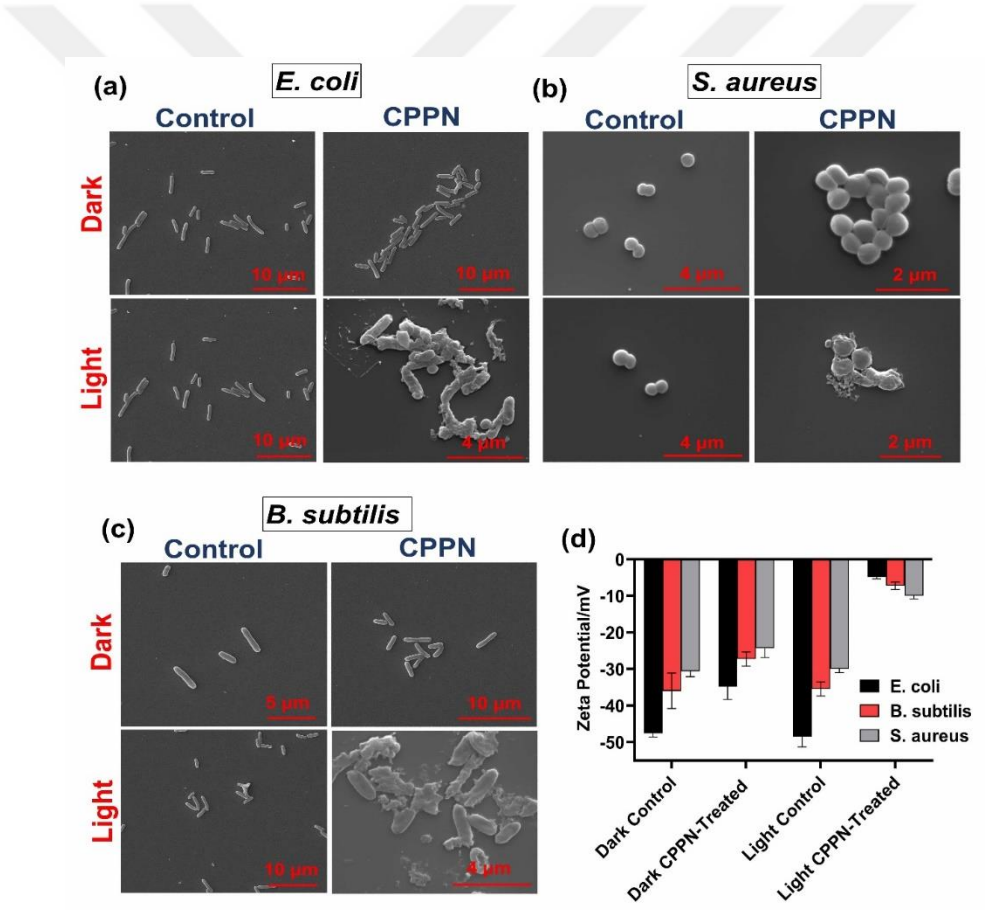

Figure 3.19: SEM images of (a) *E. coli*, (b) *S. aureus* and (c) *B. subtilis* treated with CPPN and ampicillin in the dark and under white light irradiation (22 mW cm^{-2}) for 10 min, (d) ζ-potentials of the bacteria for control and CPPN treated samples in the dark and under white light irradiation for 10 min.

3.2.4 Mammalian Cancer Cell Cytotoxicity and Photocytotoxicity of CPPN

The in vitro cytotoxicity of CPPN against mammalian cancer cell line was investigated MTT assay. MCF-7 breast cancer cells were treated with different concentrations of CPPN from 3.75-112.5 µg/mL. The CPPN treated MCF-7 breast cancer cells were compared to the DMEM-control group (Figure 3.20). The difference in cell viability between DMEM-control cells and CPPN treated cells in the dark was insignificant. Even at a high CPPN concentration of 112.5 µg/mL, the cell viability was around 96%. On the other hand, cells that were treated with CPPN and irradiated to white light (20 mW cm^{-2}) for 20 min displayed a drastic decrease in cell viability. CPPN show dose-dependent cytotoxicity against the MCF-7 breast cancer cells. At a concentration of 18.75 µg/mL, approximately 55% of the cells were viable. Moreover, the half-maximal inhibitory concentration value (IC_{50}) of cells treated with CPPN with white light exposure was determined to be around 20.8 µg mL^{-1}. These results explicitly demonstrated that, even at low CPPN concentrations, white light activates CPPN effectively, resulting in a significant decrease in cell viability of the MCF-7 breast cancer cells. CPPN is a good photosensitizer, with minimal dark cytotoxicity but highly toxic upon short time illumination with white light at low intensity (22 mW/cm^2). These findings are in support of the results from the photodynamic antibacterial assays confirming that CPPN is an ideal photosensitizer with negligible dark cytotoxicity.

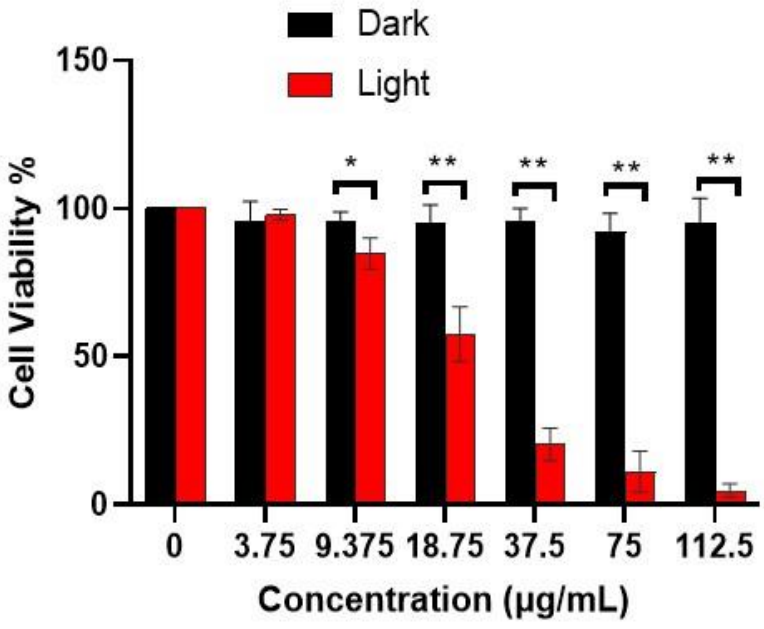

Figure 3.20: Relative cell viability (%) of CPPN against MCF-7 breast cancer cells at different concentrations in the dark and under light illumination (22 mW cm^{-2}, 20 minutes). 2-way ANOVA multiple comparison test was performed to compare results for the significant differences between groups. The data are represented as the mean ± Std. (n = 4) (* and ** indicate a significant difference between groups with $p < 0.05$ and $p < 0.0001$, respectively).

SECTION 3.3 Synthesis and Application of PCP

3.3.1 Synthesis of PCP

Cross-linked conjugated polymer nanoparticles (PCP) were synthesized by following the same procedure used to synthesize CPPN.

The success of the azide-alkyne click reaction was confirmed by FT-IR spectroscopy (Figure 3.21). The obtained nanoparticles (PCP) were stable in aqueous media without aggregation. The number average hydrodynamic size of PCP was 122 nm according to DLS analysis with ζ-potential +36.5 mV (Figure 3.22).

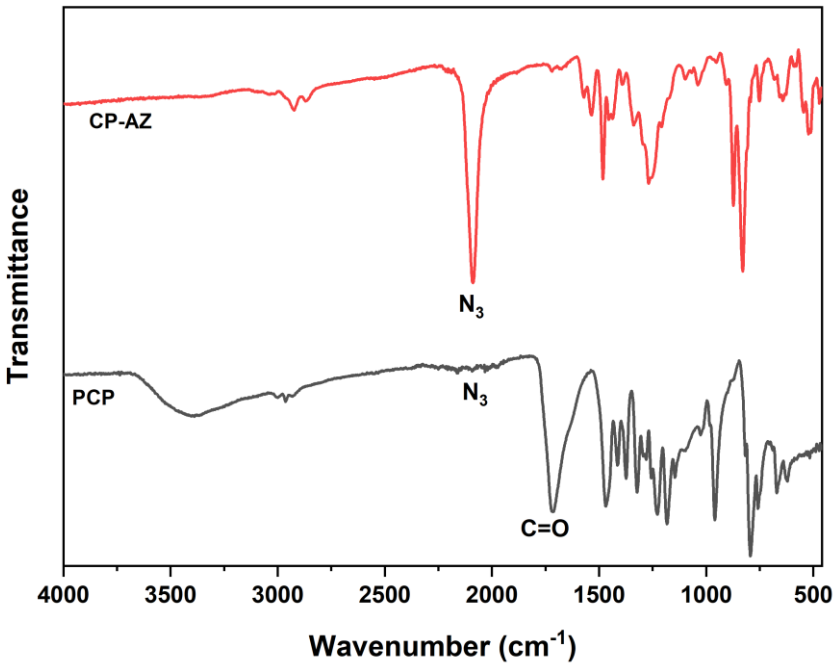

Figure 3.21: Comparison of FT-IR spectra of PCP with CP-AZ.

(a)

Results

		Size (d.n...	% Number:	St Dev (d.n...
Z-Average (d.nm): 122.2	Peak 1:	50.11	100.0	21.95
PdI: 0.315	Peak 2:	0.000	0.0	0.000
Intercept: 0.215	Peak 3:	0.000	0.0	0.000

Result quality Good

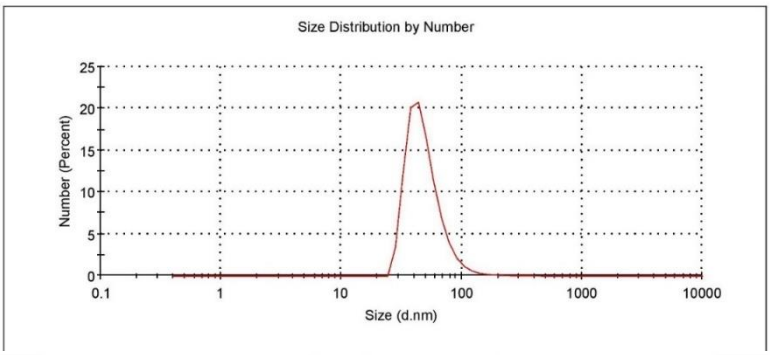

(b)

Results

		Mean (mV)	Area (%)	St Dev (mV)
Zeta Potential (mV): 36.5	Peak 1:	36.5	100.0	8.19
Zeta Deviation (mV): 8.19	Peak 2:	0.00	0.0	0.00
Conductivity (mS/cm): 1.36	Peak 3:	0.00	0.0	0.00

Result quality Good

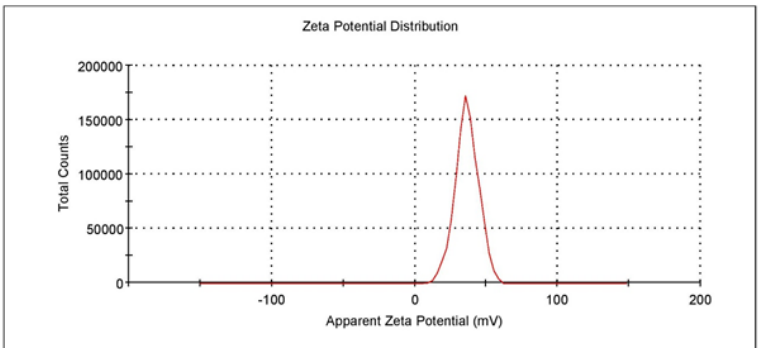

Figure 3.22: DLS histograms of PCP: (a) number average hydrodynamic size and (b) zeta potential.

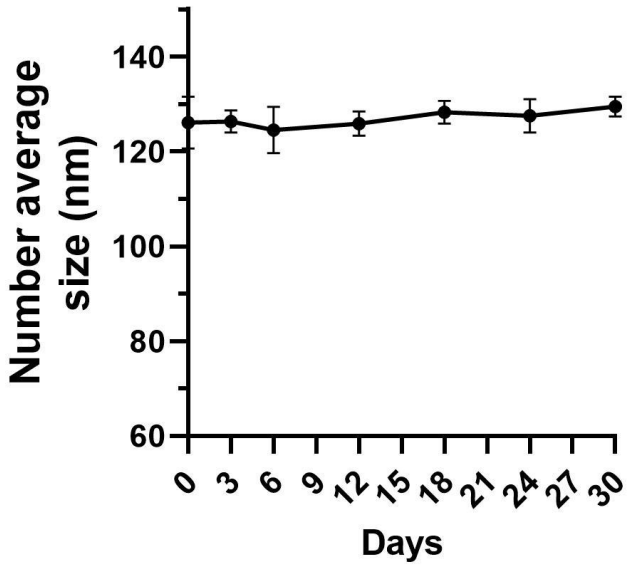

Figure 3.23: Stability test of PCP in deionized (DI) water for 30 days. Results represent the mean ± SD of three separate measurements.

The photophysical properties of PCP were examined using UV and fluorescence spectroscopy. PCP showed absorption peaks at 320 nm and 530 nm, while the emission peak was at 680 nm for PCP (Figure 3.24).

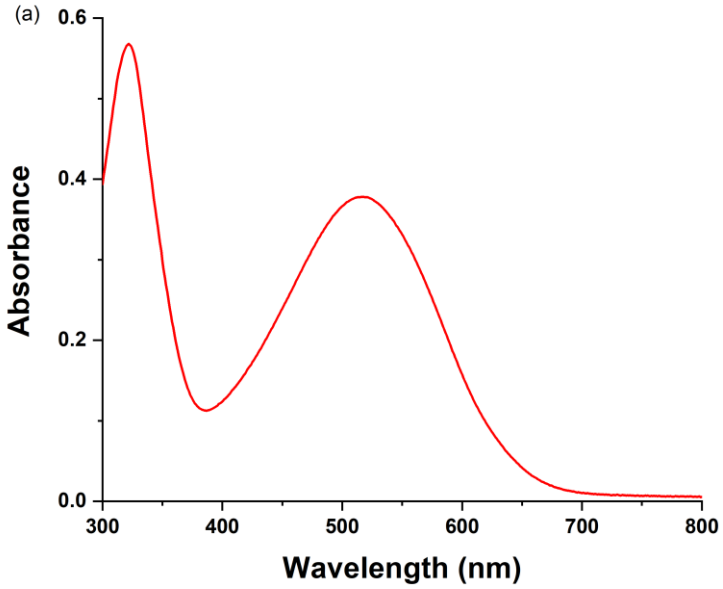

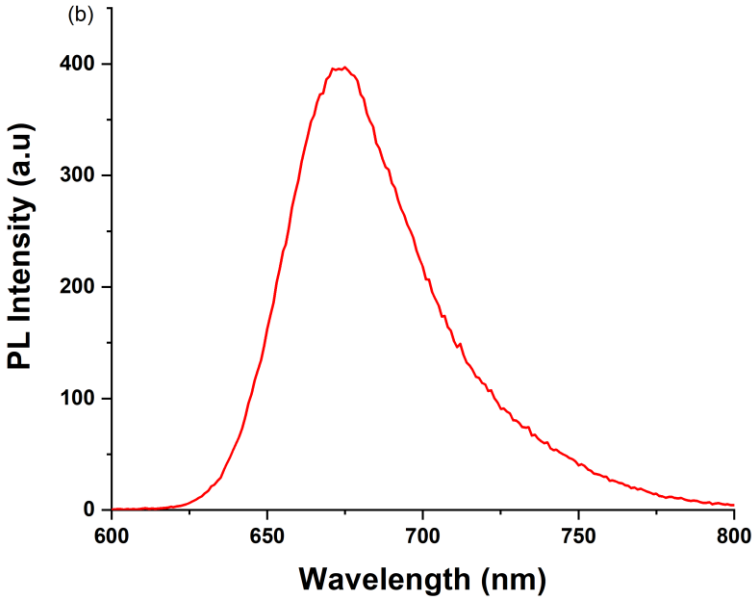

Figure 3.24: (a) UV-vis and (b) Fluorescence spectra of **PCP**

3.3.2 Photodynamic Effects of PCP on Bacteria

First, the MIC on PCP on *E. coli* was measured by following the same procedure used for CPPN. The MIC was determined to be 24 µg mL^{-1} when *E. coli* is treated with PCP and illuminated with white light (20 mW cm^{-2}) for 10 min (Figure 3.25 a-b). E. coli and B. subtilis were treated with PCP (24 µg mL^{-1}) in the dark and under light irradiation for 10 min. According to colony counting results (Figure 3.26), about 3-log reduction colony-forming units (CFUs) was achieved when *E. coli* and *B. subtilis* were treated with PCP under white light illumination for 10 min. However, PCP displayed almost no toxicity in the dark against the model bacteria.

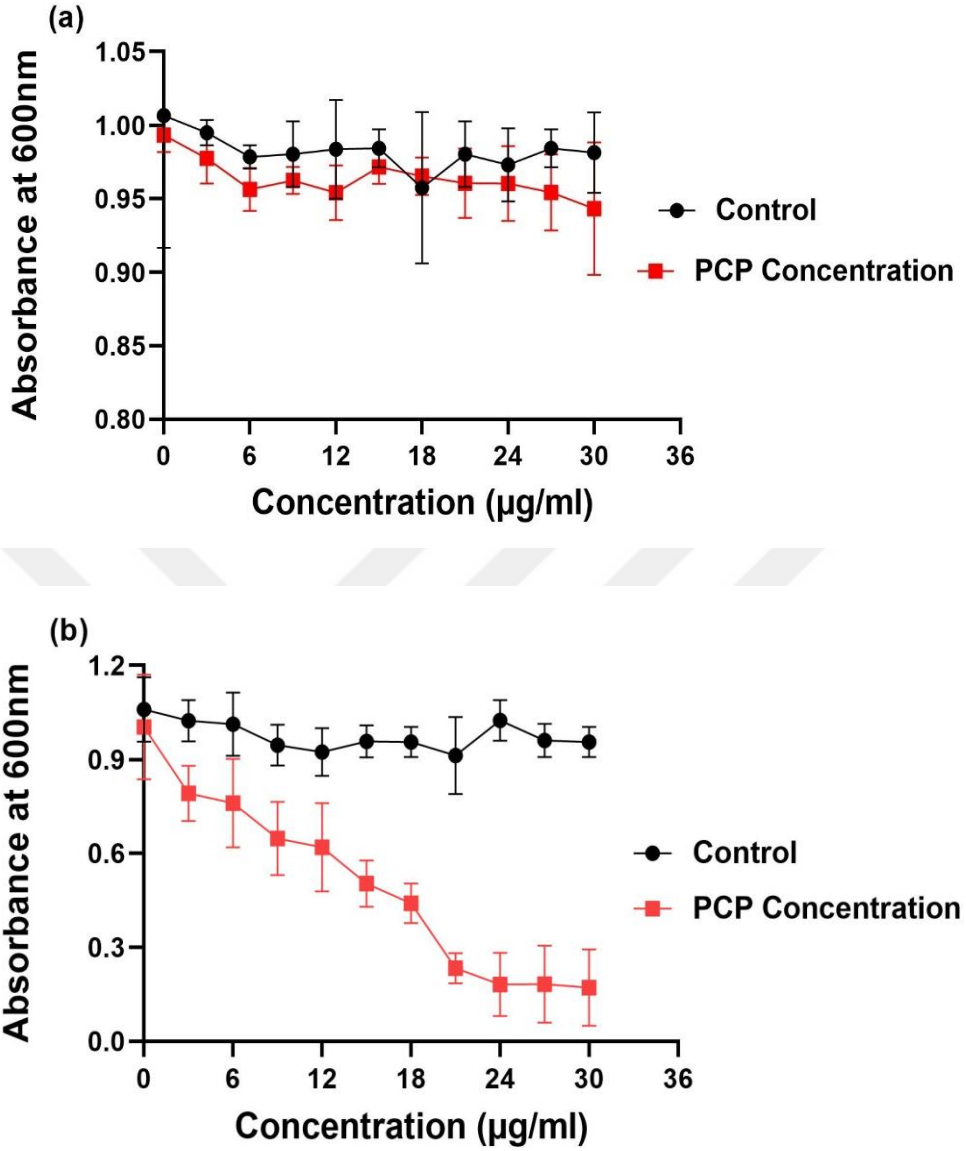

Figure 3.25: MIC assay of PCP (a) in the dark and (b) under light in comparison with control group without PCP. Results represent mean ± SD of three separate experiment.

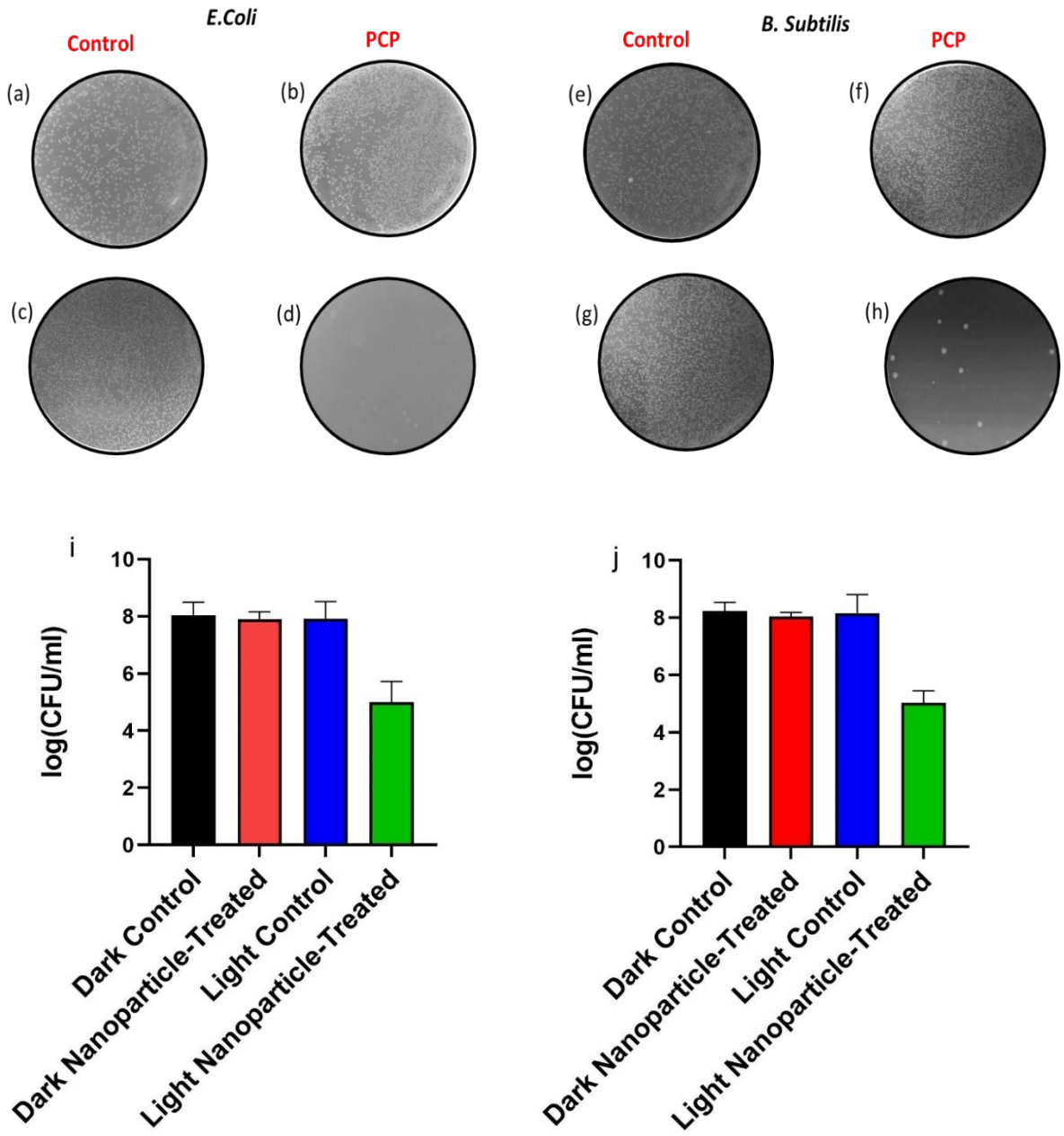

Figure 3.26. Plate photographs of bacteria on the agar plate: *E. coli* (a) control, (b) with PCP in the dark, (c) light control, (d) with PCP under light illumination; and *B. subtilis* (e) Control, (f) with PCP in the dark, (g) light control, (h) with PCP under light illumination. Antibacterial activity of the PCP toward E. *coli* (i) and *B. subtilis* (j) in the dark and under light illumination. Light treatment: white light with a flux of 22 mW cm^{-2} for 10 min. The data represented the mean ± standard deviation of three separate experiments.

To further investigate the light-induced antibacterial photodynamic effect of cross-linked conjugated polymer nanoparticles (PCP) on bacteria, a disk diffusion assay was utilized. Ampicillin inactivated bacteria both in the dark and under light illumination as expected. When bacteria were treated with PCP in the dark, almost no inhibition zone radius was seen, but when they were treated with PCP and illuminated with light, inhibition zone radius increased (Figure 3.27).

The antibacterial photodynamic therapy (PDT) efficiency of PCP was less than that of CPPN due to the presence of porphyrin in CPPN. Porphyrin acts as a photosensitizer, and it generates reactive oxygen species (ROS) when exposed to light, thereby increasing the PDT efficiency of CPPN.

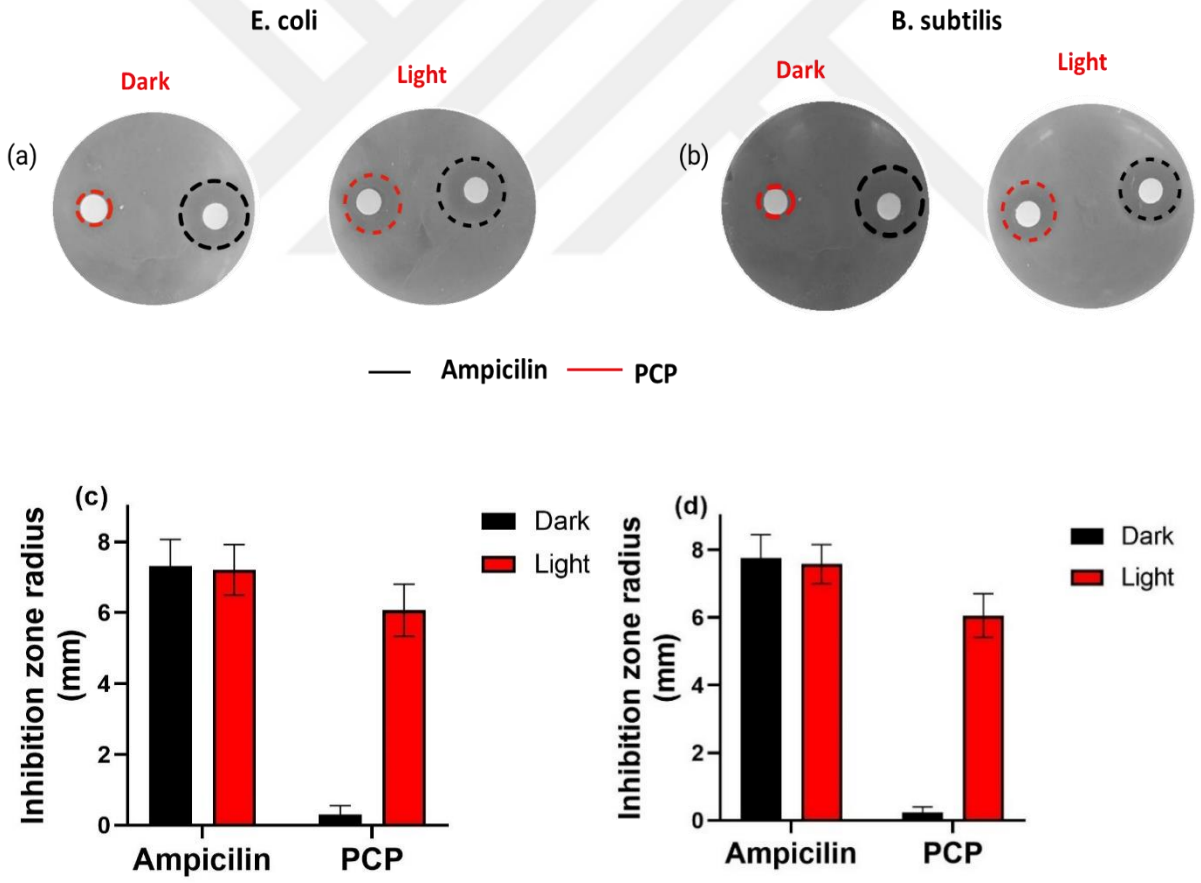

Figure 3.27: Plate photographs of agar disk diffusion assays of (a) *E. coli* and (b) *B. subtilis*, which were treated with 24 μg/mL **PCP**. The corresponding inhibition zone radius graphs of (c) *E. coli* and (d) *B. subtilis*. Experiments were repeated three times, and results were plotted as the mean of three independent experiments.

Section 3.4 Cross-linked Conjugated Polymer-Gold Nanoparticles

3.4.1 Synthesis and Characterization of CPPN-Au and PCP-Au Nanoparticles

Conjugated polymer-porphyrin-gold nanoparticles (CPPN-Au) and cross-linked conjugated polymer-gold nanoparticles (PCP-Au) nanoparticles were synthesized by following the same procedure used to synthesized CPPN and PCP. However, in the aqueous media, AuCl3 was added, and after that, the same procedure for the synthesis of CPPN and PCP was followed. The main driving force behind nanoparticles formation is the hydrophobic effect. The hydrophobic conjugated backbone of the polymer and porphyrin interact with Au^{3+} ion through π-ion interaction and fold around the Au^{3+} ion, thereby encapsulating the gold.

The morphology of the nanoparticles was characterized using SEM. SEM images showed that the nanoparticles were spherical with gold encapsulated in them (Figure 3.28).

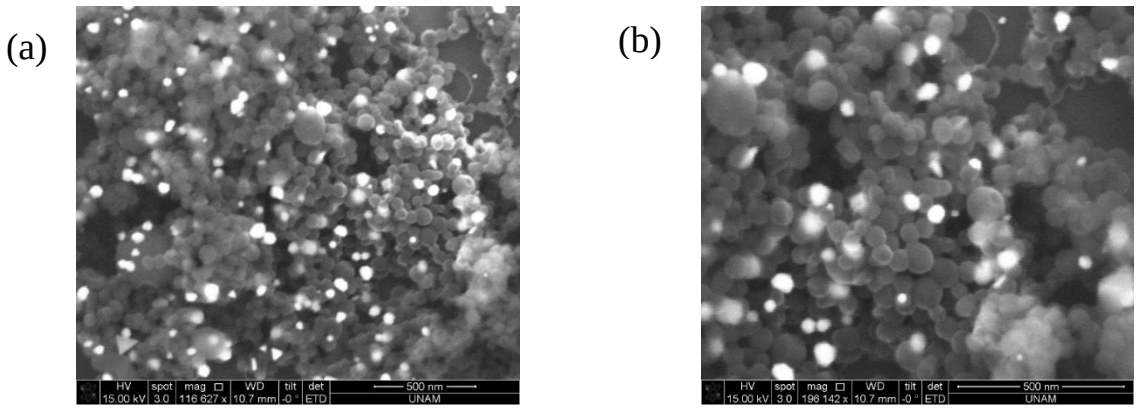

Figure 3.28: SEM images of (a) CPPN-Au and (b) PCP-Au.

Also, CPPN-Au and PCP-Au showed photophysical properties similar to CPPN and PCP (Figures 3.29 and 3.30). A bathochromic shift was seen in the Uv and fluorescence spectra of CPPN-Au and PCP-Au compared to CPPN and PCP.

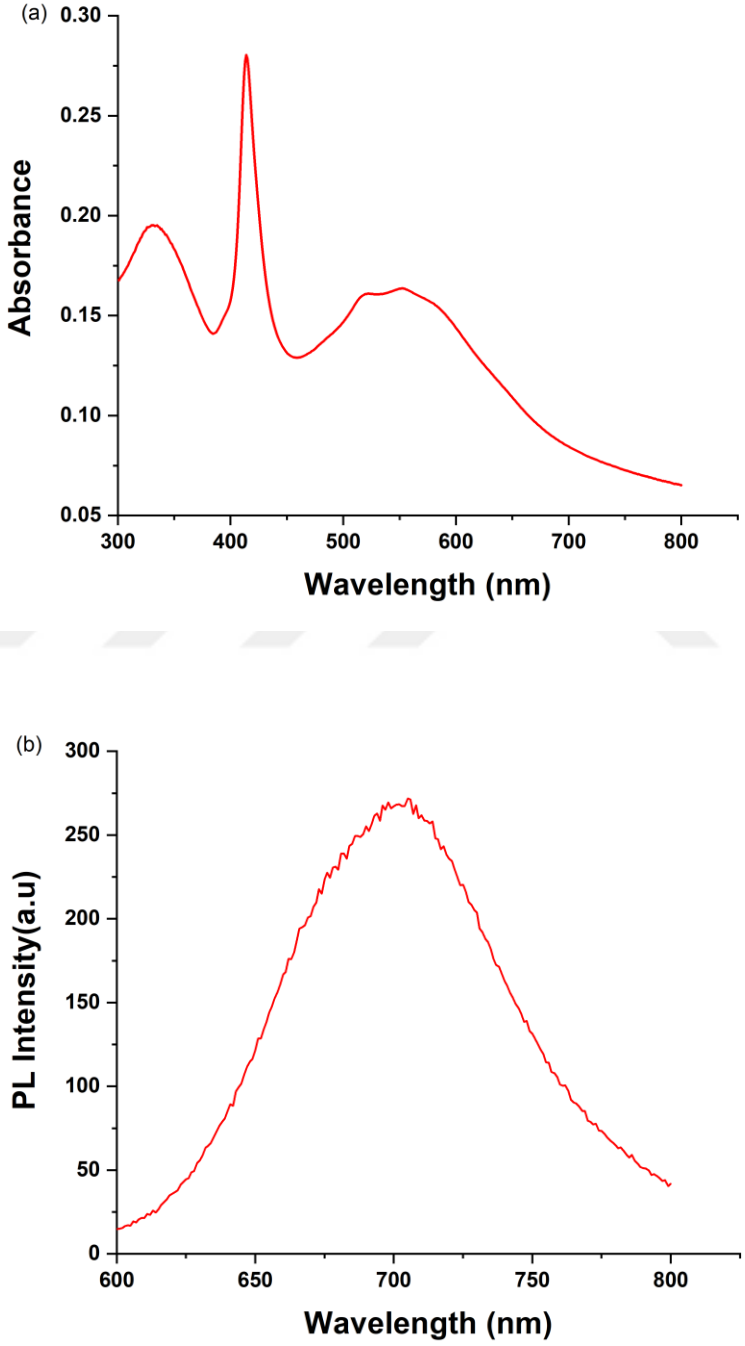

Figure 3.29: (a) UV-vis and (b) Fluorescence spectra of CPPN-Au nanoparticles.

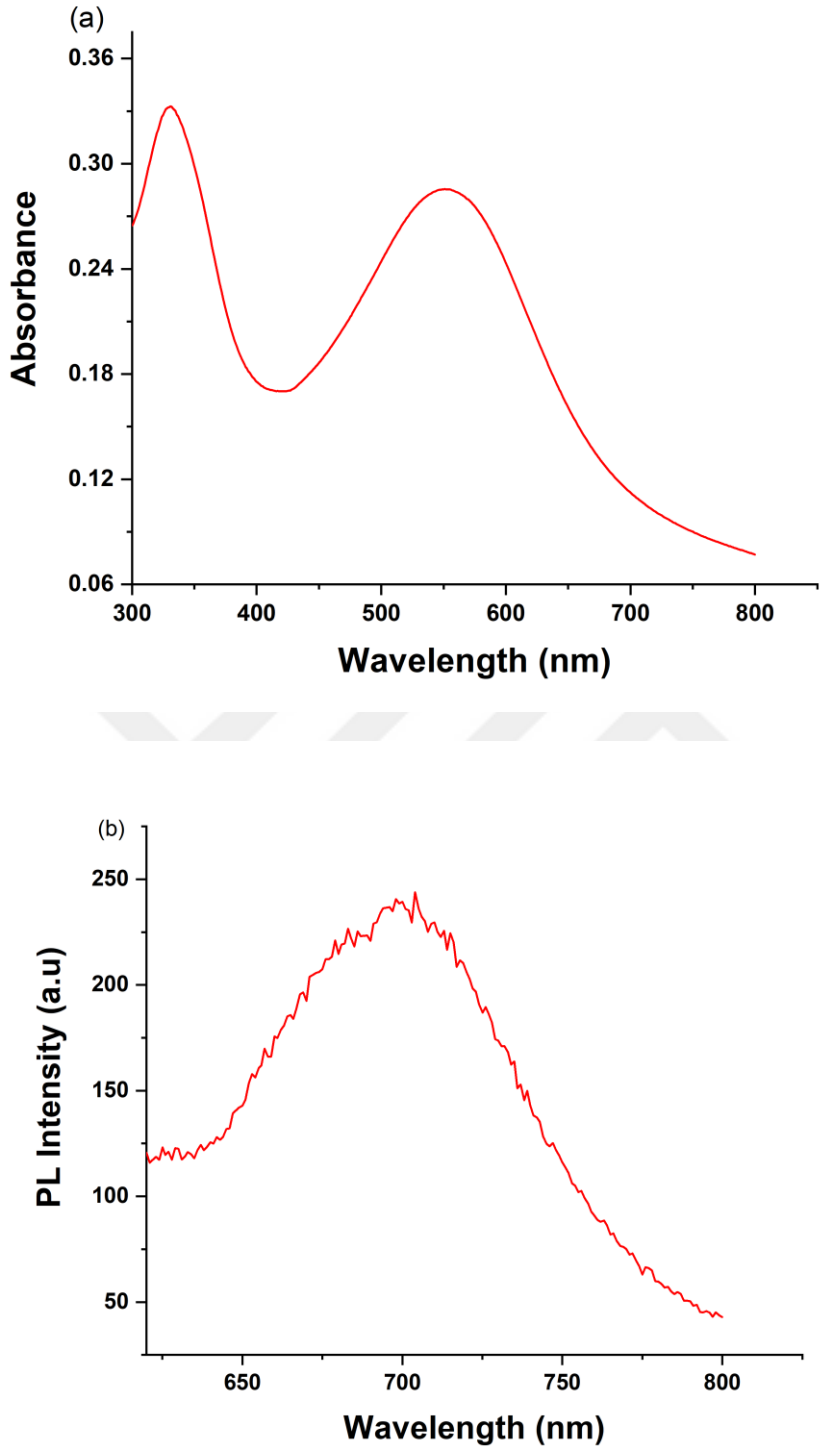

Figures 3.30: (a) UV-vis and (b) Fluorescence spectra of PCP-Au nanoparticles.

The nanoparticles were not stable in water, so they precipitated after two days. Figures 3.31 and 3.32 shows the stability of CPPN-Au and PCP-Au nanoparticles in water. Due to the instability of CPPN-Au and PCP-Au nanoparticles, we could not use them in phototherapy.

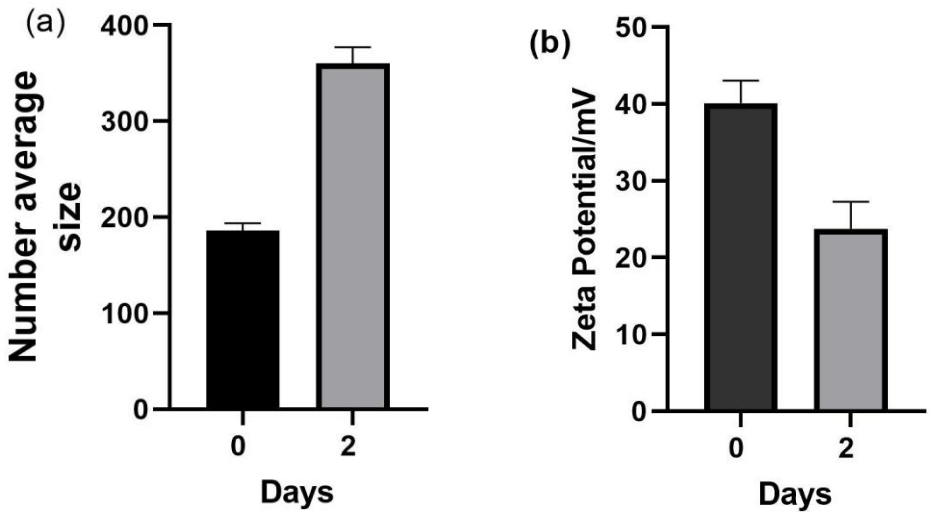

Figure 3.31: Stability of CPPN-Au in water (a) number average size and (b) Zeta potential after 2 days. Results represent the mean ± SD of four separate measurements.

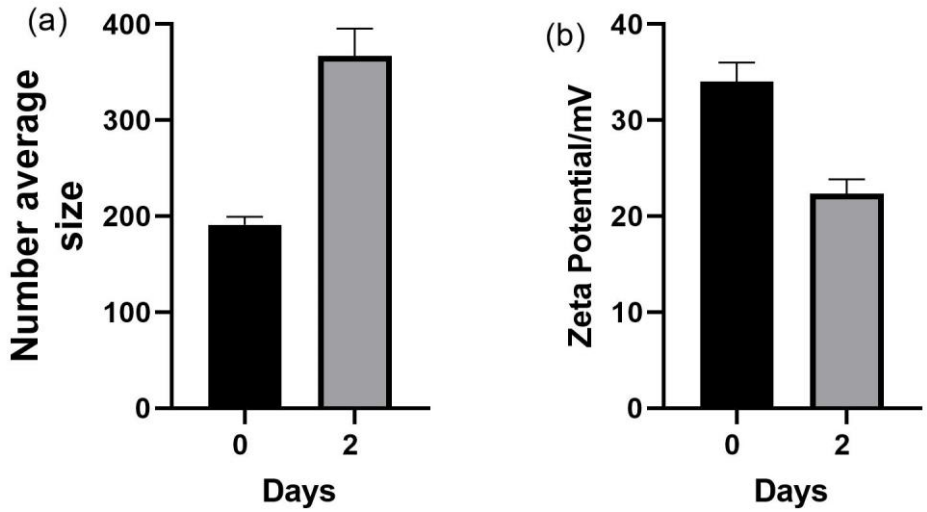

Figure 3.32: Stability of PCP-Au in water (a) number average size and (b) Zeta potential after 2 days. Results represent the mean ± SD of four separate measurements.

Section 4

Conclusions and Future works

Herein, we have prepared two novel water dispersible and mechanically stable conjugated polymer-based nanoparticles, namely conjugated polymer-porphyrin nanoparticles (CPPN) and cross-linked conjugated polymer nanoparticles (PCP) by nanoprecipitation using cucurbit[6]uril-(CB6)-catalyzed azide-alkyne cycloaddition (CB6-AAC) reaction. The nanoparticles were stable in water for months with any visible aggregation. They demonstrated high reactive oxygen species (ROS) generation, evident in the antibacterial and anticancer photodynamic therapy (PDT) experiments.

CPPN is a better photosensitizer than PCP due to the presence of porphyrin, which acts as a photosensitizer and can generate ROS when irradiated with light, thereby increasing the light-induced photodynamic antibacterial and anticancer effect of CPPN compared to PCP. CPPN is novel, can generate ROS more effectively; it shows minimal dark cytotoxicity (4%) and high light-induced biocidal activity (96%). These features show that CPPN is an ideal and potential photosensitizer that can be utilized in a broad-spectrum antimicrobial and anticancer photodynamic therapy.

In future work, modifying the nanoparticles by incorporating targeting groups like peptides and amino acids will help improve the PDT efficiency of the nanoparticles. Furthermore, the nanoparticles can be tested on other cancer cell lines. Also, the stability of CPPN-Au and PCP-Au nanoparticles can be improved by first reducing the gold from Au^{3+} to Au^{0} before adding the conjugated polymer nanoparticles. Since the nanoparticles are fluorescent, they can be used in cellular imaging. In addition, the nanoparticles can be utilized in photoacoustic imaging.

References

[1] WHO, https://www.who.int/news-room/fact-sheets/detail/antimicrobial-resistance, accessed: 10, 2020

[2] A. Petchiappan, D. Chatterji, ACS Omega 2017, 2, 7400-7409

[3] P. Vikesland, E. Garner, S. Gupta, S. Kang, A. Maile-Moskowitz, N. Zhu, Acc. Chem. Res. 2019, 52, 916-924

[4] G. D. Wright, Chem. Commun. 2011, 47, 4055-4061

[5] T. Maisch, Photochemical & Photobiological Sciences 2015, 14, 1518-1526

[6] T. Maisch, Mini Rev. Med. Chem. 2009, 9, 974-983

[7] B. C. Wilson, M. S. Patterson, Phys. Med. Biol. 2008, 53, R61.

[8] Nurgül Kömerik, Michael Wilson, Steve Poole, the effect of photodynamic action on two virulence factors of gram-negative bacteria. Photochem. Photobiol. 2000, 72, 676–680.

[9] Rajesh, S.; Koshi, E.; Philip, K.; Mohan, A. Antimicrobial photodynamic therapy: An overview. J. Indian Soc. Periodontol. 2011, 15, 323–327.

[10] X. Zhao, J. Liu, J. Fan, H. Chao, X. Peng, Chem. Soc. Rev. 2021.

[11] Z. Zhou, J. Song, L. Nie, X. Chen, Chem. Soc. Rev. 2016, 45, 6597-6626.

[12] B. S. Dash, S. Das, and J.-P. Chen, Photosensitizer-Functionalized Nanocomposites for Light-Activated Cancer Theranostics, Int. J. Mol. Sci. 2021, 22(13), 6658.

[13] Jing Xu, Jianqing Gao, Qichun Wei, "Combination of Photodynamic Therapy with Radiotherapy for Cancer Treatment", Journal of Nanomaterials, vol. 2016, 8507924, 7 pages, 2016.

[14] E. D. Sternberg, D. Dolphin, C. Brückner, Tetrahedron 1998, 54, 4151-4202.

[15] M. Ethirajan, Y. Chen, P. Joshi, R. K. Pandey, Chem. Soc. Rev. 2011, 40, 340-362.

[16] M. Rajora, J. Lou, G. Zheng, Chem. Soc. Rev. 2017, 46, 6433-6469.

[17] S. Singh, A. Aggarwal, N. D. K. Bhupathiraju, G. Arianna, K. Tiwari, C. M. Drain, Chem. Rev. 2015, 115, 10261-10306.

[18] X. Li, S. Lee, J. Yoon, Chem. Soc. Rev. 2018, 47, 1174-1188.

[19] [126] T. J. Dougherty, C. J. Gomer, B. W. Henderson, G. Jori, D. Kessel, M. Korbelik, J. Moan, Q. Peng, J. Natl. Cancer Inst., 1998, 90, 889-905.

[20] L. Chen, H. Bai, J-F. Xu, S. Wang, X. Zhang, ACS Appl. Mater. Interfaces, 2017, 9, 13950-13957.

[21] W. Lei, G. Jiang, Q. Zhou, B. Zhang, X. Wang, Phys. Chem, Chem. Phys., 2010, 12, 13255-13260.

[22] S. Gao, R. Islam and J. Fang, Tumor Environment-Responsive Hyaluronan Conjugated Zinc Protoporphyrin for Targeted Anticancer Photodynamic Therapy, J. Pers. Med. 2021, 11(2), 136.

[23] M. Özkan, Y. Keser, S. E. Hadi, D. Tuncel, Eur. J. Org. Chem. 2019, 2019, 3534-3541.

[24] A. Gupta, S. Mumtaz, C.-H. Li, I. Hussain, V. M. Rotello, Chem. Soc. Rev. 2019, 48, 415-427.

[25] X. Li, H. Bai, Y. Yang, J. Yoon, S. Wang, X. Zhang, Adv. Mater. 2019, 31, 1805092.

[26] L. Zhou, T. Qiu, F. Lv, L. Liu, J. Ying, S. Wang, Adv. Healthc. Mater. 2018, 7, 1800670.

[27] J. Li, K. Pu, Chem. Soc. Rev. 2019, 48, 38-71.

[28] Y. Jiang, K. Pu, Acc. Chem. Res. 2018, 51, 1840-1849.

[29] D. Cui, J. Huang, X. Zhen, J. Li, Y. Jiang, K. Pu, Angew. Chem. 2019, 58, 5920-5924.

[30] Z. H. Yu, X. Li, F. Xu, X. L. Hu, J. Yan, N. Kwon, G. R. Chen, T. Tang, X. Dong, Y. Mai, Angew. Chem. 2020, 132, 3687-3693.

[31] B. Wang, G. Feng, M. Seifrid, M. Wang, B. Liu, G. C. Bazan, Angew. Chem. 2017, 56, 16063-16066.

[32] D. Tuncel, H. V. Demir, Nanoscale 2010, 2, 484-494.

[33] D. Tuncel, Nanoscale Adv. 2019, 1, 19-33.

[34] G. Feng, Y. Fang, J. Liu, J. Geng, D. Ding, B. Liu, Small 2017, 13, 1602807.

[35] Y. Wang, S. Li, L. Liu, L. Feng, ACS Appl. Bio Mater. 2018, 1, 27-32.

[36] J. Pennakalathil, E. Jahja, E. S. Özdemir, O. Konu, D. Tuncel, Biomacromolecules 2014, 15, 3366-3374.

[37] K. Landfester, Angew. Chem., Int. Ed., 2009, 48, 4488.

[38] J. Pecher and S. Mecking, Chem. Rev., 2010, 110, 6260.

[39] C. Wu, C. Szymanski and J. McNeill, Langmuir, 2006, 22, 2956.

[40] C. Wu, C. Szymanski, Z. Cain and J. McNeill, J. Am. Chem. Soc., 2007, 129, 12904.

[41] C. Wu, B. Bull, C. Szymanski, K. Christensen and J. McNeill, ACS Nano, 2008, 2, 2415.

[42] J. Yu, C. Wu, S. Sahu, L. Fernando, C. Szymanski and J. McNeill, J. Am. Chem. Soc., 2009, 131, 18410.

[43] I. O. Ozel, T. Ozel, H. V. Demir and D. Tuncel, Opt. Express, 2010, 18, 670–684.

[44] I. O. Huyal, T. Ozel, D. Tuncel and H. V. Demir, Opt. Express, 2008, 16, 13391–13397.

[45] Tingting Sun, Jin-Hu Dou, Shi Liu, Xin Wang, Xiaohua Zheng, Yapei Wang, Jian Pei, and Zhigang Xie. Second Near-Infrared Conjugated Polymer Nanoparticles for Photoacoustic Imaging and Photothermal Therapy ACS Appl. Mater. Interfaces 2018, 10, 9, 7919–7926.

[46] Yuchao Liang, Hongjuan Zhang, Huanxiang Yuan, Wen Lu, Zelin Li, Lei Wang, and Li-Hua Gao. Conjugated Polymer and Triphenylamine Derivative Codoped Nanoparticles for Photothermal and Photodynamic Antimicrobial Therapy. ACS Appl. Bio Mater. 2020, 3, 6, 3494–3499.

[47 Liheng Feng, Jiarong Zhu, and Zhijun Wang. Biological Functionalization of Conjugated Polymer Nanoparticles for Targeted Imaging and Photodynamic Killing of Tumour Cells. ACS Appl. Mater. Interfaces 2016, 8, 30, 19364–19370.

[48] N. Elgiddawy, S. Ren, W. Ghattas, W. M. A. El Rouby, A. O. El-Gendy, A. A. Farghali, A. Yassar, and H. Korri-Youssoufi, Antimicrobial Activity of Cationic Poly(3-

hexylthiophene) Nanoparticles Coupled with Dual Fluorescent and Electrochemical Sensing: Theragnostic Prospect, Sensors 2021, 21(5), 1715.

[49] H. Yuan, H. Zhao, K. Peng, R. Qi, H. Bai, P. Zhang, Y. Huang, F. Lv L. Liu, J. Bao, and S. Wang, Conjugated Polymer-Quantum Dot Hybrid Materials for Pathogen Discrimination and Disinfection, ACS Appl. Mater. Interfaces 2020, 12, 19, 21263–21269.

[50] A. Parthasarathy, H. C. Pappas, E. H. Hill, Y Huang, D. G. Whitten, and K. S. Schanze, Conjugated Polyelectrolytes with Imidazolium Solubilizing Groups. Properties and Application to Photodynamic Inactivation of Bacteria, ACS Appl. Mater. Interfaces 2015, 7, 51, 28027–28034.

[51] D. Tuncel, J. H. Steinke, Macromolecules 2004, 37, 288-302.

[52] D. Tuncel, H. B. Tiftik, B. Salih, J. Mater. Chem. 2006, 16, 3291-3296.

[53] D. Tuncel, Ö. Özsar, H. B. Tiftik, B. Salih, Chem. Commun. 2007, 1369-1371.

[54] K. Kim, Cucurbiturils and related macrocycles, Royal Society of Chemistry, Cambridge, 2019.

[55] V. Ibrahimova, S. Ekiz, Ö. Gezici, D. Tuncel, Polym. Chem. 2011, 2, 2818-2824.

[56] M. Özkan, Y. Kumar, Y. Keser, S. E. Hadi, D. n. s. Tuncel, ACS Appl. Bio Mater. 2019, 2, 4693-4697.

[57] M. Özkan, Y. Keser, A. Koc, D. Tuncel, J. Porphyr. Phthalocyanines 2019, 23, 1406-1413.

[58] L. Chen, H. Bai, J.-F. Xu, S. Wang, X. Zhang, ACS Appl. Mater. Interfaces 2017, 9, 13950-13957.

[59] K. Liu, Y. Liu, Y. Yao, H. Yuan, S. Wang, Z. Wang, X. Zhang, Angew. Chem. 2013, 52, 8285-8289.

[60] J. Pennakalathil, E. Jahja, E. S. Özdemir, O. Konu, D. Tuncel, Biomacromolecules 2014, 15, 3366-3374.

[61] Ahmet Koç, Synthesis and Characterization of Cucurbituril based Photoactive Multifunctional Assemblies, 2019.

[62] A. L. Koner, I. Ghosh, N. Saleh, and W. M. Nau, “Supramolecular encapsulation of benzimidazole-derived drugs by cucurbit [7] uril,” Canadian Journal of Chemistry, vol. 89, no. 2, pp. 139–147, 2011.

[63] Y. Zhao, M. H. Pourgholami, D. L. Morris, J. G. Collins, and A. I. Day, “Enhanced cytotoxicity of benzimidazole carbamate derivatives and solubilisation by encapsulation in cucurbit [n] uril,” Organic & Biomolecular Chemistry, vol. 8, no. 14, pp. 3328–3337, 2010.

[64] Y. Zhao, D. P. Buck, D. L. Morris, M. H. Pourgholami, A. I. Day, and J. G. Collins, “Solubilisation and cytotoxicity of albendazole encapsulated in cucurbit [n] uril,” Organic & Biomolecular Chemistry, vol. 6, no. 24, pp. 4509–4515, 2008.

[65] Z. Miskolczy, M. Megyesi, G. T´ark´anyi, R. Mizsei, and L. Bicz´ok, “Inclusion complex formation of sanguinarine alkaloid with cucurbit [7] uril: inhibition of nucleophilic attack and photooxidation,” Organic & biomolecular chemistry, vol. 9, no. 4, pp. 1061–1070, 2011.

[66] C.-F. Li, L.-M. Du, W.-Y. Wu, and A.-Z. Sheng, “Supramolecular interaction of cucurbit [n] urils and coptisine by spectrofluorimetry and its analytical application,” Talanta, vol. 80, no. 5, pp. 1939–1944, 2010.

[67] N. Dong, S.-F. Xue, Q.-J. Zhu, Z. Tao, Y. Zhao, and L.-X. Yang, “Cucurbit [n] urils (n= 7, 8) binding of Camptothecin and the effects on solubility and reactivity of the anticancer drug,” Supramolecular Chemistry, vol. 20, no. 7, pp. 663–671, 2008.

[68] J. Pennakalathil, E. Jahja, E. S. Ozdemir, O. Konu, and D. Tuncel, “Red emitting, cucurbituril-capped, ph-responsive conjugated oligomer-based nanoparticles for drug delivery and cellular imaging,” Biomacromolecules, vol. 15, no. 9, pp. 3366–3374, 2014.

[69] L. Cao, G. Hettiarachchi, V. Briken, and L. Isaacs, “Cucurbit [7] uril containers for targeted delivery of oxaliplatin to cancer cells,” Angewandte Chemie International Edition, vol. 52, no. 46, pp. 12033–12037, 2013.

[70] J. A. Plumb, B. Venugopal, R. Oun, N. Gomez-Roman, Y. Kawazoe, N. S. Venkataramanan, and N. J. Wheate, “Cucurbit [7] uril encapsulated cisplatin overcomes cisplatin resistance via a pharmacokinetic effect,” Metallomics, vol. 4, no. 6, pp. 561–567, 2012.

[71] A. R. Kennedy, A. J. Florence, F. J. McInnes, and N. J. Wheate, “A chemical preformulation study of a host–guest complex of cucurbit [7] uril and a multinuclear platinum

agent for enhanced anticancer drug delivery," Dalton Transactions, no. 37, pp. 7695–7700, 2009.

[72] Y. Zhao, M. S. Bali, C. Cullinane, A. I. Day, and J. G. Collins, "Synthesis, cytotoxicity and cucurbituril binding of triamine linked dinuclear platinum complexes," Dalton Transactions, no. 26, pp. 5190–5198, 2009.

[73] N. Saleh, A. L. Koner, and W. M. Nau, "Activation and stabilization of drugs by supramolecular pka shifts: Drug-delivery applications tailored for cucurbiturils," Angewandte Chemie, vol. 120, no. 29, pp. 5478–5481, 2008.

[74] N. Kahwajy, A. Nematollahi, R. R. Kim, W. B. Church, and N. J. Wheate, "Comparative macrocycle binding of the anticancer drug phenanthriplatin by cucurbit [n] urils, β-cyclodextrin and para-sulfonatocalix [4] arene: a 1 h nmr and molecular modelling study," Journal of Inclusion Phenomena and Macrocyclic Chemistry, vol. 87, no. 3-4, pp. 251–258, 2017.

[75] H. Cong, C.-R. Li, S.-F. Xue, Z. Tao, Q.-J. Zhu, and G. Wei, "Cucurbituril resisted acylation of the anti-tuberculosis drug isoniazid via a supramolecular strategy," Organic & biomolecular chemistry, vol. 9, no. 4, pp. 1041– 1046, 2011.

[76] N. J. Wheate, V. Vora, N. G. Anthony, and F. J. McInnes, "Host–guest complexes of the antituberculosis drugs pyrazinamide and isoniazid with cucurbit [7] uril," Journal of Inclusion Phenomena and Macrocyclic Chemistry, vol. 68, no. 3-4, pp. 359–367, 2010.

[77] S. Dutta Choudhury, J. Mohanty, A. C. Bhasikuttan, and H. Pal, "A fluorescence perspective on the differential interaction of riboflavin and flavin adenine dinucleotide with cucurbit [7] uril," The Journal of Physical Chemistry B, vol. 114, no. 33, pp. 10717–10727, 2010.

[78] E. Corda, M. Hernandez, S. Sanchez-Cortes, and P. Sevilla, "Cucurbit [n] urils (n= 6–8) used as host molecules on supramolecular complexes formed with two different drugs: Emodin and indomethacin," Colloids and Surfaces A: Physicochemical and Engineering Aspects, vol. 557, pp. 66–75, 2018.

[79] S. D. Choudhury, J. Mohanty, H. Pal, and A. C. Bhasikuttan, "Cooperative metal ion binding to a cucurbit [7] uril- thioflavin t complex: Demonstration 118of a stimulus-responsive fluorescent supramolecular capsule," Journal of the American Chemical Society, vol. 132, no. 4, pp. 1395–1401, 2010.

[80] I. W. Wyman and D. H. Macartney, “Host–guest complexations of local anaesthetics by cucurbit [7] uril in aqueous solution,” Organic & biomolecular chemistry, vol. 8, no. 1, pp. 247–252, 2010.

[81] A. Boreham, R. Brodwolf, K. Walker, R. Haag, and U. Alexiev, Molecules 2017, 22(1), 17.

[82] R. Peng, Y. Luo, Q. Cui, J. Wang, and L. Li, Near-Infrared Conjugated Oligomer for Effective Killing of Bacterial through Combination of Photodynamic and Photothermal Treatment, ACS Appl. Bio Mater. 2020, 3, 2, 1305–1311.

[83] L. Guo, H. Wang, Y. Wang, F. Liu, and L. Feng, Organic Polymer Nanoparticles with Primary Ammonium Salt as Potent Antibacterial Nanomaterials, ACS Appl. Mater. Interfaces 2020, 12, 19, 21254–21262.

[84] S. Khan, M. Rayis P, and I. Naseem, ROS mediated antibacterial activity of photo illuminated riboflavin: A photodynamic mechanism against nosocomial infections, https://doi.org/10.1016/j.toxrep.2019.01.003.

[85] J. R. Melamed, R. S. Edelstein, and E. S. Day, Elucidating the Fundamental Mechanisms of Cell Death Triggered by Photothermal Therapy, ACS Nano 2015, 9, 1, 6–11.

[86] B. Zhou, Y. Li, G. Niu, M. Lan, Q. Jia, and Q. Liang, Near-Infrared Organic Dye-Based Nanoagent for the Photothermal Therapy of Cancer, ACS Appl. Mater. Interfaces 2016, 8, 44, 29899–29905.

[87] Aleksandra Zielińska, Filipa Carreiró, Ana M. Oliveira, Andreia Neves. Polymeric Nanoparticles: Production, Characterization, Toxicology and Ecotoxicology. Molecules 2020, 25(16), 3731.

[88] J. Zeng, W. Yang, D. Shi, X. Li, H. Zhang, and M. Chen, Porphyrin Derivative Conjugated with Gold Nanoparticles for Dual-Modality Photodynamic and Photothermal Therapies In Vitro, ACS Biomater. Sci. Eng. 2018, 4, 3, 963–972.

[89] S. C. Karunakaran, P. S. S. Babu, B. Madhuri, In Vitro Demonstration of Apoptosis Mediated Photodynamic Activity and NIR Nucleus Imaging through a Novel Porphyrin, ACS Chem. Biol. 2013, 8, 1, 127–132.

[90] Y. Cai, Q. Tang, X. Wu, Bromo-Substituted Diketopyrrolopyrrole Derivative with Specific Targeting and High Efficiency for Photodynamic Therapy, ACS Appl. Mater. Interfaces 2016, 8, 17, 10737–10742.

[91] M. Özkan, S. E. Hadi, İ. Tunç, Y. Midilli, B. Ortaç, and D. Tuncel, Cucurbit[7]uril-Capped Hybrid Conjugated Oligomer-Gold Nanoparticles for Combined Photodynamic-Photothermal Therapy and Cellular Imaging, ACS Appl. Polym. Mater. 2020, 2, 9, 3840–3849.

[92] J. Lagona, P. Mukhopadhyay, S. Chakrabarti, and L. Isaacs, "The cucurbit [n] uril family," Angewandte Chemie International Edition, vol. 44, no. 31, pp. 4844–4870, 2005.

APPENDIX

Table A.1: Examples of Cucurbituril-Biomolecule complexes in the literature

Guest	Function of Guest	Host CB	Advantage of Complexation	Reference
Benzimidazole (BZ)	Anthelmintic drug	CB6, CB7, CB8	Water solubility was enhanced upon complexation by 1200-fold.	[62], [63]
 Albendazole (ABZ)	Anthelmintic drug	CB6, CB7, CB8	Water solubility was enhanced upon complexation by 2000-fold.	[62], [64]
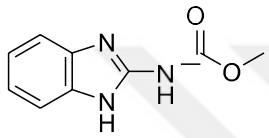 Carbendazim (CBZ)	Fungicide	CB7	Water solubility was enhanced upon complexation by 7-fold.	[62]
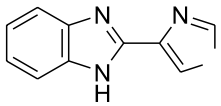 Thiabendazole (TBZ)	Anthelmintic drug	CB7	Water solubility was enhanced upon complexation by 10-fold.	[62]
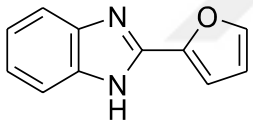 Fuberidazole (FBZ)	Fungicide	CB7	Water solubility was enhanced upon complexation by 3-fold.	[62]
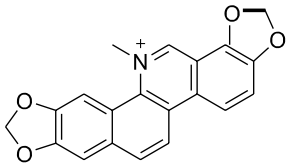 Sanguinarine	Alkaloid antibiotic and botanical fungicide	CB7	Active sanguinarine was stabilized.	[65]
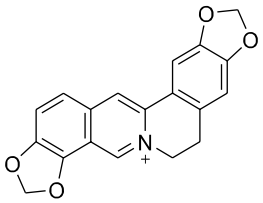 Coptisine (COP)	Metabolite	CB5, CB6, CB7, CB8	Stability and fluorescence intensity of COP were increased.	[66]
 Lansoprazole	Proton pump inhibitor, prevents stomach and intestinal ulcers	CB7	Activation and stabilization were provided upon complexation.	[74]

Camptothecin (CPT)	Strong anti-tumor agent	CB7, CB8	*In vitro* study of targeted drug delivery towards A549, P388D1, MCF7 and MDA-MB-231 cell lines.	[67], [68]
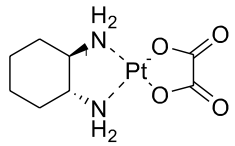 Oxaliplatin	Anti-cancer drug	CB7	Enhanced cytotoxicity in vitro towards L1210FR cells.	[69]
Cisplatin	Anti-cancer drug	CB7	*In vitro* and *in vivo* studies confirmed that, complex defeats cisplatin resistance via pharmacokinetic effect.	[70]
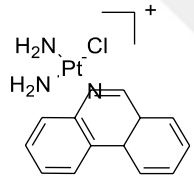 Phenanthriplatin	DNA-binding anti-cancer drug candidate	CB7, CB8	CB7 accommodates one equivalent phenanthriplatin molecule and CB8 accommodates two equivalent phenanthriplatin molecules.	[75]
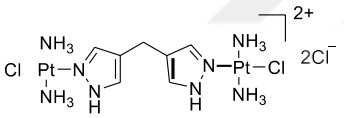 trans-[{Pt(NH3)2Cl}] 2μ-dpzm)]$^{2+}$	DNA-binding anti-cancer Platinum complex	CB7	Stability was completely enhanced upon complexation.	[71]
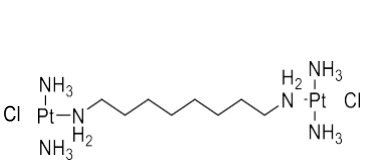 *trans*-[{PtCl(NH3)2}2(μNH2(CH2)8 NH2)]$^{2+}$ CT008	Antibiotic drug	CB10	Strong inclusion complex formed.	[65]
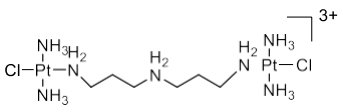 CT033	Antibiotic drug	CB7, CB8	Enhanced cytotoxicity in vitro towards L1210 cells and cisplatin resistant subline L210/DDP.	[72]

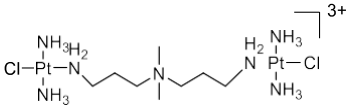 CT233	Antibiotic drug	CB7, CB8	Enhanced cytotoxicity in vitro towards L1210 cells and cisplatin resistant subline L210/DDP, however 50-times less active than CT033.	[72]
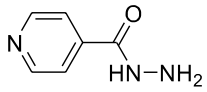 Isoniazid	Antibiotic for tuberculosis	CB6, CB7	CB6 and CB7 assist hindrance of acylation of isoniazid.	[76]

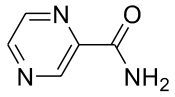 Pyrazinamide	Medication to treat tuberculosis	CB7	Drug physical stability was achieved upon complexation.	[77]
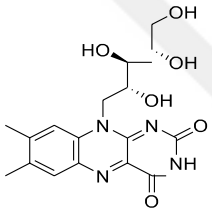 Riboflavin (RF)	Vitamin B2	CB7	Fluorescence intensity of RF was quenched upon complexation.	[78]
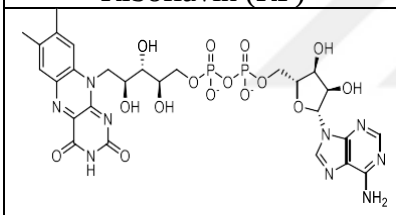 Flavin Adenine Dinucleotide (FAD)	Human, *E. coli* and mouse metabolite	CB7	Fluorescence intensity of FAD was enhanced upon complexation.	[79]
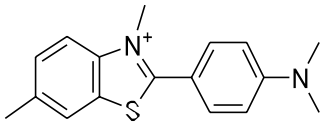 Thioflavin T (ThT)	Stain for amyloid	CB7	1:1 (CB7.ThT) and 2:1 [(CB7)2.ThT] complexes formed and fluorescence intensities were enhanced upon addition of metal cations.	[150]
Procaine	Local anesthetic	CB7	Very stable complex formed KCB7 = (3.5 ± 0.7) × 10^4 dm^3 mol^{-1}.	[80]
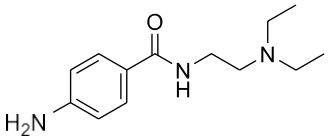 Procainamide	Local anesthetic and medication for cardiac arrhythmias	CB7	Very stable complex formed KCB7 = (7.8 ± 1.6) × 10^4 dm^3 mol^{-1}.	[81]

Prilocaine	Local anesthetic	CB7	Very stable complex formed $K_{CB7} = (2.6 \pm 0.6) \times 10^4\ dm^3\ mol^{-1}$.	[81]
Tetracaine	Local anesthetic	CB7	Very stable complex formed $K_{CB7} = (1.5 \pm 0.4) \times 10^4\ dm^3\ mol^{-1}$.	[81]